University of Alberta

Velocity and concentration fluctuations in concentrated solid-liquid flows

by

Seyed Abdolreza Hashemi

A thesis submitted to the Faculty of Graduate Studies and Research in partial fulfillment of the requirements for the degree of

Doctor of Philosophy

in

Chemical Engineering

Department of **Chemical and Materials Engineering**

Fall 2013

Edmonton, Alberta

Dedication

To my mother Shirin and my father Mohammad Ali; to my sibling Tahereh.

To the love of my life Maedeh.

Abstract

The aim of this research was to investigate experimentally the turbulent flow of concentrated slurries in horizontal pipelines and to improve the fundamental understanding of mechanism(s) that govern these. High speed Electrical Impedance Tomography (EIT) was combined with advanced signal processing techniques to develop a measurement procedure to obtain solids concentration distributions and turbulent intensity profiles in a highly concentrated solid-liquid mixture.

Specific Energy Consumption (SEC), which is a measure of transport efficiency, was used to find the optimum operating condition for heterogeneous (settling) slurry flows. The effects of solids concentration, mixture velocity and particle diameter on SEC were determined using the equivalent-fluid and near-wall lift models for fine- and coarse-particle slurries, respectively. The analysis shows that the minimum SEC occurs at a solids concentration of approximately 30% by volume. Model predictions were compared with the results of numerous experimental studies.

In spite of the utility of phenomenological models, such as the near-wall lift model, many fundamental questions in solid-liquid flows remain. Issues include the poor understanding of the mechanisms that govern these complex flows, and the lack of local parameters measured and available for model validation studies. Among the various parameters, solids and liquid concentration fluctuations and turbulent intensities are arguably the most important pieces of information that need to be measured.

In horizontal slurry pipe flows, solids velocity and concentration fluctuations were measured for concentrated sand-water mixtures (20 - 35% solids by volume).

Slurries of narrowly sized sand (d_{50} = 100 μm) were tested in a 52 mm (i.d.) pipe loop at different mixture velocities (2 - 5 m/s) that were significantly above the deposition velocity. The results showed that the magnitude of the local solids concentration fluctuations is greater near the pipe wall and increases as the mixture velocity increases. Additionally, the concentration fluctuations are greater near the pipe invert, particularly at lower mixture velocities and/or concentrations where the solids concentration profiles are asymmetric.

Experiments were also carried out in a 10.16 cm (i.d.) solid-liquid fluidized bed using 2, 3 and 4 mm mono-sized spherical glass beads with water as the continuous phase. A reduced solids concentration in the central region of the bed, which is known to occur during the bubbly (aggregate) fluidization regime, was observed. This study provides further insight into the dynamic behaviour of liquid-solid fluidized beds through the measurement of local solids concentration fluctuations.

Acknowledgements

Though only my name appears on the cover of this dissertation, many great people have contributed to its completion. I owe my gratitude to all those people who have made this dissertation possible and because of whom my graduate experience has been one that I will cherish forever.

My deepest gratitude and special thanks is to my supervisor, Dr. Sean Sanders, who gave me the resources and the freedom I required. I have been amazingly fortunate to have a supervisor who gave me the freedom to explore on my own, and at the same time one that gave me the guidance to recover when my steps faltered. Dr. Sanders taught me how to question thoughts and express ideas. His patience and support helped me overcome many crises and finish this dissertation. I hope that one day I would become as good a supervisor to my students as Dr. Sanders has been to me.

Special thanks to Dr. Jos Derksen, Dr. Randall Gillies, Dr. Ryan Spelay and Dr. Ken Wilson for their great scientific support, insightful comments and constructive criticisms at different stages of my research.

Special thanks also go to Ms. Terry Runyon for her endless assistance.

I would like to thank the Saskatchewan Research Council (SRC) for providing me with equipment and laboratory access during my research. Also, I would like to thank the technicians and staff at SRC Pipe Flow Technology Centre^{TM}, especially Paul Schergevitch and Curtis Knops.

I would also like to thank the technicians and staff at Chemical and Materi-

als Engineering machine and instrument shops, especially Walter Boddez, Richard Copper, Les Dean, Clark Bicknell and Dave Parlin.

Also, pursuit of my education would have not been possible if were not for the encouragement, patience and support of my family, especially my father.

Finally, I gratefully acknowledge the financial support provided through the NSERC Industrial Research Chair in Pipeline Transport Processes.

Contents

List of Figures

List of Tables

1

Introduction

The term 'multiphase flow' generally refers to a flow condition where two or more phases are present. Multiphase flows not only appear in natural forms such as snow, rain, clouds, avalanches and so on, but are also widely used in many industrial processes. Examples include fluidization, pneumatic conveying, slurry transport pipelines, bubble columns and hydrocyclones. Multiphase flows could be classified into different categories based on their components. Among them, gas-solid, solid-liquid and gas-liquid flows are found in various industrial applications. Table 1.1 summarizes important types and samples of multiphase flows (1). The focus of the current study is on dispersed solid-liquid flows, where solid particles are dispersed in a liquid phase.

Prediction of the behavior of multiphase flows is essential in determining the efficiency of these processes. However, single phase turbulence and multiphase flows are two main topics in fluid mechanics that remain unsolved to date. There are many questions to be answered for single phase fluid turbulence, especially at high Reynolds numbers and one needs to use empirical models to deal with unsteady turbulent motion. The addition of a dispersed phase brings the complexity to a new level by adding new parameters, e.g. particle size, spatial distribution of the dispersed phase and descriptions of the interactions between phases. Many different modeling approaches have been taken to address the complexities associated with the presence of a dispersed phase, depending on the extent of interaction (coupling)

Table 1.1: Multiphase flow types and samples adapted from Crowe et al. (1)

Gas–liquid flows	Bubbly flows Separated flows Gas–droplet flows
Gas–solid flows	Gas–particle flows Pneumatic transport Fluidized beds
Liquid–solid flows	Slurry flows Oil sand conditioning (hydrotransport) Open-channel sediment transport
Three–phase flows	Bubbles in a slurry flow Droplets/particles in gaseous flows

between the phases and the levels of detail and accuracy required from the model. Regardless of the modeling approach, however, experimental studies are needed to validate model performance. Thus, one could say that multiphase flow research can be divided into three main categories: (1) theoretical studies, (2) numerical studies, and (3) experimental studies. Because of the complex nature of the equations of motion when applied to multiphase flows, theoretical solutions and studies are limited to a few simple conditions. Although multiphase flow science has undergone many significant advances in both theoretical and experimental aspects during the last decades, it is still far from its final precise mathematical modeling framework. A better understanding of the advantages and limitations of the existing modeling approaches is crucial for multiphase flow research. The current research is mainly focused on the modeling and experimental study of highly concentrated slurry (solid-liquid) pipeline flows. Specifically, the focus is to determine the advantages and disadvantages of existing models and to improve the fundamental understanding of mechanism(s) that govern these flows through a series of novel experimental studies.

This chapter is organized as follows: in the first section, different classes of turbulent slurry flow models are described and their advantages and limitations are discussed. The concept of Specific Energy Consumption (SEC) for slurry pipeline

flow is introduced as a measure to evaluate the energy efficiency of the process. Two main numerical approaches for modeling solid-liquid flows i.e. the Lagrangian and the Eulerian methods are described in this section along with their advantages and constraints. The two-fluid model, which is an example of a Eulerian approach, is described in more detail to help better understand the types of measurements that are required to improve existing models. The major measurement techniques and experimental methods in multiphase flow are described in the Section 1.2. The technique of interest for this study, Electrical Impedance Tomography (EIT), is selected by reviewing the benefits and drawbacks of various techniques. The research objectives and important contributions of the current study are highlighted in the last two sections.

1.1 Turbulent slurry flow modeling

Slurry flows occur in a wide variety of industries such as mining and minerals processing, the oil and gas sector, chemical production, and are also prevalent in the food and pharmaceutical industries. The scale of these flows ranges from microscale channel flow to the large (diameter of $\sim 1\ m$) hydrotransport pipelines found in the oil sand industry.

Slurry flows are generally divided into two main categories. If the solids are very fine, particle settling is very slow and the solids concentration remains uniform within the mixture, these mixtures are often denoted as homogeneous or non-settling slurries. They frequently consist of fine flocculating particles and usually behave as non-Newtonian fluids (2; 3).

Settling or heterogenous slurries contain non-flocculating particles, where the particles show a tendency to settle. There is a minimum operating velocity which is required to avoid particle accumulation. They are also characterized by asymmetric concentration and velocity profiles in horizontal pipelines, examples of which are shown in Figures 1.1 and 1.2 (2).

The modeling of these mixtures is very complicated and single phase fluid models are no longer valid to describe them. One must account for the presence of the solids, and the energy dissipation caused by their interaction with the fluid phase, their collisions with each other and with the pipe wall. For heterogeneous (settling) slurries of the type described here, the use of homogeneous or fluid models whereby the solids are assumed simply to augment the viscosity of the suspending liquid must be avoided. The solids and liquids must instead be viewed as distinct but interacting phases when developing models.

The slurry flow modeling spectrum consists of three main sub-categories i.e. empirical, phenomenological and numerical models. The first notable heterogenous slurry model was reported by Durand and Condolios (4), who developed an empirical correlation to estimate the frictional pressure loss in heterogenous (settling) slurry pipelines. In 1955, Newitt et al. (5) established an equation for the prediction of frictional loss in stratified flow. This method, which was a regime-specific correlation, was developed by employing the concept of mechanical sliding friction and was limited to fully stratified flows with $V_m < 17v_t$ where v_t is the particle terminal settling velocity and V_m is the mixture velocity (3). Although Newitt's equation and Durand's formulation have profound differences, they share a similar deficiency where the variation of particle size or terminal settling velocity do not affect the frictional loss. This deficiency originates from the fact that these models were developed as empirical correlations with limited attention paid to underlying physical mechanisms.

A major advancement in slurry flow modeling came with Wilson's analysis of fully and partially stratified flows, which utilized the concept of Coulombic friction to determine frictional pressure loss for slurries comprised of very coarse particles (6). Coulombic friction is due to particles that are not suspended by fluid turbulence. The immersed weight of the unsuspended particles is supported through direct particle contact with the pipe wall. The Coulombic stress is strongly dependent on particle size (7). In this stratified model, the slurry flow is viewed as having two separate

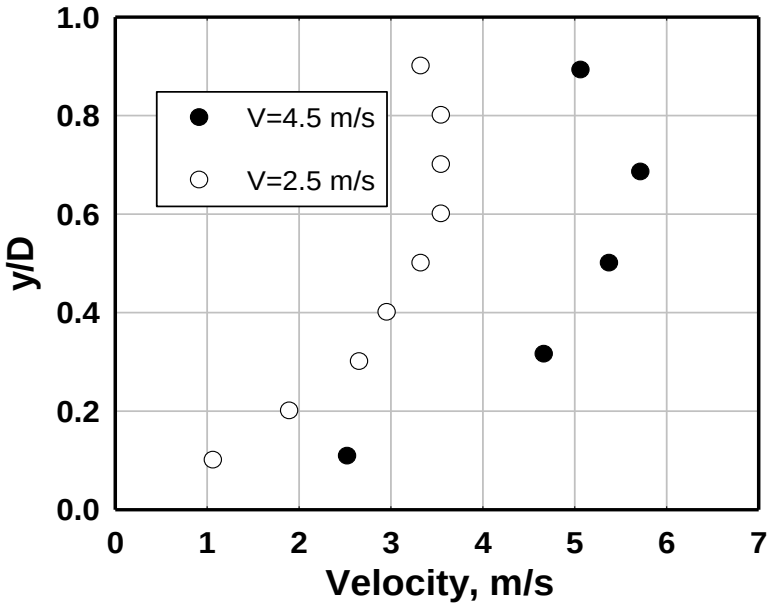

Figure 1.1: Local velocities measured on the vertical axis of a horizontal pipe: $d_p = 0.64\ mm$; $D = 0.105\ m$; $C_S = 25\%$ (by volume).

layers, with a moving bed of solids occupying the lower layer. In Wilson's analysis, the driving force for moving the bed is assumed to be the combination of the pressure gradient that acts on the portion of the cross section occupied by the bed and the effect of the shear stress on the bed's upper surface (3). Experimental results showed that the Wilson's two-layer approach is valid when the particles are larger than about 0.5 mm (8).

Although stratification for slurry flows containing particles less than 0.5 mm in diameter occurs to some extent, Wilson's two layer model was not suitable to accurately capture their flow behaviour. The importance of slurry flows with particles smaller than 0.5 mm and their extensive industrial applications was the driving force to develop a modeling framework capable of dealing with this class of heterogenous slurries. An improved version of Wilson's two-layer model was developed by Gillies et al. (9). The major improvements in the model included the way it deals with

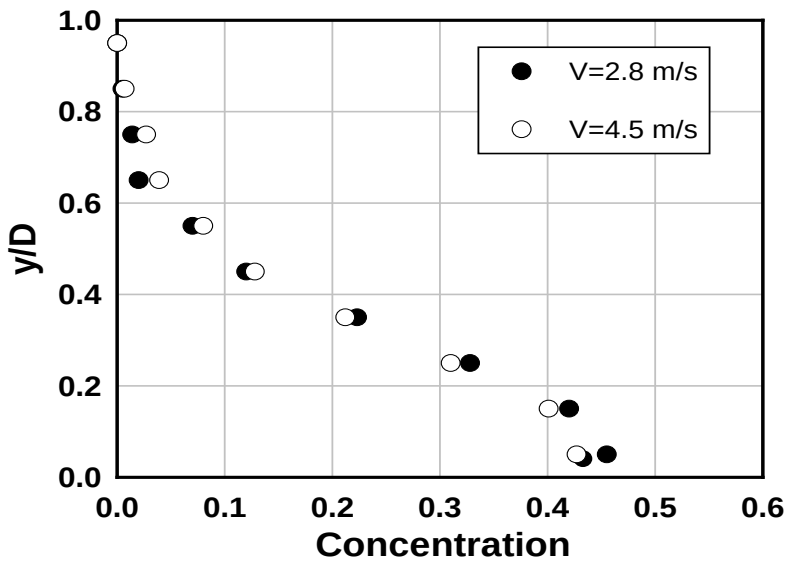

Figure 1.2: Concentration distributions measured for coarse sand slurries flowing in a horizontal pipe: $d_p = 0.64\ mm$; $D = 0.105\ m$; $C_S = 15\%$ (by volume).

the solids concentration in the lower layer and the role of particles smaller than 74 microns. The fine particles i.e. the -74 μm fraction, are assumed to combine with the suspending liquid. The resulting mixture is considered as a fluid with new density and viscosity. The coarse particles i.e. the +74 μm fraction, are assumed to be uniformly distributed within the flow domain. The smaller coarse particles are suspended by turbulent forces and contribute in the model to kinematic (velocity-dependent) friction loss. The lower layer contains these suspended particles and also the coarse fraction of particles that are not suspended by fluid turbulence, whose immersed weight is transmitted to the pipe wall. This model is generally referred to as the "SRC" two-layer model, as it was developed at the Saskatchewan Research Council. A schematic representation of the two-layer model is provided here in Figure 1.3 (2).

In 1994, Gillies and Shook further improved the performance of the SRC two-layer model by developing a model to predict the concentration distribution of particles

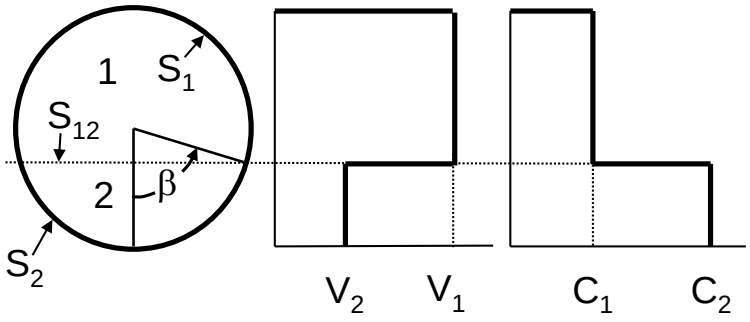

Figure 1.3: Schematic representation of the two-layer model.

in horizontal slurry pipe flows (10). This concentration distribution model was used to predict the solids concentration in the upper and lower layers.

Wilson et al. (11; 12) suggested that at high velocities, particles experience a lift force which results in particle migration away from the wall. They believe that this force is effective only near the wall. The so-called *near-wall lift force* tends to drive particles away from the pipe wall. It is strongly dependent on the shape of the fluid velocity profile and the ratio of the particle diameter to the viscous sublayer thickness. The effect of near-wall lift is important at higher velocities and for coarser particles (12).

A series of investigations conducted from 2000 to 2013 was devoted to the study of the contribution of particle dispersive stress and near-wall lift to kinematic friction in slurry pipeline flows (13; 2; 14). The particle dispersive stresses are caused by shear related particle interactions. Shearing the closely-spaced particles generates a normal stress which can be correlated to shear rate, solids concentration and particle size (15). These forces tend to drive particles toward the pipe wall. They are strongly dependent on particle concentration and are important at high solids concentrations. Experimental investigation showed that a substantial increase in frictional loss occurred at solids concentrations higher than 35% by volume. This effect was added to the SRC two-layer model by introducing a particle friction factor to account for the extra friction at high solids concentrations. Correlations for calculating parti-

cle friction factor were developed by analysing experimental results at high solids concentrations (13; 2; 14).

Studies conducted during the last 60 years suggest that the major frictional loss mechanisms in coarse particle slurry flows are:

1- Particle dispersive stresses

2- Coulombic or contact load friction

3- Near-wall lift effect

Figure 1.4 shows friction losses in a given slurry pipeline (2). At low velocities, the frictional loss for 0.27 mm and 0.64 mm particles is substantially higher compared to that of 0.09 mm particles. This increase is mainly due to the formation of a sliding bed and the resulting Coulombic friction. A sliding bed is less likely to be found for slurries of finer particles because these particles are effectively suspended by fluid turbulence. At high velocities, however, the pressure gradient for 0.27 mm particles is lower than that measured for the 0.09 mm particles. At high velocities the pressure gradient for larger particles decreases due to the effect of the near-wall lift force. As 0.09 mm particles are not large enough to experience the lift forces, the pressure gradient for 0.27 mm particles tends to be smaller than that for the 0.09 mm particles.

Presently, existing phenomenological models, such as the SRC two-layer model, are capable of predicting the basic parameters required in pipeline design and operation: namely, the minimum operating velocity, frictional pressure losses, delivered solids concentration and scale-up of lab or pilot data to commercial-scale plants for narrowly graded coarse particles. An example of the application of phenomenological models to study slurry pipeline flow is provided in the following section (i.e. Section 1.1.1) and in Chapter 2.

1.1.1 Specific Energy Consumption (SEC)

As the main purpose of a slurry pipeline is to transport solids economically over long distances, the energy required to transport a unit mass of solids over a unit

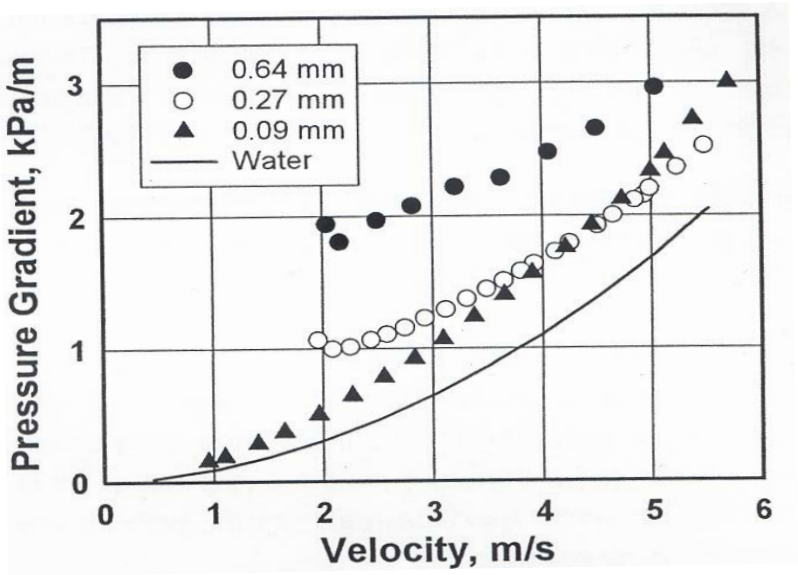

Figure 1.4: Pressure drop as a function of velocity for slurries containing water and 30% sand (by volume) in a horizontal pipeline ($D = 0.1\ m$).

pipeline length is an appropriate measure to evaluate the energy efficiency of different pipeline operating conditions. This measure is often referred to as Specific Energy Consumption (SEC)(3) and generally is expressed in units such as $\frac{J}{tonne.km}$ or $\frac{BTU}{ton.mile}$.

In terms of energy consumption, it is desirable to operate a pipeline at or near the minimum SEC, as lower SEC values represent a more energy-effective operation.

Existing slurry models can therefore be used to optimize the SEC and determine the desirable operating conditions for a slurry pipeline. In Chapter 2, two models are used to predict SEC values for fine- and coarse-particle slurries over a range of operating conditions, to show how existing phenomenological models can be valuable.

In spite of the utility of phenomenological models, there are many important phenomena that these models are unable to provide information about. Examples include pipe wear predictions, behavior of slurries with broad size distributions and flow in more complex geometries such as pumps and hydrocyclones. To deal with

this more complex class of flow problem, we require computational models.

1.1.2 Computational models

Recall that computational models are the third category of slurry flow models introduced previously. These are mainly based on the numerical solution of equations of motion, or Navier-Stokes (N-S) equations. Solution of the complete Navier-Stokes equations will provide us with comprehensive information about the flow.

Recent advances in computational methods and computational resources, along with the development of numerical simulation methods such as Direct Numerical Simulation (DNS), have enabled researchers to directly solve Navier-Stokes equations and resolve the fluid flow in great detail. However, these methods need enormous computing resources and are only applicable to a very limited number of multiphase flow cases, i.e. very dilute two-phase flow at low Reynolds numbers. Except for these simplified cases, it is not possible to solve the complete form of these equations because the number of time steps and the spatial resolution required would exceed the capacity of the most powerful computers currently available (16). Although these methods are of great importance in understanding the fundamentals of turbulent multiphase flows, the computer power required to apply these methods to industrial flow conditions cannot be expected in the foreseeable future. The common way to overcome the time and spatial resolution problem is to solve the time-averaged equations to obtain the time-averaged field properties. In this way, the instantaneous variables are treated as a product of statistical mean values plus fluctuating values (Reynolds decomposition) which results in the Reynolds Averaged N-S equations of motion (RANS). Two main numerical approaches based on RANS equations are commonly used in dealing with engineering problems. These two main approaches are (1) Eulerian- Lagrangian (trajectory models) and (2) Eulerian-Eulerian (two-fluid model) methods.

In trajectory or Lagrangian particle tracking models, the motion of individual particles in the fluid field is assessed and the effect of relevant forces such as lift

and drag on particles is evaluated. The particles are usually considered to be point particles. As the number of real particles is generally too high for full resolution, a computational particle (*parcel*) that represents a number of particles is employed in simulation. As a result, the flow around the individual particles cannot be resolved. In these methods, all the particles or representative particles need to be followed at the same time. In order to obtain statistically reliable results, typically 10000 to 100000 particles or parcels need to be considered. The advantage of this approach is that the tracking of a particle and its behavior in the flow will provide important information on parameters such as fluid-particle interactions and particle-particle interactions. However, this method is suitable to dilute two phase flows where the number of particles is limited. The application of particle tracking models for dense flows, where the number of particles is very high and the dispersed phase influences the fluid flow, is impractical. The two-fluid model is another commonly used method in modeling multiphase flows (17). This model treats each phase as a separate fluid and averaged equations of motion are written for each individual phase. Since the macroscopic fields of one phase are not independent of the other phase, interaction terms accounting for the transport of mass, momentum and energy among phases should be considered in the equations (18). As one does not need to follow all individual particles in the two–fluid approach and all particles are considered as a continuous phase, it is the preferred approach for the numerical study of dense two phase flows such as slurry transport pipelines and fluidized beds.

This modeling approach is described in greater detail in Section 1.1.3, with particular attention paid to the closure relations, which are equations or sub-models that are needed to account for fluid turbulence, particle-turbulence interactions, particle-particle interactions and interphase momentum exchange. Reliable and accurate closure relations are required; without them, the overall quality of the computational model suffers. In many cases, and especially for solid-liquid systems, the empirical or semi-empirical closure relations that have been developed are unsatisfactory.

The two major problems are that (*i*) many of the models have not been validated for solid-liquid systems and (*ii*) there is poor understanding of the nature of the mechanisms that the models are attempting to describe. In turbulent solid-liquid multiphase systems, the local, instantaneous velocities and concentrations of both phases fluctuate significantly and closure relations represent an attempt to model the effects of these fluctuations in a time- and spatially-averaged way. Therefore, to expand on (*ii*), above, we could say that many closure relations are unsatisfactory because of the poor understanding of the mechanisms that produce velocity and concentration fluctuations (19; 20). An example of such poor understanding is illustrated in Figure 1.5 where Zenit et al. (19) compared the experimental collisional pressure data against many different modeling approaches. Collisional pressure is a function of the fluctuating component of velocity for the solids phase (21; 22; 23).

The interactions that closure relations are meant to describe are very complex and obtaining physical models derived from basic principles is not feasible. Hence, reliable experimental data are required to understand the important physical mechanisms responsible for each of these parameters and to develop semi-empirical models that reasonably describe the key interactions.

One of the objectives of the present study is to produce reliable local experimental data that are required to improve our understanding of such complex phenomena and to develop new models that accurately predict the key parameters in solid-liquid flows. As mentioned previously, the two-fluid modeling approach seems to be the most appropriate for highly concentrated slurry flows. In order to determine the type of measurements that are required, the equations and closure relations comprising the two-fluid model are presented in the next section. It should be noted, though, that the types of experimental measurements described here are universally valuable. They are not designed just to improve two-fluid models.

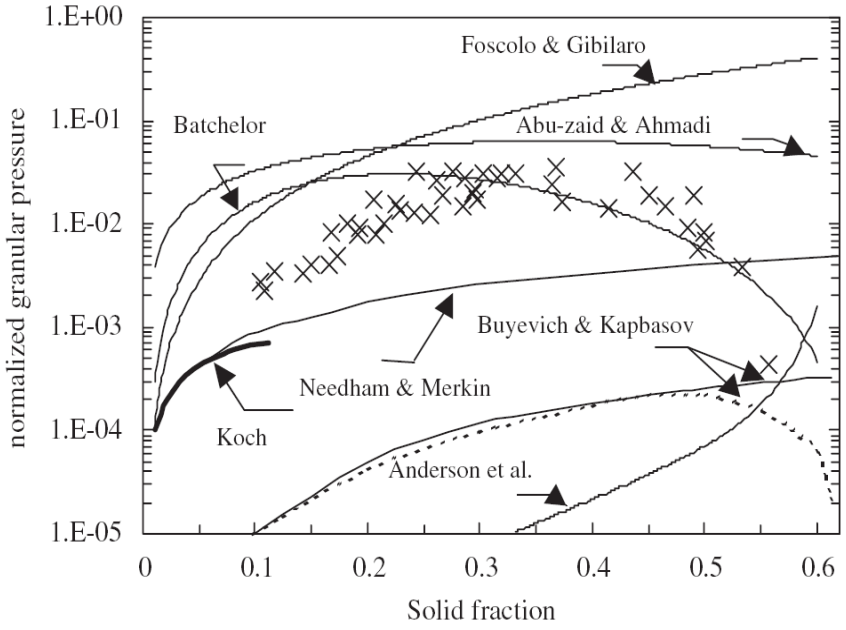

Figure 1.5: Comparison between experimental particle pressure measurements ($\times$) and theoretical models (solid and dashed lines) for 3 mm glass beads from Zenit et al.

1.1.3 The two-fluid model

The continuity and momentum equations, for the fluid and solids phases, with no interphase mass transfer, can be expressed as:

$$\frac{\partial(c_s\rho_s)}{\partial t} + \nabla\cdot(c_s\rho_s\mathbf{u_s}) = 0 \tag{1.1}$$

$$\frac{\partial(c_f\rho_f)}{\partial t} + \nabla\cdot(c_f\rho_f\mathbf{u_f}) = 0 \tag{1.2}$$

$$\begin{aligned}[\frac{\partial(c_s\rho_s\mathbf{u_s})}{\partial t} + \nabla.(c_s\rho_s\mathbf{u_s}\mathbf{u_s})] = [\nabla\cdot\mathbf{T_{sv}} + \nabla\cdot\mathbf{T_{st}}] - c_s\nabla p_f \\ + c_s[\nabla\cdot\mathbf{T_{fv}} + \nabla\cdot\mathbf{T_{ft}}] + c_s\rho_s\mathbf{g} + \mathbf{M_{si}}\end{aligned} \tag{1.3}$$

$$[\frac{\partial(c_f\rho_f\mathbf{u_f})}{\partial t}+\nabla\cdot(c_f\rho_f\mathbf{u_f}\mathbf{u_f})]=-c_f\nabla p_f+c_f[\nabla\cdot\mathbf{T_{fv}}+\nabla\cdot\mathbf{T_{ft}}]+c_f\rho_f\mathbf{g}+\mathbf{M_{fi}} \quad (1.4)$$

where p_f, $\mathbf{g}$ and c_s are pressure, gravity and solids volume fraction, respectively (23; 24).

Note that $\mathbf{T_{ft}}$ and $\mathbf{T_{st}}$ represent fluid and solids phase turbulent (Reynolds) stresses. The Reynolds stress tensors are extra stress terms which appear during the derivation of RANS equations (23; 25). The $\mathbf{M_{si}}$ and $\mathbf{M_{fi}}$ terms correspond to interphase forces.

Closure relations for the Reynolds stress, the solids phase stress tensor, interphase forces and pressure drop are required to solve this system of equations.

Reynolds stress

If one replaces the instantaneous velocities with a product of statistical mean values plus fluctuating values,$\mathbf{u_i}=\bar{\mathbf{U}}_\mathbf{i}+\acute{\mathbf{u}}_\mathbf{i}$, and then averages the N-S equations, the Reynolds Averaged equations of motion (RANS) are obtained. For instance, the x-component of the averaged continuity equation is :

$$\begin{aligned}\frac{\partial}{\partial t}\rho\bar{\mathbf{U}}_\mathbf{x}=-\frac{\partial\bar{P}}{\partial x}-(\frac{\partial}{\partial x}\rho\bar{\mathbf{U}}_\mathbf{x}\bar{\mathbf{U}}_\mathbf{x}+\frac{\partial}{\partial y}\rho\bar{\mathbf{U}}_\mathbf{y}\bar{\mathbf{U}}_\mathbf{x}+\frac{\partial}{\partial z}\rho\bar{\mathbf{U}}_\mathbf{z}\bar{\mathbf{U}}_\mathbf{x})\\-(\frac{\partial}{\partial x}\rho\acute{\mathbf{u}}_\mathbf{x}\acute{\mathbf{u}}_\mathbf{x}+\frac{\partial}{\partial y}\rho\acute{\mathbf{u}}_\mathbf{y}\acute{\mathbf{u}}_\mathbf{x}+\frac{\partial}{\partial z}\rho\acute{\mathbf{u}}_\mathbf{z}\acute{\mathbf{u}}_\mathbf{x})+\mu\nabla^2\bar{\mathbf{U}}_\mathbf{x}+\rho\mathbf{g_x}\end{aligned} \quad (1.5)$$

On the right hand side of the equation, new unknown terms arise ($\rho\acute{\mathbf{u}}_\mathbf{x}\acute{\mathbf{u}}_\mathbf{x}$, $\rho\acute{\mathbf{u}}_\mathbf{y}\acute{\mathbf{u}}_\mathbf{x}, \rho\acute{\mathbf{u}}_\mathbf{z}\acute{\mathbf{u}}_\mathbf{x}$), which are associated with the turbulent velocity fluctuations. They are called Reynolds Stresses. With the appearance of these new variables, the number of unknowns is greater than the number of equations. The problem now is finding relations for the Reynolds stresses. This problem is known as the "turbulent closure problem" and this is why turbulent models are required.

There are different turbulent models available for implementation, such as Reynolds Stress Model (RSM), Eddy-Viscosity Models (EVM), and Algebraic Reynolds Stress Models (ARSM)(16). The Reynolds stress model involves obtaining the Reynolds

stresses, $\rho\mathbf{\acute{u}_i\acute{u}_j}$, using differential transport equations. The exact Reynolds stress equation is (26)

$$\frac{D\overline{\mathbf{\acute{u}_i\acute{u}_j}}}{Dt} = -(\overline{\mathbf{\acute{u}_i\acute{u}_k}}\frac{\partial\bar{\mathbf{U}}_\mathbf{j}}{\partial x_k} + \overline{\mathbf{\acute{u}_j\acute{u}_k}}\frac{\partial\bar{\mathbf{U}}_\mathbf{j}}{\partial x_k}) - 2\nu\overline{\frac{\partial\mathbf{\acute{u}_i}}{\partial x_k}\frac{\partial\mathbf{\acute{u}_j}}{\partial x_k}} + \overline{\frac{p}{\rho}(\frac{\partial\mathbf{\acute{u}_i}}{\partial x_j} + \frac{\partial\mathbf{\acute{u}_j}}{\partial x_i})} - \{\frac{\partial}{\partial x_k}[\overline{\mathbf{\acute{u}_i\acute{u}_j\acute{u}_k}} - \nu\overline{\frac{\partial\mathbf{\acute{u}_i\acute{u}_j}}{\partial x_k}} + \overline{\frac{p}{\rho}(\delta_{jk}\mathbf{\acute{u}_i} + \delta_{ij}\mathbf{\acute{u}_j})}]\} + \mathbf{S_u} \quad (1.6)$$

This symbolically can be written as:

$$\mathbf{C_{ij}} = \mathbf{P_{ij}} - \boldsymbol{\varepsilon_{ij}} + \mathbf{D^p}_{ij} - \mathbf{D_{ij}} + \mathbf{S_u} \quad (1.7)$$

where $\mathbf{C_{ij}}$ is the material derivative term, $\mathbf{P_{ij}}$ is the generation term, $\boldsymbol{\varepsilon_{ij}}$ is viscous destruction, $\mathbf{D^p_{ij}}$ is transport by pressure fluctuations and $\mathbf{D_{ij}}$ is a diffusion term. The user-defined term, $\mathbf{S_u}$, allows for adding or subtracting additional terms.

The various EVM's are based on the analogy between the stress-strain relationships in laminar flow. These models use the Boussinesq eddy-viscosity assumption. There are zero-, one- and two-equation models. Algebraic turbulence models or zero-equation turbulence models do not require the solution of any additional equations, and are calculated directly from the flow variables. As a consequence, zero-equation models may not be able to properly account for history effects on the turbulence, such as convection and diffusion of turbulent energy. These models are often too simple for use in general situations, but can be quite useful for simpler flow geometries.

The most famous EVM is the $k-\varepsilon$ model, where k is the turbulence kinetic energy, which is defined as $k = \frac{1}{2}[\overline{(\mathbf{u_i'^2})} + \overline{(\mathbf{u_j'^2})} + \overline{(\mathbf{u_k'^2})}]$ or, in the other words, the sum of normal Reynolds stresses. In this model, ε is the rate of turbulence energy dissipation. The equations for these variables can be derived using transport equations and thus one is able to solve the RANS equations (16). The standard $k-\varepsilon$ model equations are (27):

$$\frac{\partial(\rho k)}{\partial t} + \frac{\partial(\rho k\mathbf{u_i})}{\partial x_i} = P_k - \rho\varepsilon + \frac{\partial}{\partial x_j}[(\mu + \frac{\mu_t}{\sigma_k})\frac{\partial k}{\partial x_j}] + S_{user} \quad (1.8)$$

and

$$\frac{\partial(\rho\varepsilon)}{\partial t}+\frac{\partial(\rho\varepsilon\mathbf{u_i})}{\partial x_i}=C_{1\varepsilon}\frac{\varepsilon}{k}(P_k+C_{3\varepsilon}P_b)-C_{2\varepsilon}\frac{\varepsilon^2}{k}+\frac{\partial}{\partial x_j}[(\mu+\frac{\mu_t}{\sigma_s})\frac{\partial\varepsilon}{\partial x_j}]+S_{user} \quad (1.9)$$

$$P_k=-\overline{\rho\acute{\mathbf{u}}_\mathbf{i}\acute{\mathbf{u}}_\mathbf{j}}\frac{\partial\mathbf{u_j}}{\partial x_i} \quad (1.10)$$

and

$$P_b=\beta\mathbf{g_i}\frac{\mu_t}{Pr_t}\frac{\partial\theta}{\partial x_i} \quad (1.11)$$

where θ is temperature and

$$\mu_t=\mu C_\mu\frac{k^2}{\varepsilon} \quad (1.12)$$

The constants in these equations are: $C_{1\varepsilon}=1.44$, $C_{2\varepsilon}=1.92$, $C_{3\varepsilon}=1.44(P_b>0), 0(P_b\leq 0)$, $C_\mu=0.09$ and $\sigma_s=1.3$.

We see that the equation describing k equation could be written as:

$$L_k+C_k=P_k-\rho\varepsilon+D_k+S_u \quad (1.13)$$

where L_k represents unsteady or time-dependent effects, C_k is the convection term, P_k the is production term, and D_k is the diffusion term. To validate the turbulence model using experimental data, we would need to measure fluid and solids velocity fluctuations.

Particle-Particle interaction forces

As mentioned previously, we need a closure relation for the solids phase pressure and viscous stress tensor. The solids phase stress tensor could be expressed as:

$$\mathbf{T_{sv}}=p_s\mathbf{I}+\mathbf{T_{coll}} \quad (1.14)$$

where

$$\mathbf{T_{coll}} = [\xi_s \nabla \cdot \mathbf{u_s} + \mu_s(\nabla \mathbf{u_s} + \nabla \mathbf{u_s}^T)] - \frac{2}{3} c_s \mu_s \nabla \cdot \mathbf{u_s} \tag{1.15}$$

According to Equation 1.15, we should find relations for p_s , ξ_s and μ_s , which are solids phase pressure, solids bulk viscosity and solids shear viscosity. There are two general classes of models for these quantities: empirical constitutive models and kinetic theory based models. The first class consists of empirical relations where the solids phase pressure, solids bulk viscosity and solids shear viscosity are expressed as a function of solids concentration (28). The most widely used constitutive relation for solids pressure is

$$\nabla p_s = G(c_s) \nabla c_s \tag{1.16}$$

and

$$G(c_s) = G_0[e^{-C_m(c_s - c_{max})}] \tag{1.17}$$

where G_0 is the reference elastic modulus, C_m is a compaction modulus and c_{max} is the maximum particle packing volume fraction (22; 24).

The second class of models is based on the kinetic theory of gases which can be used to derive relations for the solids phase stress. The relations p_s , ξ_s and μ_s are given as functions of solids concentration and granular temperature, where the term *granular temperature* is defined below.

Interparticle collisions induce random velocities that are reminiscent of the thermal motion of molecules. The magnitude of fluctuating velocities is called granular temperature (T) and can be expressed as:

$$T = \frac{1}{3} \Sigma(\overline{\mathbf{u_s^{'2}}}) \tag{1.18}$$

It is a measure of the fluctuating velocity of the solids phase (21; 22; 23). This concept was introduced by Ogawa in 1987 (29). The effective pressure based on this model could be expressed as:

$$p_s = c_s \rho_s T(1 + 2c_s g_0(1 + e)) \tag{1.19}$$

Here, e is the coefficient of restitution for particle–particle collisions and g_0 is the radial distribution function which describes the variation of density of surrounding matter with respect to a specific point as a function of distance. The coefficient of restitution represents the loss of energy due to collision and has a value between 0 and 1. The coefficient of restitution is 1 for elastic collisions with no energy loss (28; 29).

There are different models for the radial distribution function, such as the Lun and Savage model (30):

$$g_0 = \left(1 - \frac{c_s}{c_{max}}\right)^{-2c_{max}} \tag{1.20}$$

and the Gidaspow model (22):

$$g_0 = \frac{3}{5}\left(1 - \left(\frac{c_s}{c_{max}}\right)^{\frac{1}{3}}\right)^{-1} \tag{1.21}$$

The kinetic theory form of the bulk viscosity ξ_s is (28)

$$\xi_s = \frac{4}{3} {c_s}^2 \rho_p d_p g_0 (1 + e)\sqrt{\frac{T}{\pi}} \tag{1.22}$$

where d_p is particle diameter. The shear viscosity relation has two contributions. It is the sum of turbulent viscosity and collisional viscosity. The relation for solids shear viscosity is

$$\mu_s = \mu_{s,col} + \mu_{s,kin} \tag{1.23}$$

There is broad agreement on the description of the collisional part but many different proposals for the kinetic part. The collisional viscosity term is proportional to the square root of granular temperature, as in the kinetic theory of gases. The general equation for $\mu_{s,col}$ is

$$\mu_{s,col} = \frac{4}{5} {c_s}^2 \rho_s d_p g_0 (1+e) \sqrt{\frac{T}{\pi}} \tag{1.24}$$

One example of an expression for the kinetic viscosity part comes from the Lun and Savage model (30):

$$\mu_{s,kin} = \frac{5\sqrt{\pi}}{96} \rho_s d_p \left(\frac{1}{\eta g_0} + \frac{8}{5} c_s \left(\frac{1 + \frac{8}{5}\eta(3\eta - 2) g_0 c_S}{2 - \eta} \right) \right) \sqrt{T} \tag{1.25}$$

where

$$\eta = \frac{1}{2}(1+e) \tag{1.26}$$

From the Gidaspow model (22):

$$\mu_{s,kin} = \frac{5\sqrt{\pi}}{48} \frac{\rho_s d_p}{(1+e) g_0} \left(1 + \frac{4}{5}(1+e) g_0 c_s \right)^2 \sqrt{T} \tag{1.27}$$

Equations 1.19 to 1.27 show that the models for particle-particle interaction forces are function of solids bulk properties such as particle size and density, solids concentration distribution and granular temperature which, by definition, is a product of solids velocity fluctuations. Consequently, experimental measurements of solids velocity fluctuations and time-averaged concentration distributions are needed to validate the solids phase pressure closure.

Interphase forces

Interphase forces consist of different contributions, and could be stated as:

$$\mathbf{M_{ik}} = \mathbf{M_{ik}^D} + \mathbf{M_{ik}^L} + \mathbf{M_{ik}^{VM}} + \mathbf{M_{ik}^W} \qquad (k = s, f) \tag{1.28}$$

where $\mathbf{M_{ik}^D}$, $\mathbf{M_{ik}^L}$, $\mathbf{M_{ik}^{VM}}$ and $\mathbf{M_{ik}^W}$ are interphase drag, lift, virtual mass and wall forces respectively. The interphase drag forces are generally dominant and the effect of the other forces can be neglected. The interphase drag force could be expressed as :

$$M_{ik}^D = \beta(\mathbf{u_l} - \mathbf{u_k}) \qquad (k = s, f; l = s, f) \tag{1.29}$$

and

$$\beta = \frac{3}{4} C_D \frac{\rho_f c_s (1 - c_s) |\mathbf{u_f} - \mathbf{u_s}|}{d_p} \tag{1.30}$$

Here, β is the fluid-particle friction coefficient and C_D is the standard drag coefficient (22). There are many different relations for the standard drag coefficient given for different flow conditions. Examples of these relations for dense, distributed solids particles (which is our case) are the Wen and Yu model (31)

$$C_D = \begin{cases} \frac{24}{Re_p}[1 + 0.15(Re_p)^{0.687}](1 - c_s)^{-2.65} & \text{if } Re_p < 1000 \\ 0.44 & \text{if } Re_p \geq 1000 \end{cases} \tag{1.31}$$

and the Gidaspow model (22)

$$C_D = \begin{cases} \frac{24}{Re_p}[1 + 0.15(Re_p)^{0.687}](1 - c_s)^{-2.65} & \text{if } C_f > 0.8 \\ 150\frac{{c_s}^2 \mu_f}{c_f {d_p}^2} + 1.75\frac{c_s \rho_f |\mathbf{u_f} - \mathbf{u_s}|}{d_p} & \text{if } C_f < 0.8 \end{cases} \tag{1.32}$$

Note that

$$Re_p = \frac{(1 - c_s)\rho_f |\mathbf{u_f} - \mathbf{u_s}| d_p}{\mu_f} \tag{1.33}$$

is the particle Reynolds number. Measurement of time-averaged solids and fluid velocities and solids concentration profiles is required to validate the drag closure relations.

Required measurements

Validation of model predictions using experimental data is critical. The first step, before doing any experiments, is to clarify the kind of measurements we need to make. Based on the description provided in the previous section (the two-fluid model as an example of a multiphase flow computational method), we need to measure the following parameters:

1- Time-averaged concentration distributions

2- Time-averaged velocity distributions

3- Concentration fluctuations

4- Velocity fluctuations

The velocity fluctuations measurements could be used in the validation of Reynolds stress and solids phase stress closures. The velocity and concentration distributions could also be used in the validation of solids phase stress and interphase drag closures.

1.2 Experimental methods in multiphase flow

Experimental measurements in multiphase flow processes are not only important in research programs, but also in industrial processes for quality control and flow characterization purposes. Typical parameters of interest in dispersed two phase flows are (1):

1- Particle size and size distribution

2- Particle concentration

3- Particle and fluid velocity

A wide range of measurement techniques have been developed for measuring multiphase flow parameters. However, selecting the right technique for a particular system is critical. Generally, the selection is a function of system geometry, flow conditions and component properties.

There are two main measurement categories for multiphase flows: (1) sampling methods and (2) online measurement techniques. Sampling methods are usually used to measure parameters such as particle size distribution, particle shape and particle concentration. The most important point is that as the sample should be representative of the bulk of the flow. The common sampling method that is widely used in multiphase flows is isokinetic sampling for particle concentration measurements. One of the disadvantages of the sampling methods used in flow applications is their intrusive nature.

Online measurements are also divided into *integral methods* and *local measure-*

ment techniques. Integral methods give time-resolved spatial averaged information whereas local measurement techniques provide information with a specific spatial resolution. Laser Doppler Velocimetery (LDV) and Particle Image Velocimetry (PIV) are examples of integral methods and local measurements techniques, respectively.

Common single and dilute multiphase flow measuring techniques, such as LDV, PIV, and PTV (Particle Tracking Velocimetry) are widely used for transparent flows and/or flows where the solids concentration is low. However, their capabilities in highly concentrated and opaque flows, such as dense slurry flows, are debatable (32).

Advances in measurement techniques in recent years, especially tomography methods, have opened a new window in the experimental study of multiphase flows. The most important advantage of these methods is their ability to perform in concentrated and opaque systems. Tomography involves the use of arrays of sensors on the periphery of an object to obtain cross sectional images of the sensing zone and it could be categorized as an online local measurement technique. There are various types of tomography sensors, such as NMR (Nuclear Magnetic Resonance)(33; 34), ultrasonic, electrical (35), X and gamma ray (7; 36) and MRI (Magnetic Resonance Imaging) (32; 36), which could be used for measuring flow parameters even at high concentrations. Electrical tomography is applicable for concentrated solid–liquid flow. It appears to be sufficiently fast and robust enough for concentrated particle-fluid flow applications (32; 36; 37). Numerous studies have been conducted where electrical tomography techniques are used on fluid-particle systems, such as pneumatic conveying of granular solids (38; 39), flow distribution and velocity measurement in a fixed bed reactor (40), hydraulic conveying of materials (41), and fluidization (42). The results of these studies show that electrical tomography is a suitable method for applications in concentrated particle-fluid flows. Electrical Impedance Tomography (EIT) is the measurement method of choice for the present study.

1.3 Fluidized beds vs. slurry pipelines

Fluidized beds provide an ideal opportunity to study solid-liquid flows, particularly fluid-particle and particle-particle interactions. The great advantage of solid-liquid fluidized beds over slurry pipeline systems is their capability of producing nearly homogeneous two-phase flow over a wide range, from very dilute to highly concentrated mixtures (20). Numerous experimental studies have been conducted on liquid fluidized beds and different parameters such as collisional pressure, solids concentration fluctuations and liquid velocity fluctuations (19; 20; 43; 44) have been investigated. Although the cited works provided important insight into highly concentrated solid-liquid system behaviour, the measurements were limited to cross-sectional averaged values with no information on the concentration and velocity fluctuation distributions within the flow domain. Such local information is important especially in determining the mechanism(s) responsible for producing these fluctuations (e.g. particle-wall interactions). In the present study, variations of the fluctuations over the flow domain have been measured in both slurry pipelines and in liquid-solid fluidized beds.

1.4 Research objectives

The purpose of the present study is:

a) To develop energy consumption models based on existing phenomenological slurry flow models and to evaluate their performance under different flow conditions;

b) To collect novel, local experimental data for highly concentrated solid-liquid flows; and

c) To expand the understanding of the mechanisms that govern these complex flows.

The objectives are met through the completion of the following activities:

1- Using two different phenomenological models for fine and coarse particle slurries, the effect of slurry concentration, mixture velocity and particle size (where applicable) on Specific Energy Consumption (SEC) will be evaluated. Model predic-

tions will be compared with experimental results.

2- Develop a measurement procedure to obtain local, instantaneous solids velocity and concentration distribution maps in highly concentrated solid-liquid flows. The specific focus will be on the use of Electrical Impedance Tomography.

3- Perform a set of experiments in horizontal slurry pipelines to study the fluid-particle interactions in highly concentrated solid-liquid flows where the solids concentration distributions are (i) uniform or (ii) nonuniform, depending on flow conditions.

4- Perform a set of experiments using a solid-liquid fluidized bed to study the particle-particle and particle-wall interactions at various solids concentrations and evaluate the performance of existing modeling approaches.

5- Expand and modify the the modeling framework available for liquid fluidized beds to slurry pipe flows where the solids are not uniformly distributed.

1.5 Contribution of the present study

One of the important contributions of the present study is the development of a measurement procedure to study highly concentrated solid-liquid mixtures. This procedure allows for the instantaneous measurement of solids distributions in concentrated and opaque solid-liquid mixtures. The method allows for a two dimensional measurement which produces more detailed information about the flow than previous measurements, which produced only cross-sectional averages.

Another important contribution of this project is to present new information on fluid-particle and particle-particle interactions by implementing signal processing methods in analyzing concentration and velocity fluctuations of the dispersed phase at high concentrations.

From an industrial viewpoint, the present study provides basic information that is required to develop a more efficient pipeline process. As an example, the erosion of slurry pipelines is important in many industries. The capital investments in pipe are often substantial and predictions of wear rates are needed for economic analysis.

Measurement using actual pipeline flow especially for large particles is impractical and reliable simulation methods are needed. Improved understanding of the slurry flow fundamentals developed here is a key contribution toward the development of reliable simulation and scale-up methods for such processes.

1.6 Thesis outline

This dissertation is organized in a paper-based format; with Chapters 2 through 4 each based on manuscript(s) submitted or accepted for publication.

Chapter 2 addresses energy consumption in slurry pipelines. This chapter discusses the development of energy consumption models and the SEC concept is used to determine the optimum operating conditions for slurry pipelines. The effect of various parameters, such as pipe diameter, particle size and mixture velocity on the optimum operating condition is investigated. The performance of two energy consumption models is also compared against a wide range of experimental investigations.

Chapter 3 introduces the measurement procedure used to obtain two-dimensional solids instantaneous velocity and concentration distributions at high solids concentrations. The procedure involves obtaining high speed data using an EIT device (typically electrical conductivity or solids concentration) and converting them to solids concentration fluctuations and turbulent intensity using advanced signal processing methods. The procedure is then applied to measure solids concentration fluctuations and turbulent intensity distributions for slurry flow in a horizontal pipeline allowing for a novel study of fluid-particle interactions. The findings compare favourably to existing modeling schemes and experimental data.

In Chapter 4, the novel method developed in Chapter 3 is used to study a solid-liquid fluidized bed. Measurement of solids concentration and concentration fluctuation distributions allows for the study of the local dynamic behaviour of a liquid fluidized bed and for the investigation of particle-particle and particle-wall interac-

tions. The experimental findings are also compared against numerical and empirical models that can be found in the literature.

Chapter 5 includes a summary and a detailed list of the important conclusions that arise from the present study. Recommendations for extending the research through future studies are also made in this chapter.

2

Specific energy consumption and desirable operating conditions for settling slurries

Material in this chapter has been published in: *Hashemi, S.A., Wilson, K.C., Sanders, R.S., (2010). "Specific energy consumption and desirable operating conditions for fine-particle slurries". Hydrotransport 18, Rio de Janeiro, Brazil.*
and submitted for publication to: *Hashemi, S.A., Wilson, K.C., Sanders, R.S., (2013). " Specific energy consumption and operating condition for coarse-particle slurries". Powder Technology.*

2.1 Introduction

Solid-liquid (slurry) flows are widely used in many industrial processes and determining the optimum flow condition is an important factor in pipeline design and operation. Slurry flows are generally divided into two groups based on fluid and particle characteristics: non-settling or homogenous, and settling or heterogeneous slurry flows (13).

One of the important factors in determining the operating condition for a slurry flow is energy consumption. The Specific Energy Consumption (SEC) is a measure of energy required to transport a unit mass of solids over a unit pipeline length and

can be written as:

$$SEC = \frac{i_m}{S_s C_{vd}} \tag{2.1}$$

where i_m, S_s and C_{vd} are hydraulic gradient, relative solids density (solids to fluid density ratio) and delivered concentration. Lower SEC values represent more energy-effective operation and consequently, more efficient transport (3). The hydraulic gradient is the frictional head loss in terms of the height of a column of carrier fluid per unit length of pipe and is defined as:

$$i_m = \frac{1}{\rho_f g}\left(-\frac{\Delta p}{\Delta x}\right) \tag{2.2}$$

where $(-\frac{\Delta p}{\Delta x})$ and ρ_f are the pressure drop per unit length of pipe and fluid density, respectively. The pressure gradient could also be expressed as the column height of slurry per unit length of pipe, j_m, which can be written as:

$$j_m = \frac{1}{\rho_m g}(-\frac{\Delta p}{\Delta x}) \tag{2.3}$$

where ρ_m is the density of the mixture and is a linear function of solids volume concentration (C_s).

$$\rho_m = \rho_s C_s + \rho_f(1 - C_s) \tag{2.4}$$

An accurate prediction of SEC for a slurry flow relies on having a reliable model to calculate hydraulic gradient or pressure gradient. In this study, performance of two different models for fine and coarse particle slurries in determining SEC is investigated.

2.2 Fine-particle slurries

The slurries of interest here are aqueous mixtures of fine particles, typically 100 microns or smaller, but not so small as to cause significant non-Newtonian viscous

effects.

The pressure drop of this type of mixture is satisfactorily predicted using the equivalent-fluid model for most operating conditions of industrial importance. In the equivalent-fluid model, the effect of the solids on the slurry friction factor is neglected and it is assumed that the pressure gradient is generated by a fluid with the density of the mixture. As a result, the hydraulic gradient for a homogenous mixture is

$$i_m = S_m i_w \tag{2.5}$$

where S_m is the relative density of the mixture and i_w is the hydraulic gradient for the flow of fluid alone under identical conditions (i.e. velocity, pipe diameter).

In terms of energy consumption, it is desirable to operate a pipeline at the minimum SEC, as lower SEC values represent more energy-effective operations (3).

Combining Equations 2.5 and 2.1 results in:

$$SEC = \frac{S_m i_m}{S_s C_{vd}} \tag{2.6}$$

Single-phase hydraulic gradient, i_w can also be written as:

$$i_w = \frac{f_w}{2D_g} V^2 \tag{2.7}$$

As a result, SEC can be written in terms of velocity and pipe diameter using the equivalent fluid model as:

$$SEC = \frac{S_m f_w}{2DgC_{vd}S_s} V^2 \tag{2.8}$$

As shown in Equation 2.8, SEC is directly proportional to the square of mixture velocity and inversely proportional to the pipe diameter and solids concentration for a specific type of solids (constant S_s). It is worth mentioning that there are constraints for solids concentration (maximum packing fraction) and mixture velocity (minimum operating velocity or the deposition velocity) that should be considered along with the SEC to find the optimum operating condition. In the next section, the effects

of solids concentration, mixture velocity and pipe diameter on SEC are studied by analyzing a number of previously published experimental data.

2.2.1 Results and discussion

Data presented here are from experimental works carried out at the Saskatchewan Research Council (SRC) Pipe Flow Technology Centre (13; 45) and by Korving (46). Table 2.1 shows the details of these experiments.

Table 2.1: Details of experimental data sets.

Data set	Experiments	Solids	d_p (μm)	D (mm)	V (m/s)	C_s (v/v)%	ρ_s (kg/m^3)	ρ_f (kg/m^3)
1	(13)	sand	90	103	1–5	19–33	2650	998
2	(46)	sand	100	155	1.5–4	18–48.5	2650	1000
3	(45)	sand	90	160	1.8–5	13.9–39.3	2655	1000
4	(45)	sand	90	50	1.5–5	15–40	2655	1000
5	(45)	sand	90	160	1.25–5	15–40	2660	1000
6	(45)	Glass bead	85	160	1.25–5	15–40	2441	1000

Figure 2.1 shows the Gillies et al. data i.e. data set 1. It can be seen from the figure that the equivalent-fluid model shows good agreement with the experimental data for a certain range of particle concentrations and mixture velocities. We will explore the utility of the equivalent-fluid model in calculating SEC for slurries of this type.

Effect of solids concentration on SEC

To study the effect of solids concentration on SEC, pressure gradient measurements in all experimental data sets are used to calculate SEC. The SEC versus concentration plot is obtained for each velocity. The results presented here are typical of those obtained from this analysis and thus SEC values for all conditions are not plotted.

Figures 2.2 and 2.3 show the effect of concentration on SEC for data sets 3 and 6. It can be seen that SEC values decrease with increasing concentration up to a concentration around 30%. Further increases in concentration result in SEC aug-

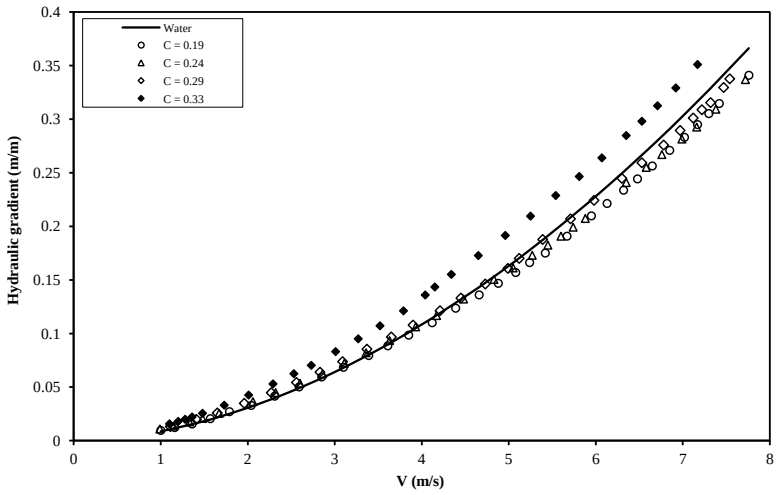

Figure 2.1: Hydraulic gradient versus mixture velocity for data set 1

mentation. This behavior can be observed for each data set, except for Korving's data. Solids concentration alters SEC as a consequence of two competing effects. On one hand, the increase in solids concentration increases the delivered solids concentration which results in decreasing SEC. On the other hand, the increase in solids concentration causes the hydraulic gradient (and consequently the SEC) to rise. At lower solids concentrations, the increase in solids delivered concentration has a more profound effect on SEC values. As solids concentration increases, particle dispersive stresses are becoming more important and the rate of increase in hydraulic gradient goes up. As a result of these two competing effects, an optimum solids concentration exists at which SEC is a minimum.

The effect of solids concentration on SEC for Korving's data (set 2) is shown in Figure 2.4. It can be seen from this figure that there are no experimental data between solids concentrations of 18% and 36%, where the minimum SEC value for other data sets is located. Comparison of Korving's data with Schaan's 160 mm pipeline data (which are almost identical) highlight this more clearly. Figure 2.5 and

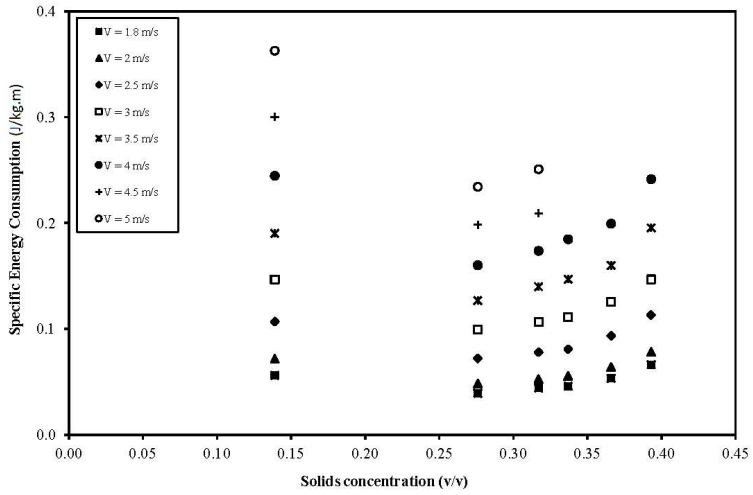

Figure 2.2: Change in SEC with concentration for data set 3

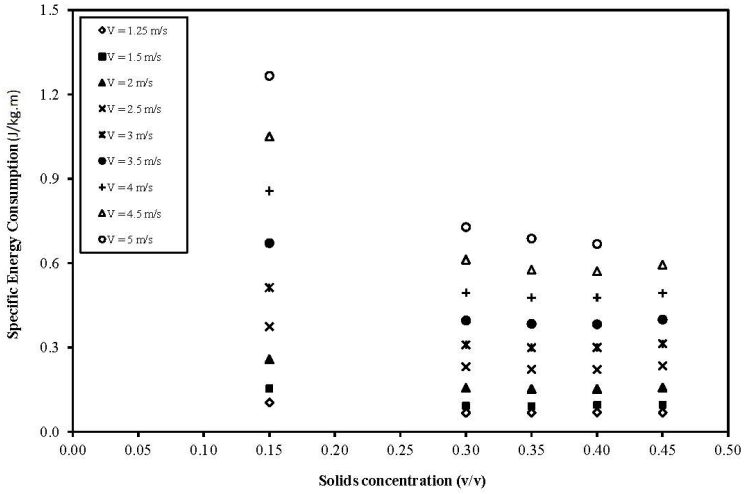

Figure 2.3: Change in SEC with concentration for data set 6

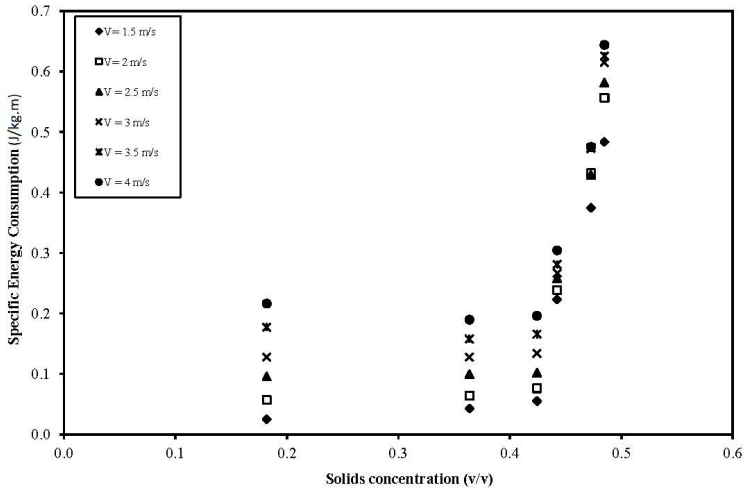

Figure 2.4: Change in SEC with concentration for data set 2

2.6 show SEC vs. concentration plots for these two data sets at 2 and 4 m/s.

Another interesting feature arising from analysis of Korving's data is a very sharp increase in SEC at $C_s > 0.45$. This behavior was not observed in other data sets as they did not extend to such high concentrations. To have an energy-effective transport, this range of concentrations should be avoided. It is expected that other data sets would show similar behavior if experiments had been done at higher concentrations. It is also worth pointing out that Korving's solids have wider particle size distribution ($d_{10} = 0.063\ mm$, $d_{50} = 0.103\ mm$, $d_{90} = 0.250\ mm$) compared to Schaan's particles which have narrow size distribution with $d_{50} = 0.09$ mm.

Effect of pipe diameter on SEC

Figures 2.7 and 2.8 compare the SEC values for data sets 1, 3 and 4 at 2 m/s and 5 m/s, respectively. The results show that the minimum SEC value is greater for smaller pipe diameters. For single-phase flows, it is well known that the frictional pressure drop increases with decreasing pipe diameter at constant velocities. As

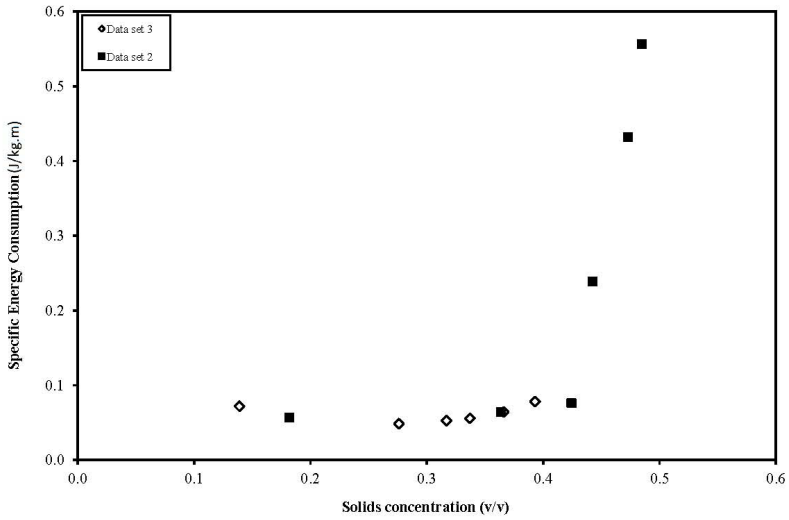

Figure 2.5: Comparison of Korving's and Schaan's data at V = 2 m/s

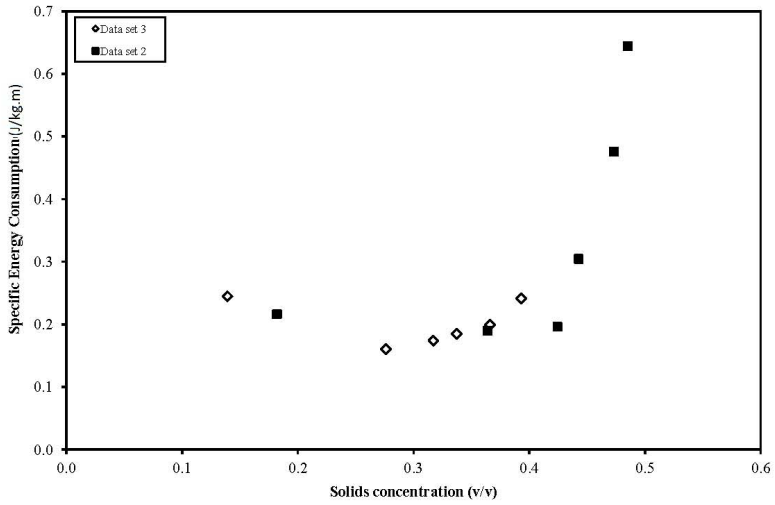

Figure 2.6: Comparison of Korving's and Schaan's data at V = 4 m/s

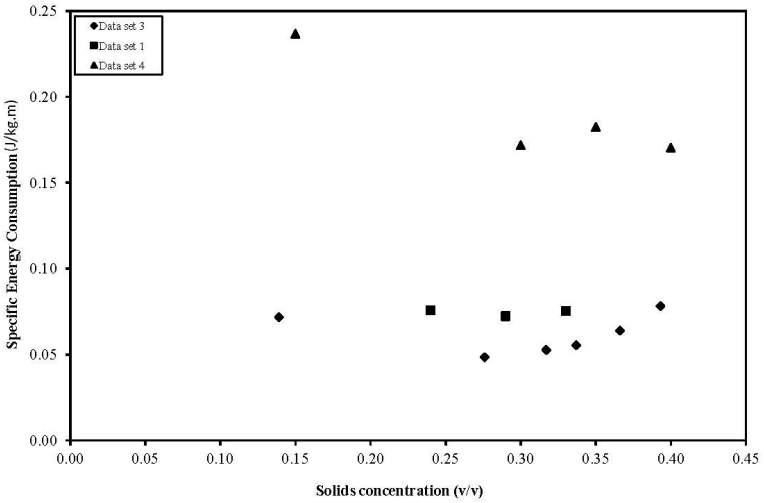

Figure 2.7: Effect of pipe diameter on SEC (data sets 1, 3 and 4 at V = 2 m/s)

mentioned earlier, homogeneous slurry mixtures behave rather similarly to an equivalent fluid and their pressure gradients can be estimated using the equivalent-fluid model. As a result, the effect of pipe diameter on pressure loss for these mixtures follows a trend similar to that of a single phase flow. Analysis of the pipe diameter effect for other mixture velocities shows the expected results.

Effect of mixture velocity on SEC

It is evident from Figures 2.2 to 2.4 that the minimum SEC for a specific mixture will increase with velocity. Figure 2.9 shows the change in SEC with mixture velocity at constant concentration for data sets 1 and 5. The concentrations selected here represent the value at which the minimum SEC occurs for each data set. This trend could also be described by implementing the equivalent-fluid model. For equivalent-fluid flows, assuming all flow properties are constant except for mixture velocity, the pressure gradient (and as a result, the hydraulic gradient, i_m) keeps rising with velocity. Consequently, SEC values are greater at higher velocities.

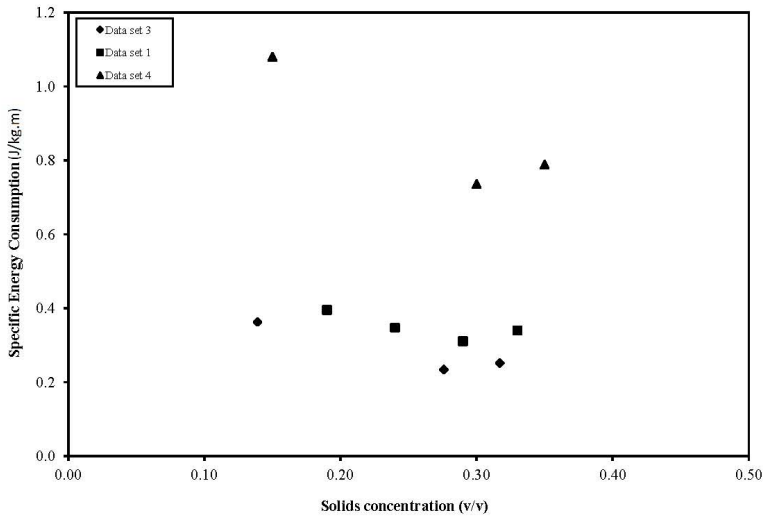

Figure 2.8: Effect of pipe diameter on SEC (data sets 1, 3 and 4 at V = 4 m/s)

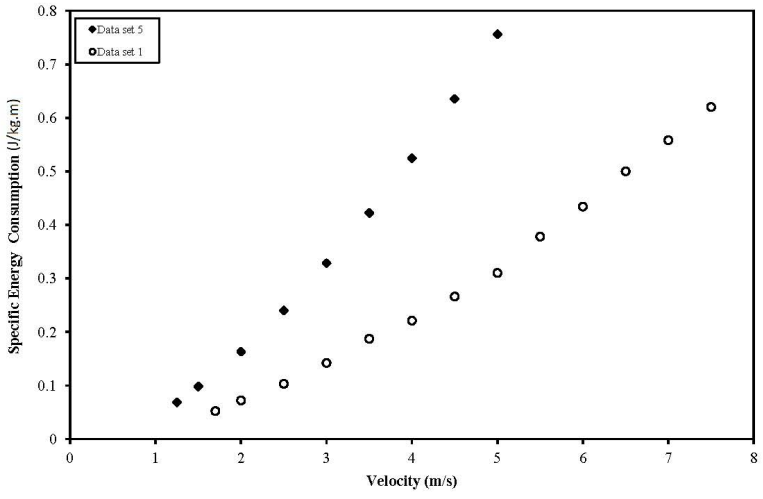

Figure 2.9: Effect of mixture velocity on SEC at $C_s = 0.3$

Table 2.2: Experimental data and Equivalent-Fluid model (EF) predictions of SEC at (V_{min}, C_{smin})

Data set	Minimum velocity available from experimental data(V_{min})	Minimum SEC at V_{min} (Experimental)	Concentration at minimum SEC (C_{smin})(Experimental)	Predicted SEC at V_{min},C_{smin} using EF model
1	1.7	0.052	0.29	0.050
3	1.8	0.039	0.28	0.033
4	1.5	0.100	0.31	0.094
5	1.25	0.068	0.31	0.068
6	1.25	0.067	0.30	0.073

The optimum operating condition

As pointed out earlier, SEC is not the only parameter that should be considered in determining the optimum flow condition. Maximum packing fraction (C_{max}) and deposition velocity (V_c) are two important factors that also need to be considered. Maximum packing fraction (C_{max}) is considered to be a given value for a particular slurry and should be determined experimentally (2). A value of $C_{max} = 0.6$ can be taken for mono-dispersed spherical particles when no experimental data for the particles is available (47). However, C_{max} decreases substantially when the particles are angular: for example, the sand used to prepare slurries for data sets 1 and 3 had a $C_{max} = 0.51$ (13; 45).

Table 2.2 shows the deposition velocities at solids concentration equal to 30% for all six data sets. The SRC model (2; 8) has been used for deposition velocity calculations. The SEC analysis shows that optimum operating concentration for these slurries is around 30%. The desirable operating velocity should be determined by considering the minimum deposition velocity for the mixture.

2.2.2 Verification of model with experimental data

Wilson et al. (3) considered two models for pipeline flow - the equivalent-fluid model and the heterogeneous model. The parameter that determines which model is to be used is the dimensionless particle diameter d^+, defined as $\frac{\rho u^* d}{\mu}$. Here ρ and μ are fluid density and viscosity, d is particle diameter and u^* is shear velocity. u^* can be written as:

$$u^* = V\sqrt{\frac{f_w}{8}} \tag{2.9}$$

where, f_w is Moody friction factor for equivalent flow of water at the mixture velocity.

For small values of d^+ (typically below 9) the particles are enclosed in the viscous sub-layer, the criterion for equivalent-fluid flow. This is the condition of interest in section 2.2.

Larger values of d^+ indicate heterogeneous flow, which requires a different model. The case of intermediate-particle slurries was studied by Wilson and Sellgren (48).

The equivalent-fluid model does not give a minimum in SEC, which increases monotonously with velocity. As mentioned previously, it is desirable to operate a pipeline at velocities slightly higher than deposition velocity. Minimum velocities at which experiments have been done for each data set, which were greater than the deposition velocity for each system, were selected as optimum operating conditions for comparison with model predictions. Note that it is possible to operate a pipeline of these mixtures even at lower velocities (See Table 3). Here, experimental data collected at a mixture velocity nearest V_c were selected as the minimum available velocity, specifically for model verification purposes. As there is no minimum for Korving's data at V = 1.5 m/s, this data set is excluded from our analysis. Table 2.2 shows a comparison between experimental data and model predictions for the other five data sets. The results show good agreement between experimental data and model predictions. Table 2.3 shows the equivalent-fluid model predictions of SEC for mixture velocities equal to $1.15V_c$ and solids concentration of 30%.

Next, the model performance in predicting the effect of velocity on SEC was evaluated at constant concentrations. The concentration values obtained from the first section, at which minimum SEC occur, were employed for calculations. Comparison of model predictions and experimental data for data sets 1 and 5 is illustrated in Figures 2.10 and 2.11, respectively. The results show good agreement between

Table 2.3: Deposition velocities and equivalent fluid model SEC prediction at $C_s = 0.3$)

Data set	V_c m/s	$1.15V_c$ m/s	Predicted SEC at $1.15V_c$, $C_s = 30\%$
1	1.04	1.20	0.026
2	1.21	1.39	0.018
3	1.10	1.27	0.015
4	0.95	1.10	0.047
5	0.91	1.05	0.043
6	0.83	0.95	0.038

experimental results and equivalent-fluid model predictions.

2.3 Coarse-particle slurries

For larger particles, or for very high concentrations of the fine particle (but still settling) slurries, the equivalent fluid model fails because particle-related friction loss must be considered. Two major frictional loss mechanisms in these coarse particle slurry flows are: (1) particle dispersive stresses and (2) Coulombic or contact–load friction. The particle dispersive stresses are caused by shear–related particle interactions. Shearing the closely-spaced particles generates a normal stress which can be correlated to shear rate, solids concentration and particle size (15). These forces tend to drive particles toward the pipe wall. They are strongly dependent on particle concentration and are dominant at high solids concentrations. The Coulombic stress is due to particles which are not suspended by fluid turbulence. The immersed weight of non-suspended particles is supported through particle contact with the pipe wall. This force is strongly dependent on particle size and insensitive to pipeline velocity (7) when particles are very coarse.

Durand and Condolios (4) developed a relation for calculation of hydraulic gradient for heterogeneous slurries. They represented the hydraulic gradient by using a dimensionless parameter Φ , defined as:

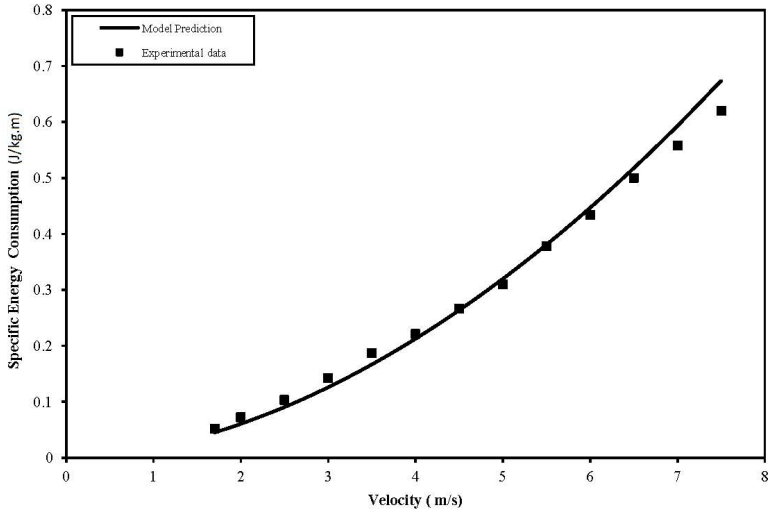

Figure 2.10: Comparison of model prediction with experimental data at constant concentration (data set 1, $C_s = 0.28$)

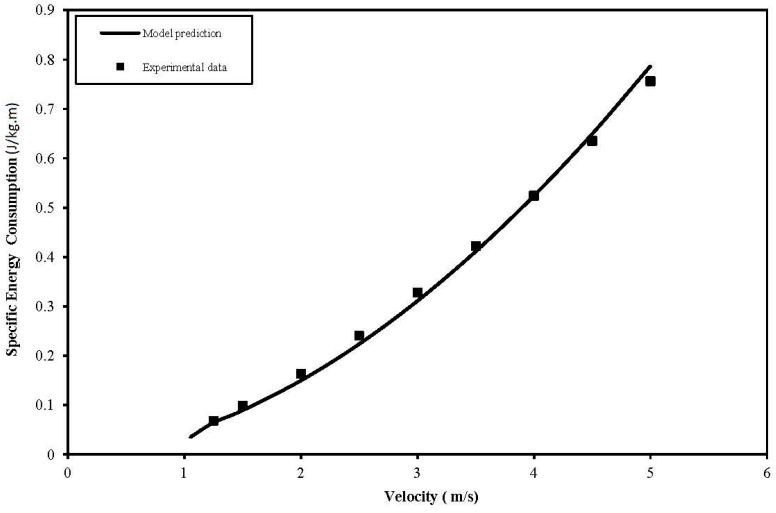

Figure 2.11: Comparison of model prediction with experimental data at constant concentration (data set 5, $C_s = 0.28$)

$$\Phi = \frac{i_m - i_w}{C_{vd} i_w} \tag{2.10}$$

where i_w is the hydraulic gradient for the single phase flow of the fluid under identical conditions (i.e. velocity, pipe diameter). They related Φ to another dimensionless variable, Ψ which is defined as :

$$\Psi = \frac{{V_m}^2}{gD(S_s - 1)} \sqrt{C_D} \tag{2.11}$$

where V_m and C_D are the mixture velocity and particle drag coefficient, respectively. Newitt et al. (5) suggested that for heterogeneous slurries the hydraulic gradient can be obtained using the stratification ratio, provided that $V_m < 17 v_t$ where v_t is the particle terminal settling velocity. The stratification ratio, R, is expressed as:

$$R = \frac{i_m - i_w}{S_m - 1} \tag{2.12}$$

where S_m is relative mixture density (ρ_m / ρ_f). They proposed that for these types of slurries the stratification ratio is constant and is equal to 0.8. In this case the main problem is the fact that the hydraulic gradient is not a function of particle size. Gibert (49) developed the following expression for determining hydraulic gradient in heterogeneous slurries. He proposed that:

$$i_m = i_w(1 + C_t \varphi) \tag{2.13}$$

where C_t is the solids volumetric concentration and φ is:

$$\varphi = 180 \left\{ \frac{V^2}{gD} \sqrt{C_x} \right\}^{-\frac{3}{2}} \tag{2.14}$$

The parameter C_x is a fictitious drag coefficient and expressed as:

$$\sqrt{C_x} = \sqrt{\frac{g d_p}{v_t}} \tag{2.15}$$

where d_p is particle diameter. He analyzed the energy consumption in a slurry flow and found that the energy consumption is inversely proportional to the velocity and has its lowest value at a point which has the minimum value in the hydraulic gradient versus pipeline velocity curve.

Although these models were mostly correlations based on many experimental results, and some of the functionalities were not correct, they provide valuable insight into the modeling and design of slurry pipelines.

Extensive analysis of heterogeneous slurries at Queen's University (50; 51) and Saskatchewan Research Council (SRC) Pipe Flow Technology Centre (13; 8) resulted in the further development of slurry flow models, such as the SRC Pipe Flow model. These models mainly capture the contributions of particle dispersion by fluid turbulence and Coulombic friction.

The concentration profiles predicted by these models show a monotonic increase in concentration toward the bottom of the pipe in horizontal flows. Experimental results for horizontal slurry flows of coarser particles obtained by various researchers (10; 52; 53) showed solids concentration profiles where the maximum concentration occurred up from the pipe invert rather than occurring right at the pipe invert. These results contradicted the prediction of the models and showed that another significant mechanism(s) is/are responsible for driving particles away from the wall.

Wilson et al. (11; 12) suggested that at high velocities, particles experience a lift force which results in particle migration away from the wall. They believed that this force is effective only near the wall. It is strongly dependent on the shape of the fluid velocity profile and the ratio of the particle diameter to viscous sublayer thickness. As well, the effect of this near-wall lift force is greatest for coarse particles at high velocities.

Wilson et al. (47) developed a new model for heterogeneous slurry flows which includes the near-wall lift force. In their model they mainly focused on the near-wall region and neglected the core of the flow since the main resistance to flow occurs near the pipe wall. They found good agreement between the model prediction and

a large body of experimental data.

In the following section, the Wilson et al. (47) model is used to determine the SEC and optimum operating condition for coarser particle, heterogeneous slurry flows. The slurries of interest are heterogeneous slurries of coarse solids with particle diameters greater than 150 μm. Effects of different parameters such as particle size, pipe diameter, solids concentration and mixture velocity on SEC and optimum operating conditions are investigated.

2.3.1 Analysis

The heterogeneous model which is the focus of the present analysis is applicable to solid-liquid mixtures containing larger particles where the turbulence dispersion force does not fully maintain the particle suspension, resulting in asymmetric concentration profiles. Wilson et al. (47) proposed that for this type of slurry flow, the stratification ratio (R) could be obtained using:

$$R = \frac{1}{\theta C_L} \tag{2.16}$$

where θ is expressed as :

$$\theta = \frac{\frac{3}{32} f_w {V_m}^2}{g(S_s - 1)d_p} \tag{2.17}$$

Here f_w and S_s are the single phase flow friction factor and solids relative density, respectively. The parameter C_L is the lift coefficient and is given by:

$$C_L = C_{L0} \Lambda Sech(\frac{60d}{D})[1 - 0.02\lambda^{1.75}] \tag{2.18}$$

where λ is the linear concentration and defined as :

$$\lambda = [(\frac{C_{max}}{C_s})^{\frac{1}{3}} - 1]^{-1} \tag{2.19}$$

Here C_s is the solids volumetric concentration and C_{max} is the maximum volumetric packing fraction of solids which is a function of particle shape and size distribution

the (7).

The C_{L0} in Equation 2.18 is given by:

$$C_{L0} = 1.43(Re^*)^{0.33} \tag{2.20}$$

where Re^* is the Reynolds number based on the particle shear velocity ($u_p{}^*$). The shear velocity for a settling particle is given by (47) :

$$u_p{}^* = \sqrt{\frac{(S-1)gd_p}{6}} \tag{2.21}$$

The parameter Λ in Equation 2.18 accounts for the effect of the viscous sublayer on particles with different diameters. The value for Λ ranges from 0 to 1. For small particles that are fully enclosed in the viscous sublayer, there is no significant near-wall lift force and Λ is zero. For larger particles that are partially enclosed in the viscous sublayer, Λ is greater than zero. The details of the method for calculation of Λ are described in Wilson et al. (47) and Whitlock et al (54).

The SEC can be expressed in terms of stratification ratio by combining Equations 2.1 and 2.12 which results in:

$$SEC = \frac{R(S-1)C_s}{SC_s} + \frac{i_w}{SC_s} \tag{2.22}$$

Equations 2.16 to 2.22 can be used as a modeling framework based on the Wilson et al. model (47) to calculate SEC values for heterogeneous slurry flows at different conditions. The optimum operating condition for slurry flows can be obtained by evaluating SEC with respect to velocity and solids concentration, allowing one to determine the condition at which the SEC is a minimum.

Various pipe diameters, particle sizes, mixture velocities and solids concentrations have been tested in the analysis to study the effect of each individual parameter on SEC and on the optimum operating condition. Mixtures of particles with diameters ranging from 150 μm to 2000 μm with volumetric solids concentrations of 20%, 30% and 40% at mixture velocities up to 10 m/s in different pipe diameters (D = 0.15 and

0.4 m) were investigated. The effect of these parameters on SEC and the optimal pipeline operating condition will be discussed in the following section.

2.3.2 Results and discussion

The first important consideration in determining the optimum operating condition for a settling slurry is to ensure that the pipeline operates at velocities higher than the mixture deposition velocity (V_c). In the first step of the analysis, the minimum deposition velocity for each case was calculated using the Wilson et al. method (3).

Figures 2.12 to 2.15 show the effect of solids concentration on SEC at different mixture velocities for 150 μm and 2000 μm particles in different pipe diameters. The velocity here is expressed in terms of a non-dimensional Durand ratio:

$$Durand\ Ratio = \frac{V_m}{\sqrt{gD(S-1)}} \tag{2.23}$$

For a constant solids concentration, SEC values decrease with increasing mixture velocity and reach a minimum at a specific velocity. Further increases in mixture velocity result in an increase in the SEC. The optimum velocity (where minimum SEC occurs) is different for each specific solids concentration and increases with increasing solids concentration. The same trend was observed for all particle sizes.

An interesting observation can be made when evaluating the effect of solids concentration on SEC. The minimum SEC values decrease with increasing solids concentration from 20% to 30%, but then increase with further increases in concentration from 30% to 40%. This trend, which was the same for all particle sizes, shows that there is an optimum operating condition (at a solids concentration around 30%) which results in the lowest SEC for that slurry and a maximum transport efficiency.

The effect of particle diameter on optimum SEC at $C_s = 30\%$ in 0.15 m and 0.4 m diameter pipes is shown in Figure 2.16. The results show that SEC increases with increasing particle diameter. The rate of change in SEC is highest at smaller particle diameters where Λ increases with increasing particle diameter and the contribution of the near-wall lift force is significant. When Λ reaches it maximum value ($\Lambda = 1$),

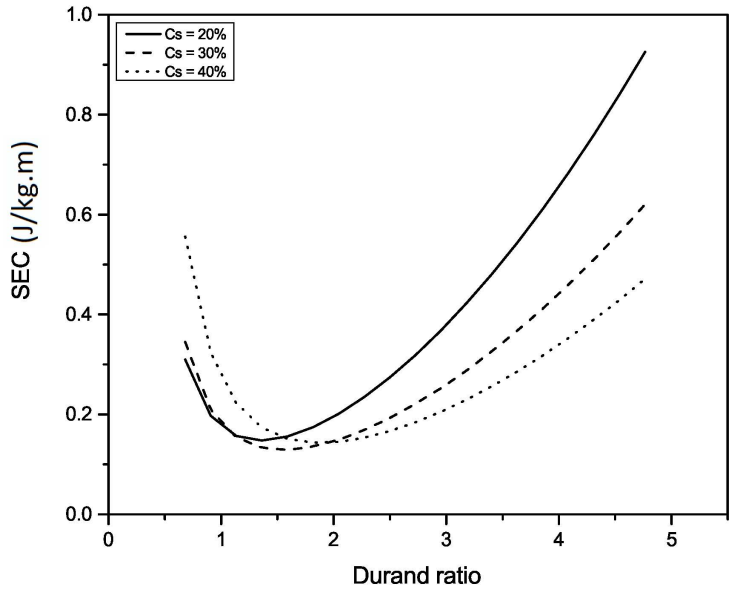

Figure 2.12: The effect of solids concentration on SEC ($d_p = 150\ \mu m$, $D = 0.15\ m$).

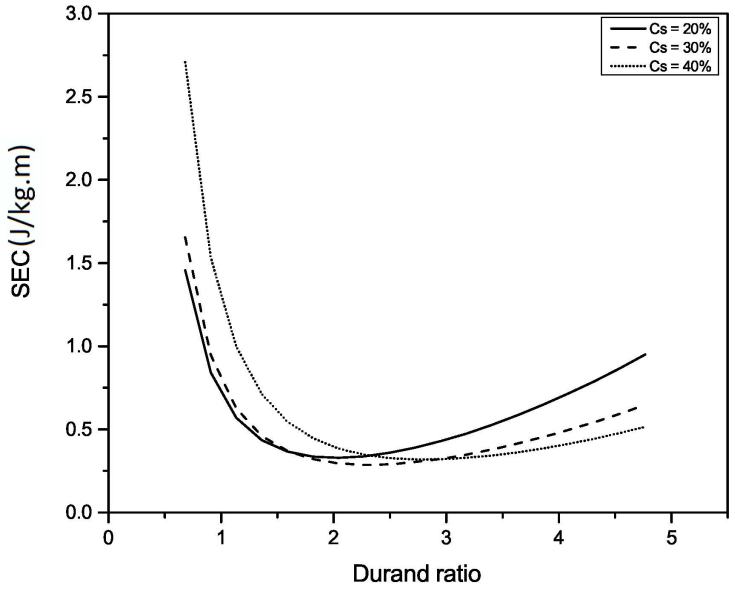

Figure 2.13: The effect of solids concentration on SEC ($d_p = 2000\ \mu m$, $D = 0.15\ m$).

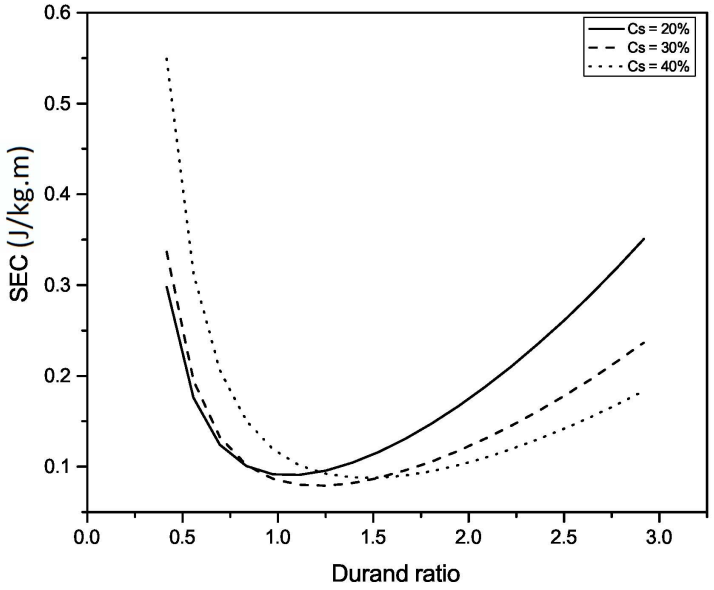

Figure 2.14: The effect of solids concentration on SEC ($d_p = 150\ \mu m$, $D = 0.4\ m$).

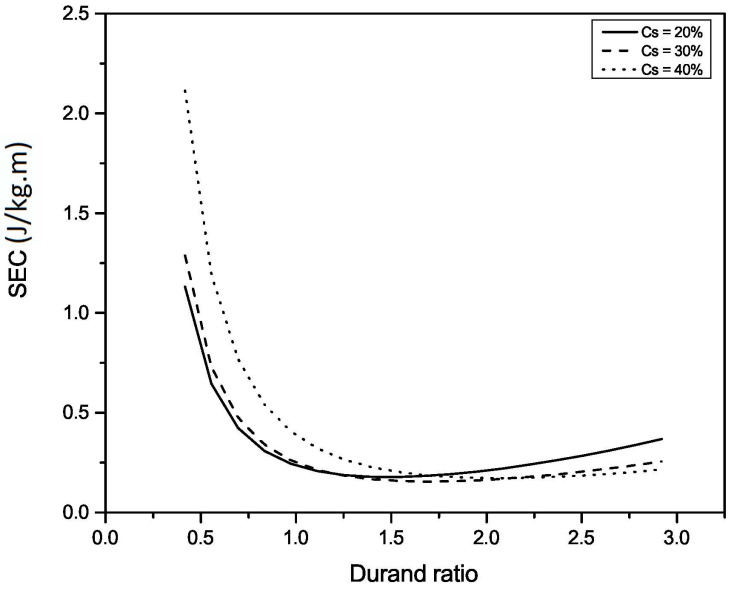

Figure 2.15: The effect of solids concentration on SEC ($d_p = 2000\ \mu m$, $D = 0.4\ m$).

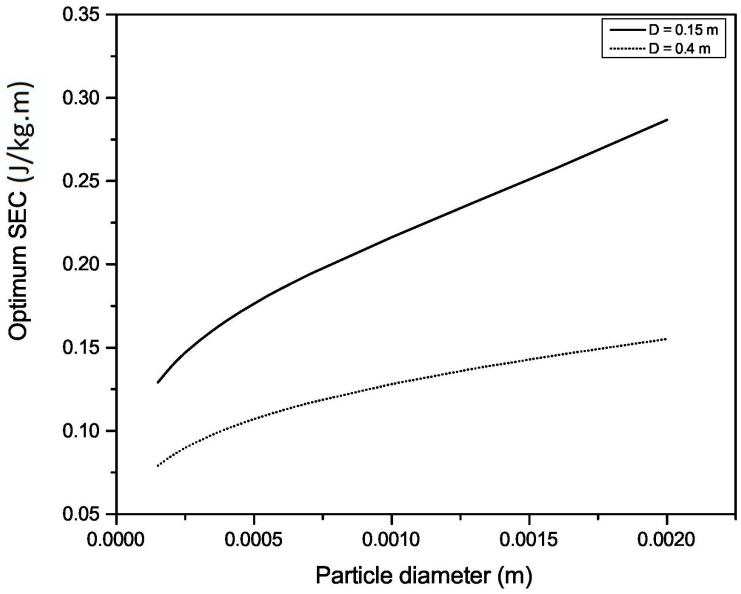

Figure 2.16: The effect of particle diameter on optimum SEC at $C_s = 30\%$.

further increases in particle diameter do not affect Λ and the slope of SEC versus particle diameter is nearly constant. Similar optimum SEC versus particle diameter behavior was found at solids concentrations of 20 and 40% by volume.

Figures 2.17 and 2.18 show the effect of mixture velocity on SEC for different particle diameters in 0.1 m and 0.4 m diameter pipes. This is an important consideration in designing heterogeneous slurry pipelines in order to minimize the energy consumption. The dotted line on these figures is the locus of minimum SEC values while the dashed-line is the locus of deposition velocities for mixtures with different particle sizes.

Two sets of data from experimental works carried out at the SRC (SRC unpublished data) and Kyushu Institute of Technology (KIT) Powder Technology Laboratory (55) were used to evaluate the performance of the model in predicting the optimum operating condition for heterogeneous slurry flows. Table 2.4 shows the details of these experiments.

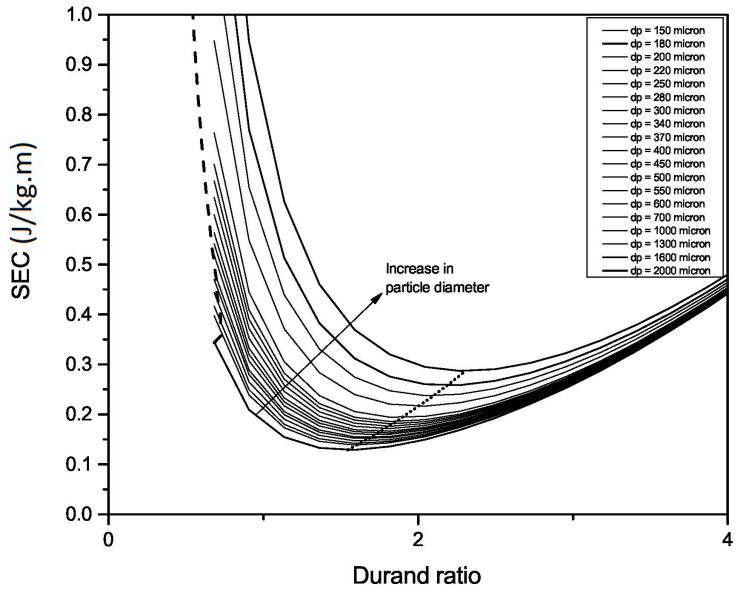

Figure 2.17: SEC versus Durand ratio for different particle diameter ($C_s = 30\%$, $D = 0.15\ m$).

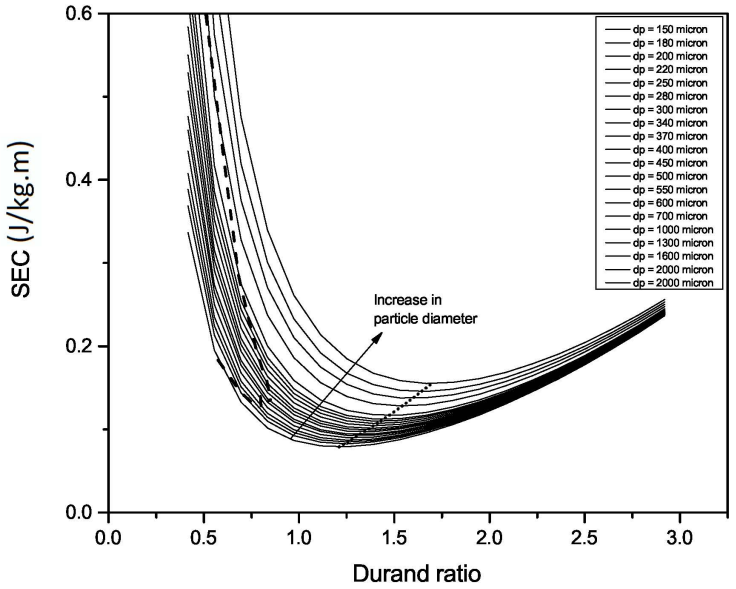

Figure 2.18: SEC versus Durand ratio for different particle diameter ($C_s = 30\%$, $D = 0.4\ m$).

Table 2.4: Details of experimental data sets.

Data set	Experiments	Solids	d_p (μm)	D (m)	V (m/s)	C_s (v/v)%	ρ_s (kg/m^3)	ρ_f (kg/m^3)
1	SRC	Bakelite	980	105	1–5	10–40	1589	999
2	KIT	Glass	440	55	2–7	10–40	2470	1000

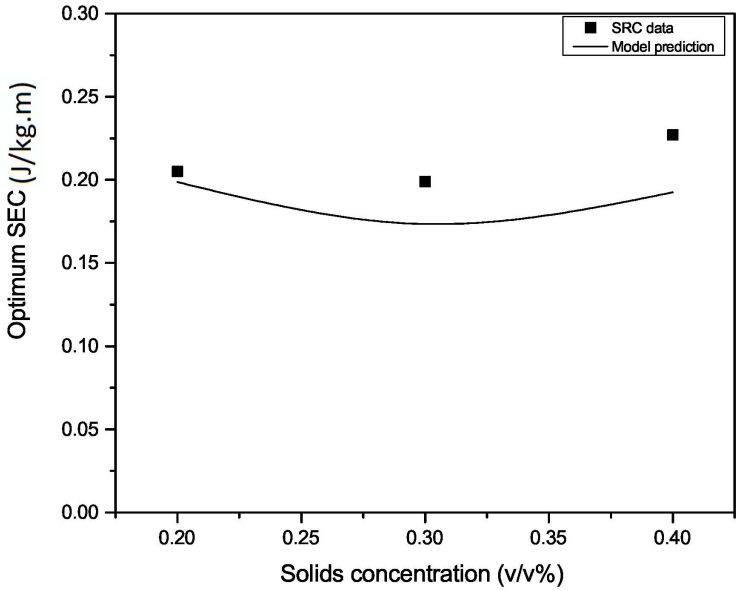

Figure 2.19: Comparison of the model prediction with SRC data for Bakelite particles ($D = 0.105\ m$, $d_p = 980$ micron).

Figures 2.19 and 2.20 show the comparison between optimum SEC obtained from both experimental data and model predictions. The comparisons show good agreement with the experimental data. Although the model slightly underestimates the optimum SEC value, it captures the optimum SEC versus solids concentration trend.

2.4 Summary

Two different models were used to determine the SEC for fine and coarse particle slurries. For Newtonian, fine-particle slurries (where $d_{50} < 100\ \mu m$), the equivalent-

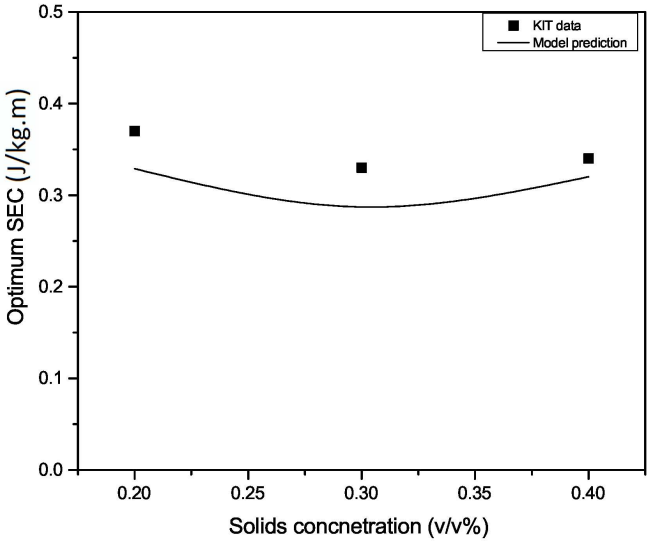

Figure 2.20: Comparison of the model prediction with KIT data for glass beads ($D = 0.55\ m$, $d_p = 440\ m$).

fluid model provides reasonable friction loss predictions for solids concentrations less than 30%. For slurries of this type, the minimum SEC occurs at a solids volume fraction between 0.3 and 0.4. The exact value will depend on the particle size distribution and particle shape, through their effect on the slurry's maximum settled bed concentration, C_{max}. Provided the equivalent-fluid model provides a reasonable approximation of the friction losses, one can show that SEC continues to increase with increasing mixture velocity and/or decreasing pipe diameter. In other words, for slurries of this type, the designer would select pipe diameter and mixture velocity based on solids throughput, a slurry density that optimizes SEC and a velocity based on the slurry's deposition velocity times a safety factor of, say, 1.15.

For coarse-particle slurries, the near-wall lift model is used to calculate the SEC and optimum operating conditions for horizontal pipe flow of heterogeneous slurry flows with particle sizes greater than 150 μm. The effect of different parameters such as particle size, pipe diameter, mixture velocity and solids concentration on the operation of horizontal slurry pipeline flows was evaluated. The analysis shows

that at solids concentrations around 30% by volume, a minimum SEC is achieved for a specific particle size and pipe diameter. This optimum SEC value increases with increasing particle diameter. The agreement between model predictions and experimental data verifies the use of the model developed in this study.

3

Solids velocity and concentration fluctuations in highly concentrated liquid-solids (slurry) pipe flows

Material in this chapter has been submitted to: *Hashemi, S.A., Shah, I.M.A., Sadighian, A., Sanders, R.S., (2013). " Solids velocity and concentration fluctuations in concentrated solid-liquid pipe flows. Int. J. Multiphase Flow.*

3.1 Introduction

Pipeline flows of coarse-particle slurries are of great importance in many industries, including hard-rock mining, oil sands production, and nuclear waste treatment. Industrial slurries have different particle sizes and hence the relative positions and velocities of these particles play an important role in pipeline design and operation. An improved understanding of the complex behavior of these flows and the physics behind them will help to improve models needed to predict, for example, frictional pressure losses, optimal operating velocities, and pipeline wear.

Highly concentrated two-phase flows are generally unsteady and previous experiments have shown that velocities and concentrations of both phases undergo fluctuations about their mean values (44). Parameters such as collisional particle pressure or granular temperature are used to describe the solids fluctuations. Presently, differ-

ent models describing particle interactions, e.g. kinetic theory (21), are commonly found in commercial CFD (Computational Fluid Dynamics) packages. However, these models have not been widely compared with experimental results, especially for liquid-solid flows. The Zenit et al.(19) experimental study of collisional pressure in a liquid-solid fluidized bed showed the unsatisfactory performance of current models, which is mainly a consequence of the lack of understanding of the physics and mechanisms that govern the behavior of these complex systems.

One of the barriers to improved understanding and model development is the difficulty associated with making the appropriate measurements (56), particularly for highly concentrated coarse-particle slurries where the axial velocities are high and mixtures are opaque.

One of the most thorough studies of solids fluctuations in concentrated liquid-solid flow is the experimental investigation of Zenit and Hunt (44). They measured the cross-sectional averaged solids concentration fluctuations in a fluidized bed and for gravity driven flow, for large particles with different diameters and densities. They compared their results with the Buyevich and Kapbasov (57) model. In this model, the solids concentration fluctuations are a function of bulk solids concentration only. Zenit and Hunt(44) found that the averaged solids concentration fluctuations are a function of both solids concentration and Stokes number, with the magnitude of the fluctuations increasing with increasing Stokes number. This was in accord with their previous findings; that is, high frequency fluctuations are mainly due to direct collisions and the power of an immersed collision increased as the Stokes number increased (58). They concluded that the Buyevich and Kapbasov (57) model relates to the condition where Stokes number tends to infinity.

Picciotto et al. (59) studied the interactions between a dispersed solids and fluid turbulence in a turbulent channel flow. They noted that interaction between particles and coherent turbulent structures near the wall results in streamwise velocity fluctuations in solids velocity. Their results show that solids streamwise velocity fluctuations are higher near the wall and decrease with increasing distance from the wall.

They also show that the magnitude of these fluctuations increases with increasing particle Stokes number.

Kechroud et al. (60) studied the dynamic behavior of the continuous phase in a solid-liquid fluidized bed. They compared their measurements of liquid velocity fluctuations with solids concentration fluctuations from Didwania and Homsy (61) and Zenit and Hunt (44). They found a high degree of similarity between liquid velocity fluctuations and solids concentration fluctuations.

Varaksin and Polyakov (62) studied particle velocity fluctuations in an air-solid turbulent pipe flow. They classified the mechanisms for solids velocity fluctuations into four main categories: (1) solid-fluid turbulence interaction, (2) presence of particles with different sizes, i.e. not truly monosized particles, (3) particle-particle and particle-wall collisions and (4) migration of particles to regions with different velocities (streaming mechanism). These four phenomena could also be considered as the main mechanisms producing solids concentration fluctuations.

One of the difficulties associated with experiments involving concentrated multiphase flows is the lack of viable measurement techniques. Common single phase and dilute multiphase flow measuring techniques, such as LDV (Laser Doppler Velocimetry), PIV (Particle Image Velocimetry), and PTV (Particle Tracking Velocimetry) are widely used for transparent flows where the solid concentration is low. However, their capabilities in highly concentrated and opaque flows, such as dense slurry flows, are debatable (32).

Advances in measurement techniques in recent years, especially electrical tomography methods, have opened a new window in the experimental study of multiphase flows. The most important advantage of these methods is their ability to perform measurements in concentrated and opaque systems. It also appears that these methods are sufficiently fast and robust enough for slurry flow applications (32; 36; 37). Numerous studies have been conducted where electrical tomography techniques are used on fluid-particle systems, such as pneumatic conveying of granular solids (38; 39), flow distribution and velocity measurement in a fixed bed reactor

(40), hydraulic conveying of materials (41), and fluidization (42). However, only a very limited number of studies directly related to electrical tomography and slurry pipe flow measurements have been published (36; 63; 64). Applications of electrical tomography to slurry pipeline flow measurements have thus far been restricted to time- and spatial- averaged values of concentration.

The goal of this paper is to investigate the mechanisms that are responsible for the production of high frequency-low amplitude solid concentration and velocity fluctuations in highly concentrated slurry flows. Novel high-frequency Electrical Impedance Tomography (EIT) measurements for highly concentrated pipeline flows of solid-liquid mixtures are used to evaluate the validity and limitations of the analysis. Specifically, solid turbulent intensity and concentration fluctuation and time-averaged solid concentration profiles for slurry flow in a horizontal pipe were measured using Electrical Impedance Tomography. The results were also compared to the models available in the literature to evaluate their capabilities and limitations. Measurements of this type are needed to develop and/or validate numerical simulations of slurry flows.

3.2 Experimental details and analysis

3.2.1 Experiments

A 52 mm (i.d.) horizontal pipeline loop located at the Saskatchewan Research Council (SRC) Pipe Flow Technology Centre, SK, Canada, was used to perform the experiments. The schematic layout of the loop is shown in Figure 3.1. The loop includes a centrifugal pump to circulate the slurry within the loop at different velocities. Operating volumetric flow rates were measured using a Foxboro 2802-SABA-TS magnetic flow meter. Two heat exchangers were used to keep the operating temperature constant during experiments. Slurries of known concentration were prepared using tap water as the carrier fluid and particles were introduced to the loop from the feed tank. Pressure drop along a test section was measured using a Valydyne DP15 dif-

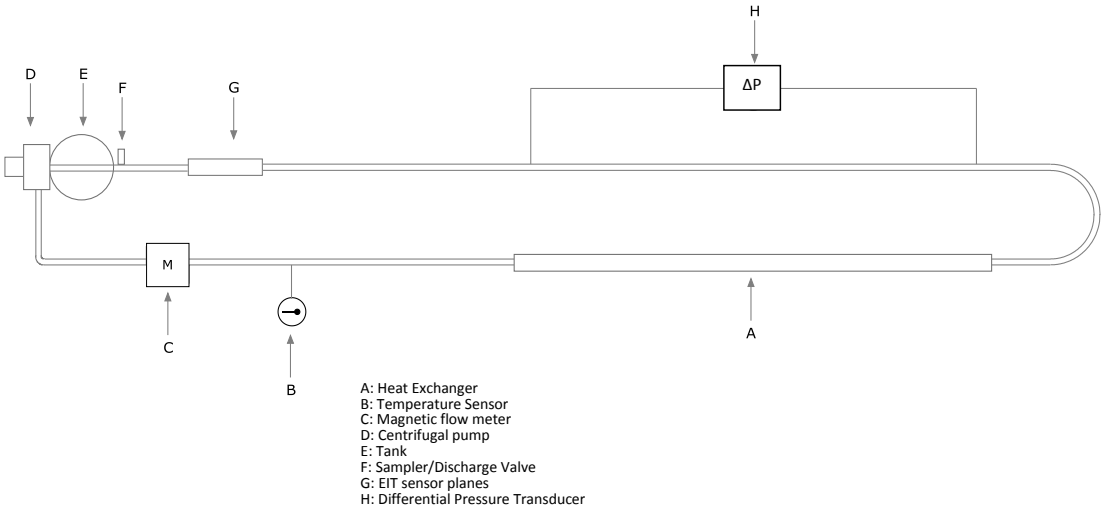

Figure 3.1: Schematic of 52 mm horizontal pipe-loop

ferential pressure transducer. The transparent observation section was used to ensure that air, which sometimes enters the line during the preparation of the slurries, was completely removed before measurements were taken. Additional details regarding the pipe loop and its operation can be found in Appendix A. Sand (Lane Mountain LM125) with $d_{50} = 100\ \mu m$ was used in the experiments. The particle size distribution of the sand is shown in Figure 3.2. Experiments were performed at solids volumetric concentrations of 20–35% and mixture velocities of 2–5 m/s.

An Industrial Tomography Systems (ITS) Z8000 Electrical Impedance Tomography (EIT) data acquisition system along with a dual-plane sensor was employed to measure solids velocity and concentration distributions. Each sensor plane consists of 16 electrodes which are arranged at equal spacing around the boundary of circular pipe. The frequency of AC injecting current was set to 80 kHz. Data were collected at a frequency of 820 frames per second (fps) per plane. The instrument measures the resistivity distribution map within the sensor plane. The resistivity map is then converted to solids concentration using the Maxwell equation (36):

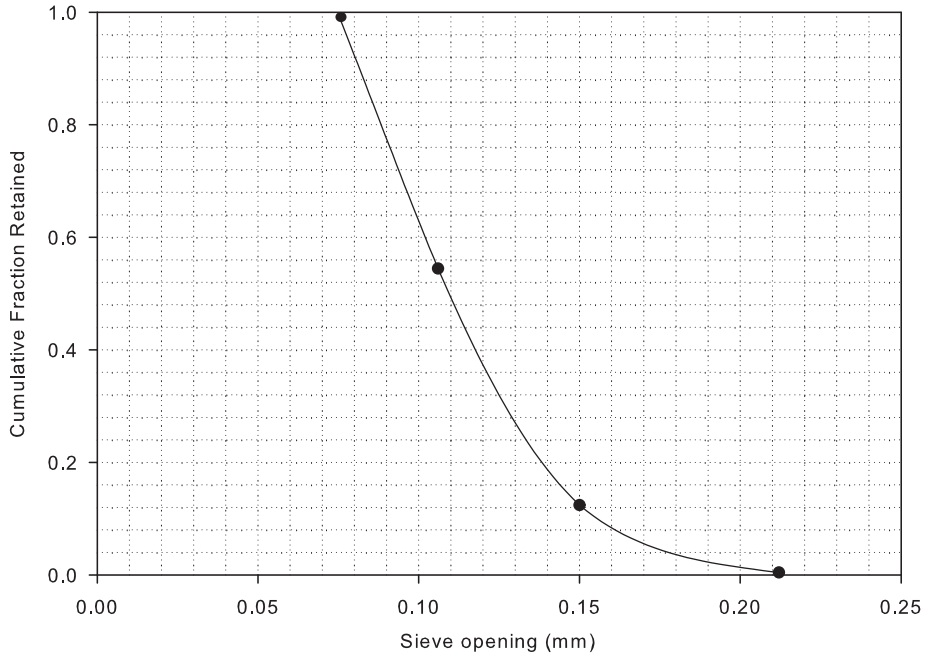

Figure 3.2: Particle size distribution of sand particles used for experiments

$$C_s = \frac{2\sigma_1 + \sigma_2 - 2\sigma_m - \frac{\sigma_m \sigma_2}{\sigma_1}}{\sigma_m - \frac{\sigma_2}{\sigma_1}\sigma_m + 2(\sigma_1 - \sigma_2)} \tag{3.1}$$

where σ_1, σ_1 and σ_m are the conductivity of continuous phase, the conductivity of dispersed phase and the reconstructed measured conductivity, respectively; while the C_s is the dispersed phase volume fraction.

Figure 3.3 shows the EIT reconstruction grid. The map divides the pipe cross section into 316 pixels of equal area. The solids concentration within each pixel is measured. Pixel to pixel cross-correlation of concentration maps between two planes was used to obtain the solids velocity distribution map (65).

For each set of experiments, 8000 conductivity maps were collected from each sensor plane for every test, i.e. at different mixture flow rates and sand concentrations. The resulting concentration maps were used to calculate solids phase concentration fluctuations, velocities and turbulent intensities.

Before any slurry tests were conducted, EIT measurements were collected for single phase (water only) runs. Solids phase concentration fluctuations should of course be zero in single phase flow. Any nonzero values represent measurement noise. Comparison of actual solids-phase concentration fluctuation measurements with the baseline measurements (noise) made for water flow illustrates the ability of the instrument to provide meaningful data. Note that other baseline/validation measurements are provided in Appendix C. Figure 3.4 shows concentration fluctuation profiles measured for flow of sand slurry with C_s= 25% at mixture velocities of 2 and 5 m/s. The measurement noise for single phase water flow at the same velocities is also shown in these figures. Note that y is the distance from the bottom of the pipe, and that this terminology is used for all figures in this chapter where measurements made at numerous positions over the flow domain are reported. The results clearly show the effect of the dispersed solids phase on both the magnitude and the shape of the concentration fluctuation profiles. To obtain more accurate concentration fluctuation values, the noise effects were removed from the concentration fluctuation signals by decomposition of signal variance. The same procedure was followed for all other velocities and concentrations reported here.

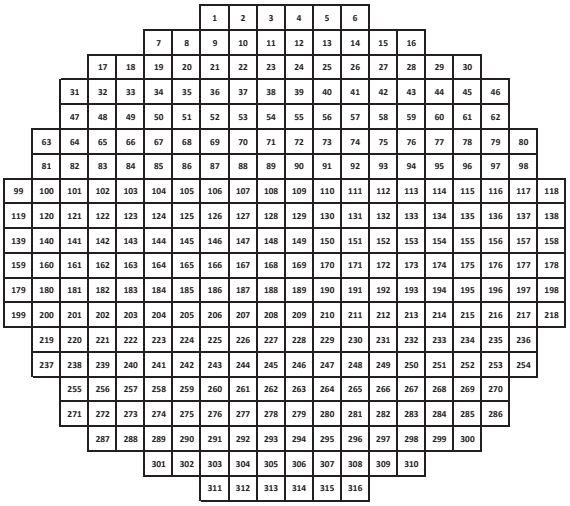

Figure 3.3: Schematic diagram of EIT reconstruction grid

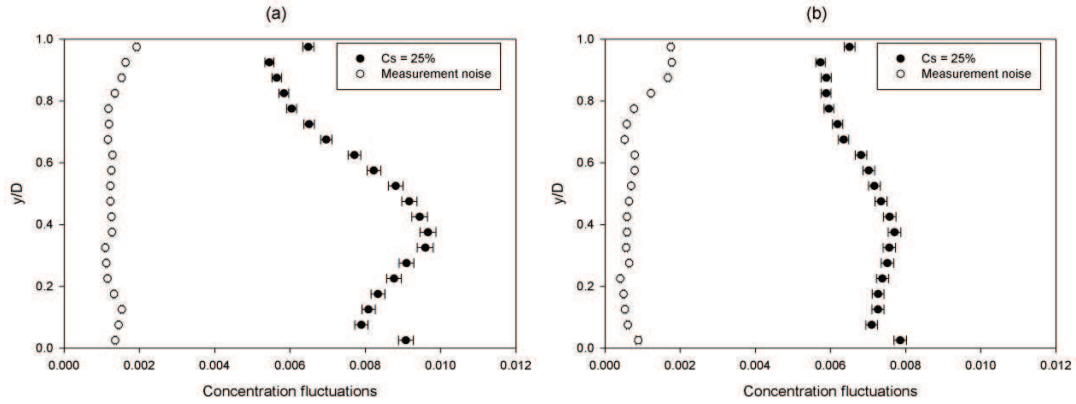

Figure 3.4: Comparison between raw concentration fluctuations (including noise) for 100 micron sand flowing in a 52 mm pipeline loop at $C_s = 25\%$ and measurement noise for single phase water flow: (a) V = 2 m/s; (b) V =5 m/s.

3.2.2 Analysis

If S_{p1} and S_{p2} are signals obtained from planes 1 and 2, respectively, at time t, the cross correlation function is defined as:

$$R(\tau) = \lim_{T\to\infty} \frac{1}{T} \int_0^T S_{p1}(t) S_{p2}(t+\tau) dt \tag{3.2}$$

where τ is the time delay between S_{p1} and S_{p2} and T is the observation time. The time delay at the maximum value of R value corresponds to the transit time between planes 1 and 2. Since the separation distance between the two planes, L_s, is known, the transit velocity can be obtained using:

$$u = \frac{L_s}{\tau_{\max}} \tag{3.3}$$

where $\tau_{\max}$ is the time delay at the maximum value of the cross-correlation coefficient, $R_{\max}$.

Pixel-to-pixel cross correlation can be used to determine the local solids velocity between corresponding pixels in the two planes. If we assume that C_{p1m} and C_{p2m}

are concentration signals obtained for pixel m, in planes 1 and 2, the cross-correlation coefficient is obtained by:

$$R(\tau) = \sum_{k=0}^{N-1} C_{p1m}[k] C_{p2m}[k+\tau] \tag{3.4}$$

where τ is the time delay, k is the image number and N is the number of images. The time delay at maximum R, $\tau_{\max}$, can be used to obtain the local solids velocity in each pixel.

Instantaneous solids velocities can be obtained by using shorter time windows, i.e. shorter T values. The windows were used to select shorter time sequences and the cross-correlation between these sections used to determine the solids-phase instantaneous velocity in each pixel. The time resolution of instantaneous velocities was set to be $0.01s$. The instantaneous velocities were then used to calculate RMS solids velocity fluctuations and solids turbulent intensities. The RMS velocity concentration fluctuation was calculated from:

$$\acute{V}_s = \sqrt{\frac{1}{N}\sum_{i=1}^{N}(\bar{V}_s - V_{si})^2} \tag{3.5}$$

where N, $\acute{V}_s$,$\bar{V}_s$ and V_{si} are the number of measurements, RMS solids velocity fluctuation, average solids velocity and instantaneous solids velocity, respectively. The time-averaged solids velocity was calculated by cross correlation of the entire signal using Equation 3.3. Solids turbulent intensity was also calculated by dividing the RMS solids velocity fluctuation by the time-averaged solids velocity. The RMS solids concentration fluctuation was also computed from:

$$\acute{C}_s = \sqrt{\frac{1}{N}\sum_{i=1}^{N}(\bar{C}_s - C_{si})^2} \tag{3.6}$$

where N, $\acute{C}_s$,$\bar{C}_s$ and C_{si} are the number of measurements, RMS solids concentration fluctuations, average solids concentration and instantaneous solids concentration, respectively. The average solids concentration was also calculated using:

$$\bar{C}_s = \frac{1}{N}\sum_{i=1}^{N} C_{si} \tag{3.7}$$

The Confidence Interval for measurements was estimated as (66):

$$C.I. = \pm 1.96 \times SE \tag{3.8}$$

where SE is the Standard Error and is defined as:

$$SE = \frac{S}{\sqrt{N}} \tag{3.9}$$

Here, S and N are standard deviation and number of measurements, respectively.

All measurements were made at operating velocities that exceeded the predicted deposition velocity for each condition. Deposition velocity is the velocity at which a stationary deposit occurs. The stationary bed decreases the cross sectional area available for flow and normally has higher surface roughness compared to the pipe wall (7). As a result, frictional pressure loss is considerably higher at velocities less than the deposition velocity. Table 3.1 shows predicted values of the deposition velocity for the 100 micron sand slurries at different concentrations using existing correlations (2). When the particle size is smaller than the thickness of the viscous sublayer, the deposition velocity increases with increasing solids concentration. For these particles, two main vertical forces act on the particles: the gravity force, which acts downward, and a net upward force which is the combination of particle-particle collisions and lift forces (67). Sanders et al. (67) showed that this net upward force is directly proportional to $(C_{max} - C_s)$ and decreases with increase in solids concentration. As a result, the minimum velocity required to avoid the formation of a stationary bed (deposition velocity) increases with increasing solids concentration. The 100 micron sand particles used in this study belong to this category. The highest deposition velocity, $V_c = 1.06\ m/s$, is obtained at $C_s = 0.35$. The minimum velocity at which experiments were performed was 2 m/s to ensure that the formation of a stationary deposit was avoided. Additionally, the averaged solids concentration and

Table 3.1: Calculated deposition velocities for 100 micron sand-in-water mixtures in a 52 mm pipe.

Solids concentration, C_s	Deposition velocity (m/s)
20%	0.82
25%	0.88
30%	0.96
35%	1.06

frictional pressure gradient were monitored to ensure that they were constant during the period of time that EIT data were collected.

As the main focus of this work is to study the low amplitude-high frequency fluctuations, the high amplitude-low frequency fluctuations were filtered using a 4^{th} order, high pass Butterworth digital filter algorithm. A cut-off frequency of 3 Hz was chosen by examining the frequency domain signals, which is the same as that chosen by Zenit and Hunt (44). Figure 3.5 shows the concentration fluctuation signals before and after the digital filter was applied. The magnitude of RMS solids concentration fluctuation decreased slightly in all cases after filtering due to the removal of higher amplitude- lower frequency phenomena. Longer measurement times are required to accurately capture the low frequency fluctuations that are mainly due to the bulk motion of the flow (44).

The power spectral density of the solids concentration and velocity fluctuation signals was also obtained so that energy distribution at different frequencies could be studied. The Welch method, which is a technique for estimating averaged power spectra with data windowing (68), was used to estimate power spectra. In the Welch method, the original signal is divided into a number of sections each of length L and the averaged power spectrum is calculated using:

$$\bar{I}(f) = \frac{1}{K} \sum_{r=0}^{K-1} I_r(f) \tag{3.10}$$

where K is the number of sections and $I_r(f)$ is the power spectrum estimation for

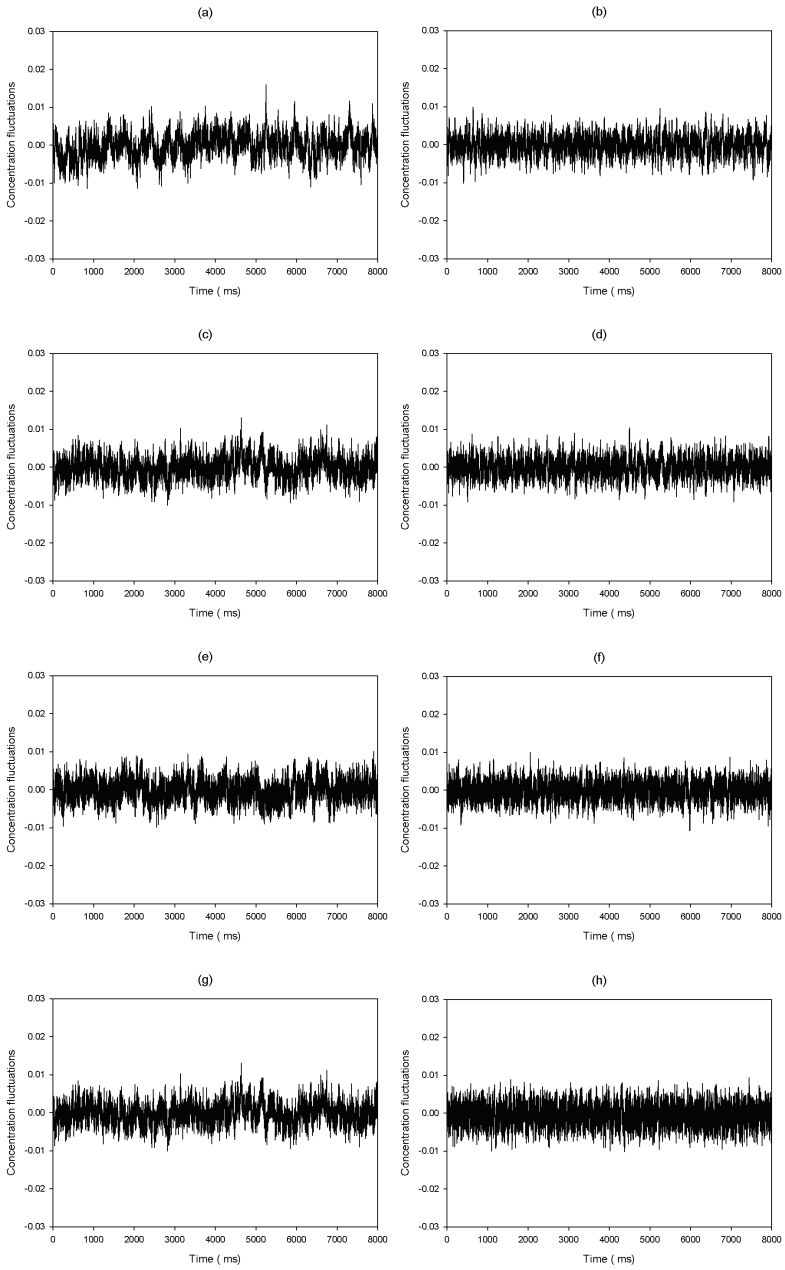

Figure 3.5: Solids concentration fluctuation before (a, c, e, g) and after (b, d, f, h) applying digital filter for 100 micron sand flowing in a 52 mm pipeline loop at $C_s = 20\%$: (a) and (b) V = 2 m/s; (c) and (d) V = 3 m/s; (e) and (f) V = 4 m/s; (g) and (h) V = 5 m/s.

each section. In the current study, the original signal is segmented into eight sections ($K = 8$) with 50% overlap, to minimize the spectral variance and obtain the optimum results. The segmented signals along with Hamming windows of the same length as the segment (69) were used to estimate the average power spectra.

3.3 Results and discussion

3.3.1 Solids velocity and turbulent intensity

The main mechanisms producing velocity fluctuations in the centre of the flow are particle-particle interactions and solids-fluid turbulent interactions (62). Here, we analyze the turbulent intensity profiles and power spectra of solids velocity fluctuations to determine the relative importance of the two mechanisms.

Solids axial turbulent intensity profiles are provided in Figure 3.6. The experimental results show that the solids turbulent intensities are higher near the wall, i.e. wall peaked. A similar trend was observed by Kulick et al. (70) for 50 and 90 micron glass beads and 70 micron copper particles in a wind tunnel. Alajbegovic et al. (71) observed wall-peaked solids axial turbulent intensities for the upward flow of ceramic particles in a vertical pipe. The main reason for the higher solids turbulent intensities near the wall is the particle-wall interactions that occur in that region. Another important mechanism is the off-the-wall migration of particles to regions with higher velocities (12; 47). The results presented in Figure 3.6 also illustrate that the magnitude of the solids turbulent intensities are roughly uniform at the pipe center, particularly at mixture velocities of $3m/s$ or greater. Figure 3.7 shows sample turbulent intensity maps obtained from tomography measurements.

The presence of the dispersed solids affects the fluid turbulent structure (72; 73) and is generally referred to as turbulence modulation. The study of turbulence modulation in both experimental and theoretical frameworks is presently an active area of research. The ideal situation is to study the fluid-particle interactions by measuring solids and fluid velocity fluctuations simultaneously. Unfortunately, the measure-

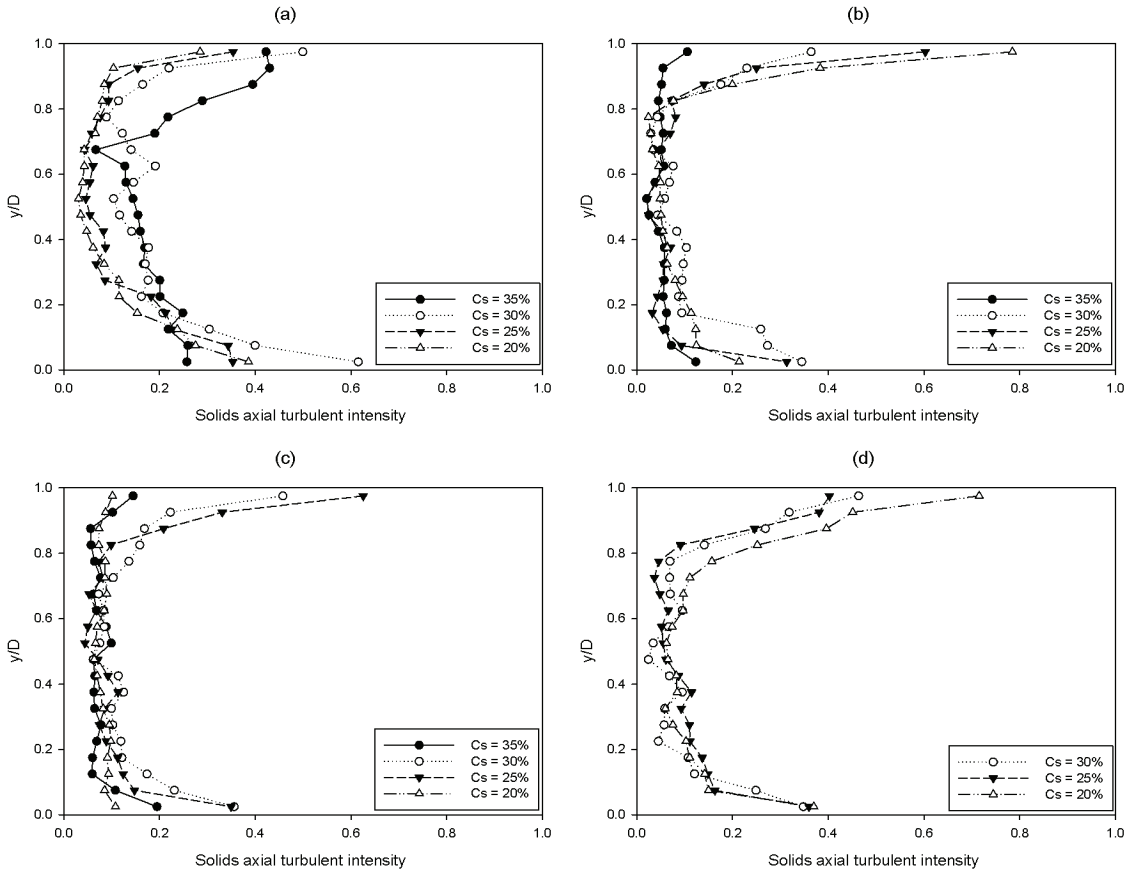

Figure 3.6: Solids turbulent intensity profiles for 100 micron sand flowing in a 52 mm pipeline loop at different solids concentrations: (a)V = 2 m/s; (b) V = 3 m/s; (c) V = 4 m/s; (d) V = 5 m/s.

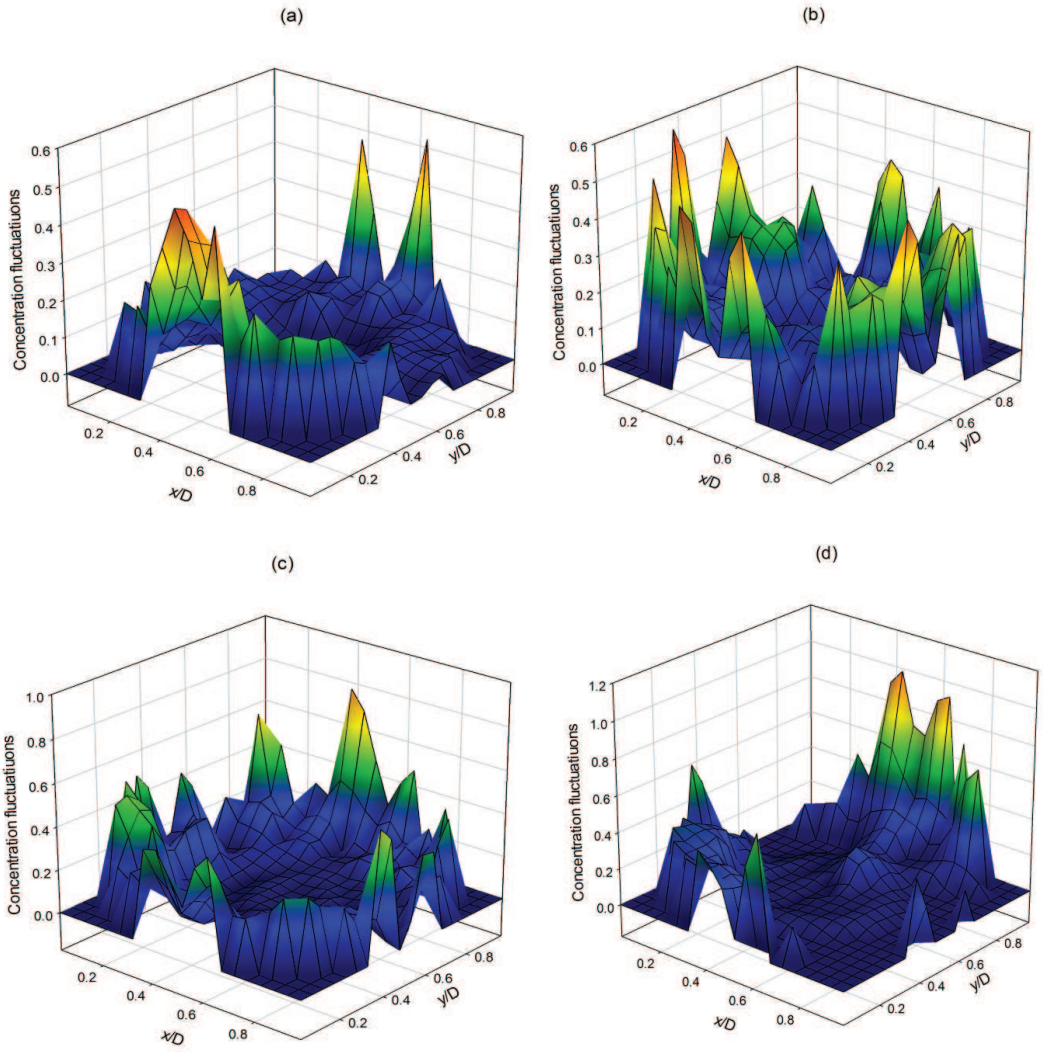

Figure 3.7: Time-averaged solids turbulent intensity maps for 100 micron sand flowing in a 52 mm pipeline loop at different solids concentrations and mixture velocities: (a)V = 2 m/s and C_s = 20%; (b) V = 3 m/s and C_s = 35%; (c) V = 4 m/s and C_s = 30%; (d) V = 5 m/s and C_s = 25%.

ment techniques for measuring fluid velocity fluctuations are only applicable to very low solids concentrations and are not suitable for concentrated mixtures of the type studied here. The studies and models of turbulence modulation found in the literature are limited to very low solids concentrations and are far from being applicable to concentrated systems such as the system of interest in this study. Another approach that has been used in the past to account for the presence of the particles is to use a mixture viscosity model, such as that proposed by Thomas (74), to account for the effect of fluid-particle interactions. Although the application of mixture viscosity models might be reasonable for homogenous mixtures of spherical particles at low solids concentrations, their ability to accurately describe fluid-particle interactions or any other flow characteristics deteriorates badly as the solids concentration and particle size and/or angularity increase (45). Hence, mixture viscosity models are not applicable to the slurries of interest here, where solids concentrations are high and particles are angular.

In the present study, we choose to compare qualitatively the dispersed solids phase velocity fluctuation measurements with single-phase flow fluid turbulence characteristics. The motivation for this choice can be stated as:

- Relatively simple approaches, such as mixture viscosity models, do not properly or accurately describe energy dissipation mechanisms for concentrated slurry flows of the type studied here;
- Models describing single-phase fluid turbulence characteristics are well known and accepted;
- Measurements of time-averaged solids concentration profiles in dense slurry pipeline flows were accurately predicted using a solids-phase turbulent diffusion coefficient equivalent to the eddy kinematic viscosity calculated for turbulent, single-phase flow (10);
- Models describing the effect of the dispersed solids phase on fluid turbulence

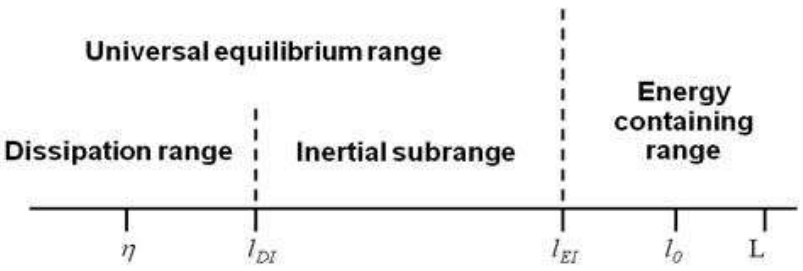

Figure 3.8: Turbulent length scales and mains ranges of turbulent energy spectrum.

have been developed (and validated) for very dilute flows only and thus are unlikely to accurately describe the modulating effects that occur at high solids concentrations.

As a consequence, it seemed logical to ignore the effect that the particles may have on the fluid turbulence and compare instead the well-known single-phase fluid turbulence characteristics with our solids-phase fluctuating measurements. The result is a clearly qualitative analysis, but one that is unfettered by questions that would naturally arise if, for example, turbulence modulation models meant for dilute mixtures were applied here. Additionally, when the comparisons with single-phase flow are taken in concert with the results obtained by other researchers (e.g. Zenit and Hunt (44)), a clear picture of the relative importance of fluid-particle interactions (over particle-particle collisions) in the production of solids fluctuations emerges.

The energy spectrum of single-phase turbulent motion can be divided into 3 main ranges: (1) energy containing range, (2) inertial sub-range and (3) dissipation range. Figure 3.8 shows these three ranges and the relevant length scale associated with each (75).

The energy containing range includes large scale turbulent eddies whose motion is roughly independent of viscosity. These large-scale structures contain the bulk of the turbulent energy. In the inertial sub-range, the turbulent energy transfer from larger length scales to smaller length scales occurs through a cascading process. The turbulent energy dissipates in the dissipation range due to the viscosity of the fluid.

Table 3.2: Kolmogorov length scale for the flow of water in a 52 mm pipe at different velocities

Velocity (m/s)	η (μm)	l_{DI} (μm)
2	28	1690
3	21	1271
4	17	1038
5	15	887

The dissipation range includes lengths larger than the Kolmogorov length scale and smaller than l_{DI}. The Kolmogorov length scale (η) is defined as:

$$\eta = (\frac{\nu^3}{\varepsilon})^{\frac{1}{4}} \tag{3.11}$$

where ν and ε, respectively, are the kinematic viscosity of the fluid and the rate of energy dissipation. The Kolmogorov length scale is the smallest turbulence length scale. For many turbulent flows, $l_{DI} \approx 60\eta$ (75).

To analyze the power spectrum of solids velocity fluctuations, turbulence length scales for single phase flow of the carrier fluid with the same velocity as the mixture were calculated. Table 3.2 shows the calculated Kolmogorov length scales and l_{DI} for single phase flow of water in a 52 mm pipe. The rate of energy dissipation was estimated using (76):

$$\varepsilon = \frac{4u^{*2}V}{D} \tag{3.12}$$

where u^*, V and D are the shear velocity, mixture velocity and pipe diameter, respectively. Shear velocity is defined as:

$$u^* = V\sqrt{\frac{f_w}{8}} \tag{3.13}$$

where f_w is the Moody friction factor at the mixture velocity. Any turbulent length scale that falls between η and l_{DI} is in the dissipation range.

A model for energy-spectrum function is given as (75):

$$E(\kappa) = C\varepsilon^{2/3}\kappa^{-5/3} f_L(\kappa L) f_\eta(\kappa\eta) \tag{3.14}$$

where κ is the wave number and defined as:

$$\kappa = \frac{2\pi}{l} \tag{3.15}$$

Here, l is the characteristic length scale. In Equation 3.14, f_L and f_η are non-dimensional functions which determine the shape of spectrum in the energy-containing and dissipation ranges, respectively. The dissipation function f_η is usually expressed as an exponential function (75):

$$f_\eta(\kappa\eta) = \exp(-\beta_0\kappa\eta) \tag{3.16}$$

where $\beta_0 = 2.094$. An alternative model for f_η is the Pao spectrum

$$f_\eta(\kappa\eta) = \exp(-\frac{3}{2}C(\kappa\eta)^{\frac{4}{3}}) \tag{3.17}$$

where C is constant and is equal to 1.5 (75).

Based on the calculated values of η and l_{DI} shown in Table 3.2, it can be concluded that the particles used in this study ($d = 100\mu m$) interact with turbulent eddies in the dissipation range, since particles typically interact with turbulent eddies whose length scales are of the same order of magnitude as the particle diameter. Table 3.2 shows that fluid turbulent eddies with average length scale of $100\mu m$ are in the dissipation range for the velocities and pipe diameter used in this study. As a result, the rate of energy decay for these eddies is greater than $-5/3$, which is the rate of energy dissipation for the inertial sub-range.

Figure 3.9 shows the power spectrum of solids velocity fluctuations for different velocities at a solids volume concentration of 30%. Note that all the graphs represent the rate of energy decay of solids velocity fluctuations for $100\mu m$ particles. These graphs are different from the single phase turbulent energy spectrum in the sense that the single phase turbulent energy spectrum represents the average rate of

Table 3.3: Calculated average power spectrum slope for 100 micron sand-in-water mixtures in a 52 mm pipe at $C_s = 30\%$.

Mixture velocity (m/s)	Power spectrum slope
2	-2.2
3	-2.4
4	-1.9
5	-1.8

energy decay at different turbulent length scales while Figure 3.9 represents the rate of energy decay for particles of a specific size (length scale). The averaged slopes of the power spectra of Figure 3.9 are shown in Table 3.3. The calculation of a single value to represent the slope of fluid turbulent energy decay in the dissipation range for comparison with the experimental values reported here is not practical, simply because the particles are not interacting with a specific turbulent length scale; rather a range of length scales are involved. Since the rate of energy decay in this region is sensitive to turbulent length scale, increasing with decreasing l, it is not possible to calculate a single slope which represents the turbulent energy decay rate. The only valid statement is that the rate of turbulent energy decay should be higher than the value for the inertial sub-range region. Table 3.3 shows that the experimental slope values are greater than $-5/3$ which is the energy spectrum slope for the inertial sub-range and is in accordance with the dissipation range where the slope is greater than for the inertial sub-range. The calculated slopes decrease with increasing mixture velocity which is also in accordance with the single-phase turbulent energy decay law. The results indicate that solids-turbulent interactions are primarily responsible for the production of solids velocity fluctuations, particularly in the central core of the flow. Similar trends were observed for other mixture velocities and solids concentrations. Experimental values of fluid velocity fluctuations in highly concentrated mixtures are required for further validation as the effect of solids particles on fluid turbulent is neglected in this analysis.

Figure 3.10 shows solids velocity profiles at different mixture velocities and aver-

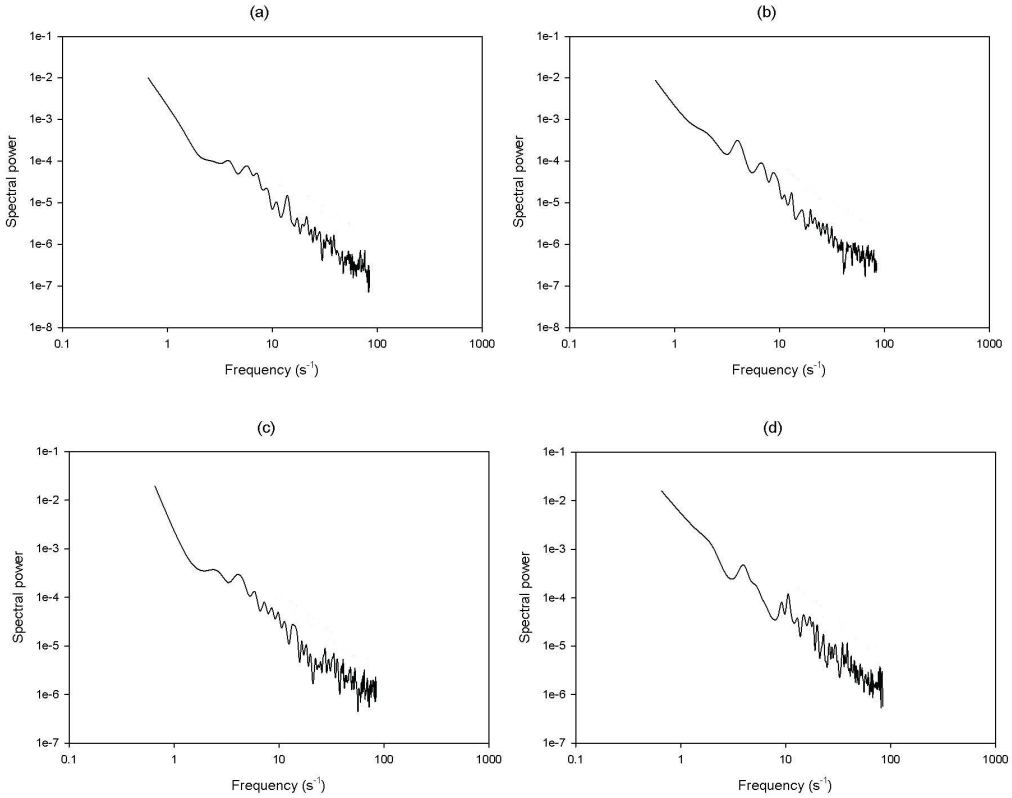

Figure 3.9: Power spectra for cross sectional averaged solids velocity fluctuations of 100 micron sand flowing in a 52 mm pipeline loop at $C_s = 30\%$: (a) V = 2 m/s; (b) V = 3 m/s; (c) V = 4 m/s; (d) V = 5 m/s.

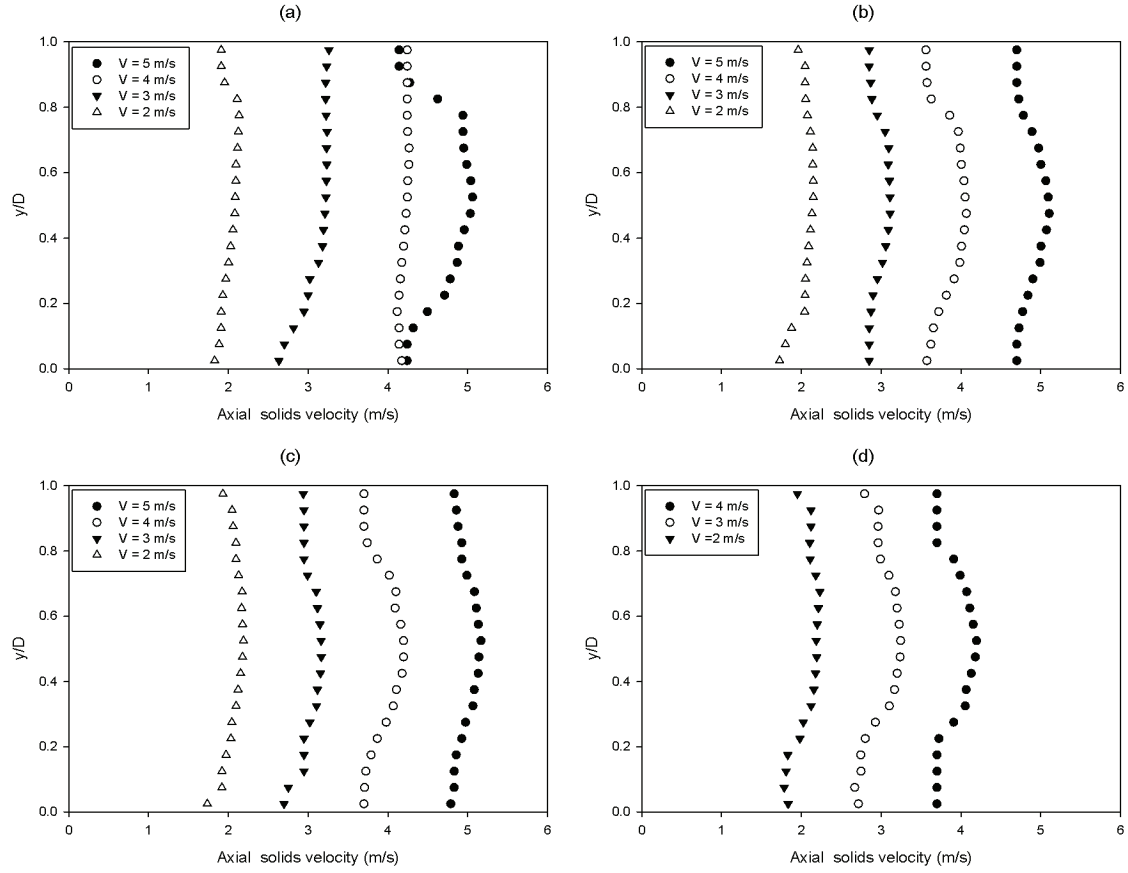

Figure 3.10: Axial velocity profiles for 100 micron sand flowing in a 52 mm pipeline loop at different mixture velocities: (a) $C_s = 20\%$; (b) $C_s = 25\%$; (c) $C_s = 30\%$; (d) $C_s = 35\%$.

age in situ solids concentrations. The velocity values plotted here are chord-averaged values. The velocity profiles are nearly axisymmetric for the flow conditions tested here. In Figure 3.11, we compare velocity profiles obtained here using cross-correlated EIT measurements with those obtained with a resistivity probe for nearly identical slurries (100μm Lane Mountain sand in water, 30% solids by volume) at SRC in the same test loop (Unpublished results from SRC). The velocity profiles are in good agreement.

Time averaged solids velocity profiles in horizontal slurry flows are usually asymmetric. The location at which the maximum solids velocity occurs varies depending

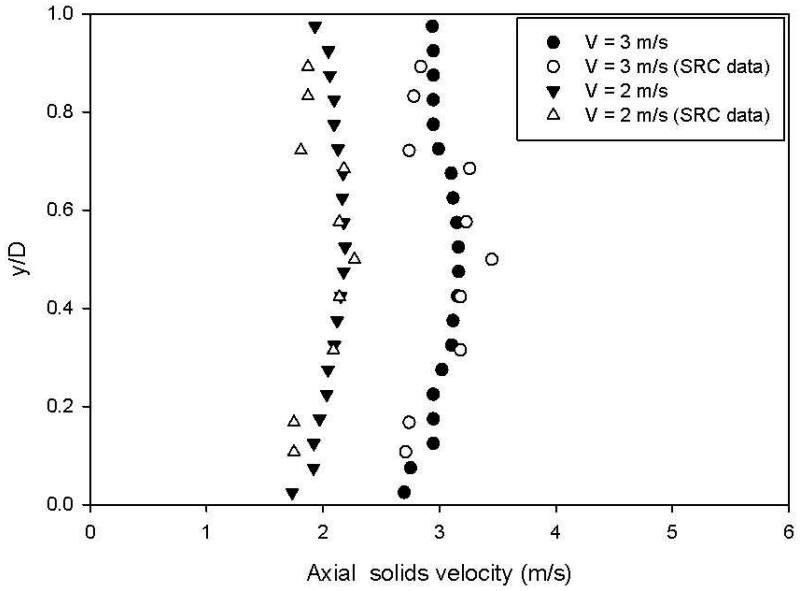

Figure 3.11: Comparison of velocity profiles measured in the present study with unpublished SRC results for 100 micron sand at $C_s = 30\%$.

on particle properties and flow conditions. Shook et al. (2) point out that the velocity defect $(u_{max} - u)$ can be used to evaluate the solids velocity profiles and the effect of fluid turbulence on solid particles. When the dispersed solids phase is mainly affected by fluid turbulence, the solids velocity defect should be comparable to that of the fluid.

The velocity defect $(u_{max} - u)$ for a single phase turbulent flow is (77):

$$\frac{(u_{max} - u)}{u^*} = 2.71 \ln(\frac{y_{max}}{y}) \tag{3.18}$$

where u_{max} is the maximum velocity and y_{max} is the position at which the maximum velocity occurs. The dimensionless velocity defect $\frac{(u_{max}-u)}{u^*}$ for $y < y_{max}$ is calculated using the solids velocity profiles obtained here (see Figure 3.10) and the result is compared to the known velocity defect distribution for single phase turbulent flow. Figure 3.12 shows the comparison of the solids velocity defect with that expected for single phase turbulent flow. The results show that in the core of the flow, the solids velocity defect is in relatively good agreement with the single phase turbulent

flow velocity defect. As $y \to 0$, the solids velocity defect starts to deviate from that calculated for single phase turbulent flow. This is probably due to particle - wall interactions (2), but a more detailed study is required to address this issue more precisely. Figure 3.12 illustrates that the dispersed solids phase is primarily affected by fluid turbulence, particularly at the pipe axis.

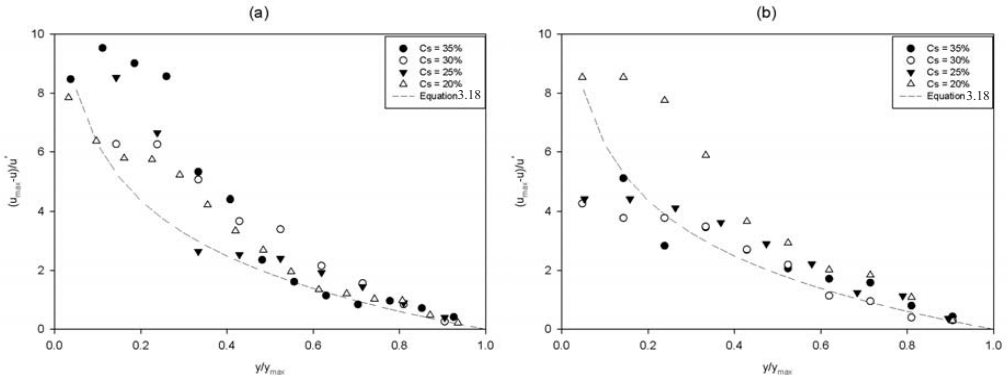

Figure 3.12: Velocity defect for solids velocity profiles of 100 micron sand flowing in a 52 mm pipeline loop at different concentrations: (a) V = 2 m/s; (b) V = 5 m/s.

3.3.2 Solids concentration fluctuations

Figure 3.13 shows solids concentration fluctuation profiles obtained at different mixture concentrations and velocities. At lower concentrations and velocities, concentration fluctuations in the lower section of the pipe are greater in magnitude than those measured in the upper section. This is due to the asymmetrical concentration profiles at lower mixture velocities and concentration. These asymmetrical fluctuation profiles become more symmetrical as solids concentration and mixture velocity increase. At higher mixture velocities, turbulent dispersion forces are much stronger and promote solids suspension, which produces a more uniform solids concentration distribution. The more uniform concentration profiles will result in more uniform concentration fluctuation profiles. More uniform concentration profiles are also partially attributable to Saffman (78) and near-wall lift forces (12). Wilson and Sellgren

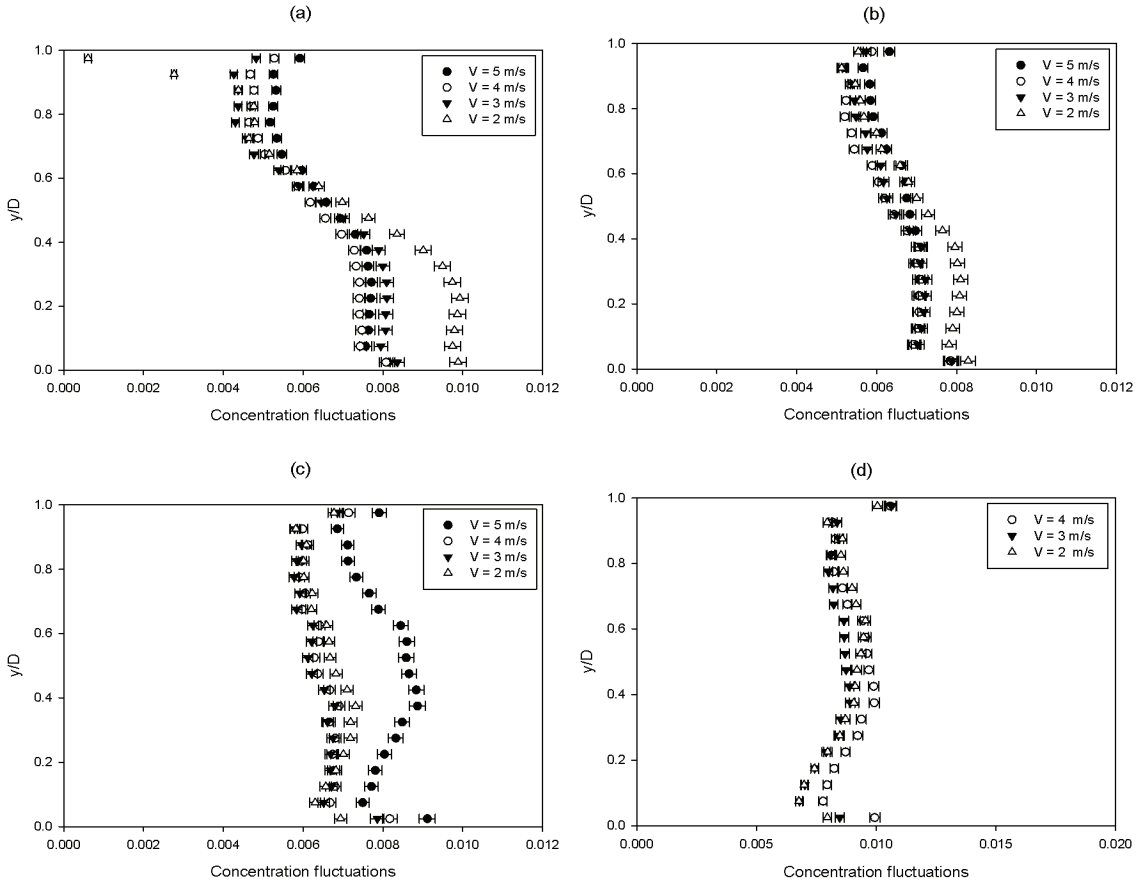

Figure 3.13: Concentration fluctuation profiles for 100 micron sand flowing in a 52 mm pipeline loop at different mixture velocities: (a) $C_s = 20\%$; (b) $C_s = 25\%$; (c) $C_s = 30\%$; (d) $C_s = 35\%$.

(12) showed that at certain conditions, near-wall lift plays an important role in promoting particle suspension. The near-wall lift force is important when the particles are partially enclosed in the boundary layer. Wilson et al.(47) showed that near-wall lift is important when d^+ is between 9 and 27 where d^+ is defined as:

$$d^+ = \frac{\rho_f d_p u^*}{\mu_f} \tag{3.19}$$

Here d_p and μ_f are particle diameter and fluid viscosity, respectively. At $d^+ < 9$, particles are fully enclosed in the boundary layer and at $d^+ > 27$ particles are fully unenclosed and they are not experiencing near-wall lift force (47). Values of d^+ for

Table 3.4: d^+ for sand particles at different velocities

Mixture velocity (m/s)	Shear velocity (m/s)	d^+
2	0.09	8.49
3	0.13	13.26
4	0.17	17.24
5	0.20	21.15

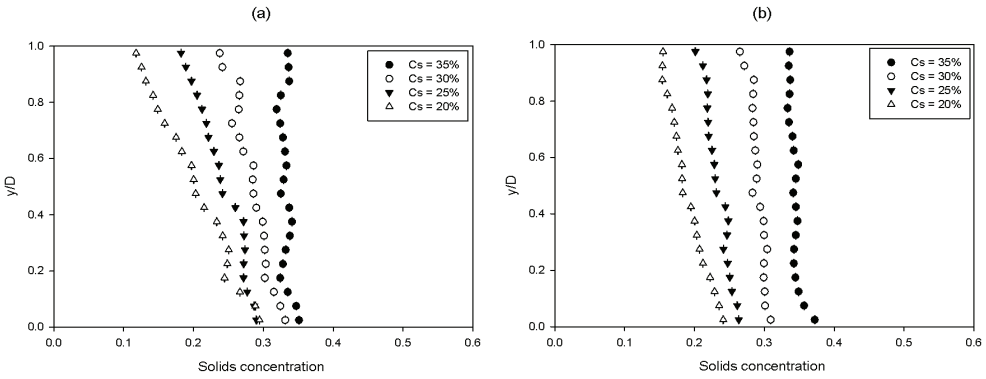

Figure 3.14: Concentration profiles for 100 micron sand flowing in a 52 mm pipeline loop at different concentrations:(a) V = 2 m/s; (b) V = 3 m/s.

the 100 micron sand used in the present study, at different velocities, are shown in Table 3.4. The results show that at 2 m/s, these particles are fully enclosed in the boundary layer and particles are not experiencing near-wall lift force. At higher velocities, $d^+ > 9$ and particles are experiencing lift force. Figure 3.14 shows concentration profiles for sand particles at 2 and 3 m/s at different concentrations. It is evident that the concentration profiles are much more uniform at 3 m/s than at 2 m/s.

The energy level of a high energy particle will decrease when it collides with a particle of lower energy level due to energy transfer during collision. An increase in the solids concentration will increase the frequency of particle collisions and consequently will increase the rate of momentum exchange between particles. This will result in an equalization of the energy distribution among the particles and should therefore produce more uniform solids concentration fluctuation profiles.

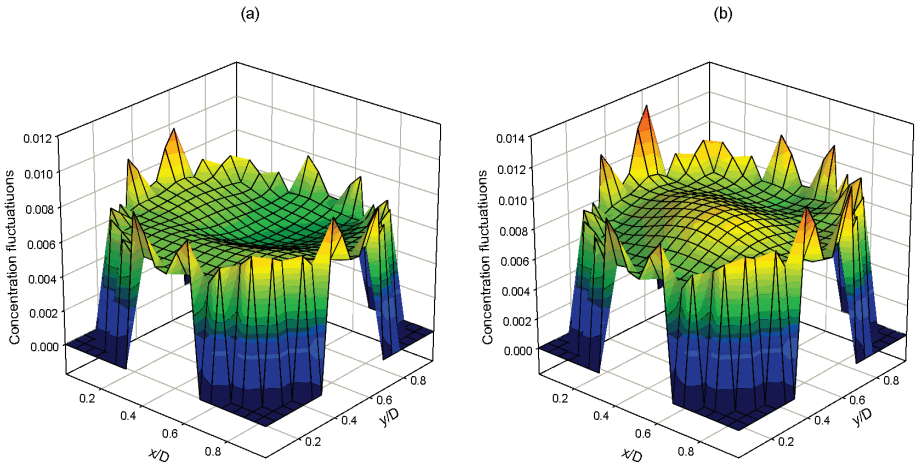

Figure 3.15: Sample solids concentration maps for 100 micron sand flowing in a 52 mm pipeline loop: (a) V = 5 m/s and C_s = 25%; (b) V = 5 m/s and C_s = 35%.

Figure 3.15 shows typical solids concentration fluctuation maps. In all cases, solids concentration fluctuations in the near-wall region were greater than those measured in the core of the flow, mainly because of solids-wall collisions and the high shear zone near the wall.

Cross–sectional averaged concentration fluctuations and the resulting power spectra are illustrated in Figure 3.16. The dotted line of Figure 3.16 represents the fluid turbulence energy decay model spectrum in the inertial sub-range. The results show that the energy of concentration fluctuations of 100 micron sand decays roughly with the same slope of solids velocity fluctuations energy, which suggests that solids-fluid turbulence interaction is an important mechanism for the production of concentration fluctuations. The energy spectrum for concentration fluctuations at lower mixture velocities shows nearly a flat portion at high frequencies (see, for example, Figures 3.16(b) and 3.16(d)). This is a result of the low signal-to-noise ratio inherent in the measurements at low mixture velocities. As the mixture velocity increases, the Kolmogrov length scale decreases and extends the turbulent dissipation range to smaller

length scales (higher frequencies). This produces stronger signals at high frequencies and increases the signal-to-noise ratio.

Zenit et al. (44) studied solids concentration fluctuations in fluidized beds and for gravity driven flows. Based on their experimental results, they concluded that the most important parameters in determination of concentration fluctuations are solids concentration and Stokes number. They suggested that solids concentration fluctuations increased with increasing Stokes number at a constant solids concentration. They calculated the Stokes number based on the particle terminal settling velocity, defining it as (44):

$$St_t = \frac{\rho_s}{\rho_f}(\frac{Re_t}{9}) \tag{3.20}$$

where Re_t is the particle Reynolds number based on the terminal settling velocity. In multiphase flows, mean quantities such as concentration fluctuations, granular temperature and pressure gradient could be expressed as a function of mean concentration and mixture velocity. However, in a fluidized bed, these mean values could be expressed as a function of either mean concentration or mean velocity as these two parameters are related and are not independent values, i.e. any given mean concentration corresponds to a specific fluidization velocity. In slurry pipe flow, the mean concentration and level of turbulence are independent variables and both affect any mean quantity. As a consequence, the Stokes number based on terminal settling velocity is not applicable to slurry pipe flows. In order to investigate the applicability of Zenit and Hunt's (44) finding to slurry pipe flows, a new definition for Stokes number for slurry pipe flows was employed. The particle Stokes number is defined as (79):

$$St_s = \frac{1}{18}\frac{\rho_s}{\rho_f}(\frac{d_p}{\eta})^2 \tag{3.21}$$

Here, the Kolmogrov length scale is used to account for the level of fluid turbulence. Table 3.5 shows the calculated Stokes number for the 100 micron sand particles

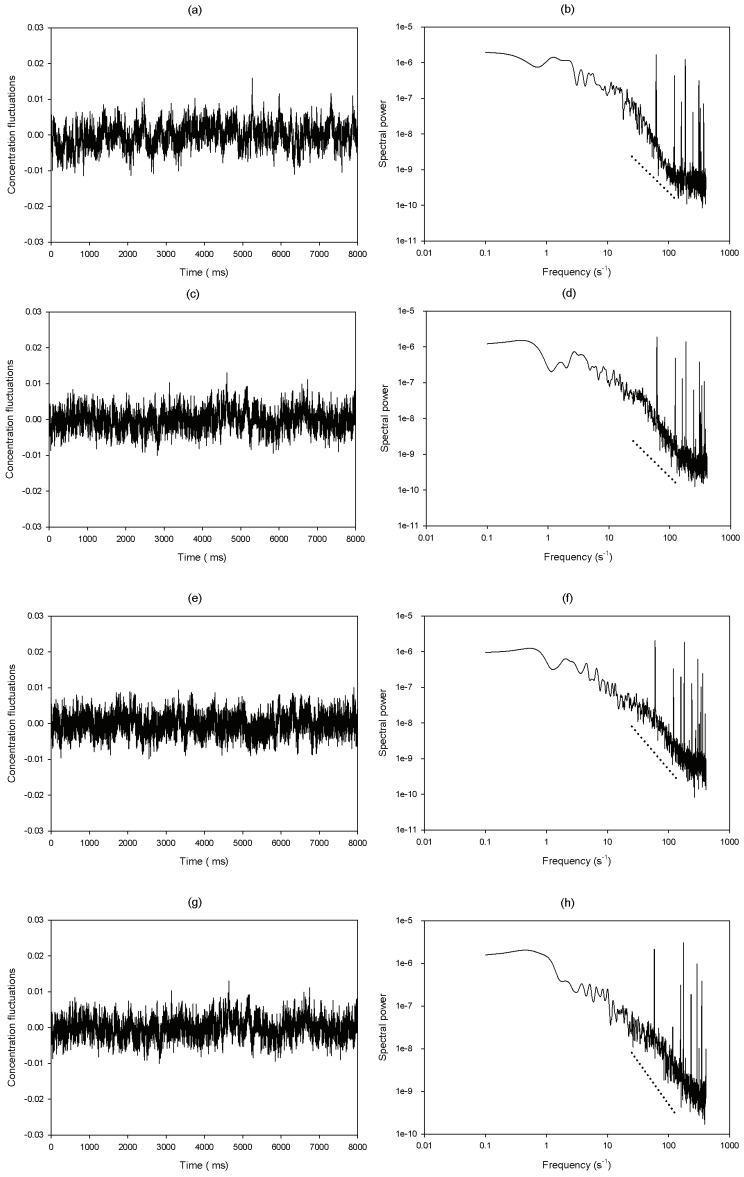

Figure 3.16: Time and frequency domain plots of cross sectional averaged solids concentration fluctuation for 100 micron sand flowing in a 52 mm pipeline loop at $C_s = 20\%$: (a) and (b) V = 2 m/s; (c) and (d) V = 3 m/s; (e) and (f) V = 4 m/s; (g) and (h) V = 5 m/s. Dotted lines are the model spectrum (Equation 3.14) decay rates.

at different mixture velocities. The results show that Stokes numbers are relatively small for the sand particles tested here, meaning that the particle's response time is relatively small compared to the characteristic flow time scale.

Table 3.5: Stokes number for sand particles at different solids concentration

Mixture velocity (m/s)	η (μm)	St_s
2	28.2	1.77
3	21.2	3.27
4	17.3	4.92
5	14.8	6.72

Aguilar et al. (80) mention that at Stokes numbers below the critical value of 10 ± 5, collisions are dampened by the interstitial fluid and direct particle-particle collisions are unlikely to happen. The definition of Stokes number here is similar to Equation 3.20 but instead of terminal settling velocity, the impact velocity has been used to determine the Reynolds number. At low Stokes numbers, fluctuations in particle motion are caused by particle-fluid interactions. Filtered cross-sectional averaged concentration fluctuations and Stokes numbers calculated using Equation 3.21 were compared with Zenit and Hunt's (44) experimental data and the Buyevich and Kapbasov(57) models for high frequency solids concentration fluctuations. The results show increases in filtered RMS concentration fluctuation with increasing concentration. Due to experimental limitations, it was not possible to run the experiments at concentrations beyond 35%. More experimental results at higher concentration are needed to comment on the concentration at which the maximum fluctuation occurs. These results are shown in Figure 3.17(a). Comparison of our RMS solids concentration fluctuations with those obtained by Zenit and Hunt is illustrated in Figure 3.17(b). Note that the effect of fluid turbulence in pipe flows is implicitly accounted for in the Stokes number and is not explicitly expressed in the figure. Concentration fluctuations are generally smaller in our experiments, which is expected because Zenit and Hunt(44) showed that the solids concentration fluctuations decreased with decreasing Stokes number. Buyevich and Kapbasov (1994)

obtained the following mathematical model for calculation of random small scale fluctuations based on the Carnahan-Sterling and Enskog models. Their model, based on the Carnahan-Sterling model, is

$$\acute{C}_s^2 = [1 - 2C_s \frac{4 - C_s}{(1 - C_s)^4}]^{-1} \tag{3.22}$$

where $\acute{C}_s$ and C_s are RMS solids concentration fluctuations and average solids concentration, respectively. They mentioned that the application of this model shown above to dense mixtures might not hold since it is based on chaotic states of a gas. To address this concern, they introduced an alternative model, based on the Enskog model for dense gases, which is expressed as:

$$\acute{C}_s^2 = C_s^2[1 - (\frac{C_s}{C_{max}})^{1/3}][1 + \frac{1}{3}(\frac{(\frac{C_s}{C_{max}})^{1/2}}{1 - (\frac{C_s}{C_{max}})^{1/2}})]^{-1} \tag{3.23}$$

where C_{max} is the maximum packing fraction for the solids which can be taken as the solids concentration in the packed bed state. Both the above equations were compared in the present work.

Figure 3.17(b) shows the comparison of the present results with the previous work by Zenit and Hunt (44) and the theoretical models (Equations 3.22 and 3.23). In Figure 3.17(b), the solids and dashed lines represent these two theoretical models. Not surprisingly, both models provide unsatisfactory predictions, as was previously observed by Zenit and Hunt. The models predict only the limiting case where $St \rightarrow \infty$. The comparison suggests the relationship between concentration fluctuations, solids concentration and Stokes number is not only valid for fluidized beds and gravity driven flows, but also holds for pipe flows provided that an appropriate definition of the Stokes number is employed.

3.4 Summary

The RMS solids concentration fluctuations of high-concentration sand slurries ($d_{50} = 100\mu m$) in horizontal pipe flow were obtained using high–speed Electrical Impedance

Tomography (EIT) for a range of in situ solids concentration and mixture velocities. In general, the solids concentrations fluctuations and solids axial turbulent intensities are higher near the wall because of particle-wall collisions and because of the presence of the high shear zone near the wall. At constant solids concentrations, the magnitude of the concentration fluctuations increases with increasing mixture velocity.

Time-series power spectra of concentration- and velocity- fluctuations (averaged over the pipe cross section) were obtained using the Fast Fourier Transform (FFT) technique. This analysis showed that the rate of decay in solids fluctuations is closely related to the turbulent energy decay in the dissipation range for single–phase flow, suggesting that solids concentration fluctuations are produced primarily through particle-fluid turbulence interactions. Comparison of the calculated turbulence length scale with the solids length scale (i.e. particle diameter) illustrated that, for these slurries, the particles interact with turbulent eddies in the dissipative range of the turbulent energy spectrum. Additionally, measurements of the local, time-averaged solids velocity distributions were used to calculate velocity defect profiles for these flows. The velocity defect profiles were very similar to those expected for single-phase turbulent flow (at the same flow conditions), particularly in the core of the flow.

Finally, the cross-sectional averaged concentration fluctuations were compared to experimental data previously reported for fluidized bed experiments and for gravity driven flows. The present results were consistent with the findings previously reported: that is, that the magnitude of the concentration fluctuations increases with in situ concentration and should be expected to increase with increasing Stokes number. We have demonstrated that the solids concentration fluctuation results obtained for turbulent slurry flow can be compared to those collected using fluidized beds if an appropriate Stokes number is defined.

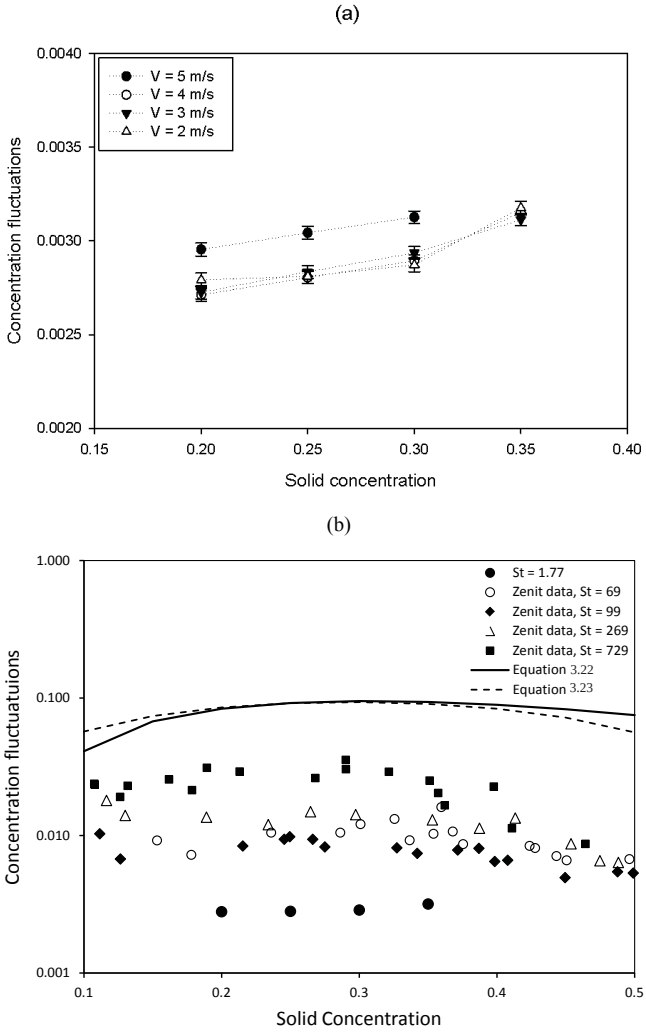

Figure 3.17: (a) Cross-sectional averaged concentration fluctuations at different concentrations and velocities: (b) Comparison of the results of the present study with data obtained by Zenit and Hunt.

4

Study of a solid–liquid fluidized bed using high speed Electrical Impedance Tomography

Material in this chapter has been submitted for publication to: *Hashemi, S.A., Kroll-Rabotin, J.S., Shokri, R., Sanders, R.S., (2013). " Experimental study of a solid-liquid fluidized bed using high speed Electrical Impedance Tomography. Chem. Eng. Sci.*

4.1 Introduction

Liquid-solid fluidized beds are widely encountered in many processes in the food production, pharmaceutical, chemical and biochemical industries. Examples of such applications are particle classification and separation, liquid-fluidized bed heat exchangers (FBHX), fluidized bed catalytic reactors and bioreactors (20; 81). Apart from their significant industrial applications, solid-liquid fluidized beds provide an ideal opportunity to study two-phase flows and particularly fluid-particle and particle-particle interactions (20).

Recent advances in multiphase flow simulation methods and computational resources have enabled researchers to directly solve the governing equations of motion and to resolve the flow in great detail. However, these methods need enormous

computing resources and are limited to cases of very dilute flows and low Reynolds numbers. However, most industrial processes deal with high concentrations and high Reynolds number flows. The computing power required to apply advanced numerical methods to industrial scales cannot be expected in the foreseeable future.

A common technique to overcome time and spatial resolution problems in computational fluid dynamics (CFD) for industrial cases is to employ time-averaged equations of motion. The ability of models of this type to accurately replicate the flow structure (phase concentrations and velocities) and behaviour (pressure drops and deposition velocities) is contingent upon the use of reliable and precise models to capture particle-particle and particle-fluid interactions. These so-called "closure" models are often semi-empirical in nature and thus reliable experimental data are required to validate these models and improve the understanding of important physical mechanisms that govern these complex and highly coupled interactions.

One of the objectives in modeling solid–liquid flows is to develop models to accurately predict the level of solids phase fluctuations. Various models such as those of Foscolo and Gibilaro (82), Batchelor (83) and Koch (84) have been developed over the past years to estimate the solids phase fluctuations.

Zenit et al. (19) investigated the collisional particle pressure in solid-liquid fluidized beds for different particle sizes and densities. Their results showed that collisional particle pressure, which originates from particle-particle and particle-wall collisions, are a function of particle density ratio, terminal settling velocity and solids concentrations. They also compared their results against different models and showed that the performance of these models are poor. They concluded that this poor performance is mostly due to limited understanding of the phenomena (19).

Zenit and Hunt (44) studied solids concentration fluctuations in gravity driven flows and fluidized beds at different particle diameters, densities and solids concentrations. They compared their results with the Buyevich and Kapbasov (57) model and found that solids concentration fluctuations were dependent on particle Stokes number and bulk solids concentrations. Solids concentration fluctuations increased

with increasing the Stokes number at constant solids concentration.

Gevrin et al. (20) used an Eulerian two-fluid approach to investigate the granular pressure in a solid-liquid fluidized bed. They performed their numerical study based on the flow configuration of Zenit et al. (19) experiments for nylon, glass and steel particles and obtained satisfactory agreement between experimental and simulation results. They also compared their numerical results with the experimental Richardson-Zaki law with an exponent of 2.4, which is characteristic for turbulent drag. They found the exponent of 2.8 for nylon and glass particles and 2.5 for steel particles based on the numerical results and showed that the simulation results provide a good approximation of experimental results using the Richardson-Zaki "law".

Kechroud et al .(60) analyzed the dynamic behaviour of the continuous phase in a fluidized bed. They compared the continuous phase velocity fluctuations with Zenit and Hunt's (44) solids concentration fluctuations. They found that there is a high degree of similarity between continuous phase velocity fluctuations and solids concentration fluctuations.

These works provided excellent insight into highly concentrated liquid-solid systems. However, the measurements were limited to cross-sectional average values with no information on the solids concentrations and concentration fluctuation distributions within the flow domain. Such local information is important especially in determining the mechanism(s) responsible for producing solids fluctuations (e.g. particle-wall interactions).

One of the difficulties associated with experiments involving concentrated multiphase flows is paucity of viable measurement techniques. Common measurement techniques, such as PIV (Particle Image Velocimetry) and LDV (Laser Doppler Velocimetry), are limited to single phase and very dilute transparent multiphase flows.

Recent advances in measurement techniques, and especially the development of process tomography methods such as electrical tomography, have opened a new window in experimental multiphase research. Electrical tomography methods are non-intrusive, robust and are capable of performing measurements in opaque and

highly-concentrated flows. In the past decade, electrical tomography techniques have been used to study many different multiphase flow systems, including flow distribution and velocity measurements in a fixed bed reactor (40), hydraulic conveying of materials (41) and fluidization (39; 42).

In the present work, high speed Electrical Impedance Tomography (EIT) is used to measure local solids concentration and concentration fluctuations in a solid-liquid fluidized bed. The results are then used to infer the mechanism(s) that are responsible for producing these fluctuations. The results are also compared to previous experimental data and numerical simulations available in the literature. Measurements of this type are required to develop and improve the modeling framework for multiphase flows.

This chapter is organized as follows: in section 4.2, the details of the experimental setup, materials and measurement techniques are described. The methods used to analyze the data are briefly presented in section 4.3. In section 4.4, the experimental results and comparisons of the current work with previous researches are discussed.The main results and findings are summarized in the last section.

4.2 Experimental setup

A 10.16 *cm* (i.d.) fluidized bed setup at the Pipeline Transport Processes Centre at the University of Alberta, Canada, was used to perform the experiments. A schematic layout of the setup is shown in Figure 4.1. The apparatus is equipped with a variable speed centrifugal pump to circulate fluid at different velocities. The liquid velocity was measured using an orifice meter and the pressure drop across orifice plate was measured using a Valydyne differential pressure transducer. Additional details of the experimental apparatus and its operation can be found in Appendix B. Mono-size glass beads were used to perform the experiments. Important properties of the particles are listed in Table 4.1. The terminal settling velocities are experimental values. Particles were added to the bed from the solids feeder and were held in the

bed using two screens at the bottom and top sections of the bed. A flow straightener was installed at the bottom of the working section to minimize the effect of the upstream elbow on the liquid flowing into the bed. Different bed concentrations were achieved by operating at different superficial velocities.

Table 4.1: Important properties of glass beads.

$d_p(mm)$	$\rho s/\rho f$	$u_t(cm/s)$	Re_t	St_t
2	2.54	21.5	430	121
3	2.54	31.8	954	269
4	2.54	37.5	1500	423

An Industrial Tomography Systems (ITS) Z8000 Electrical Impedance Tomography (EIT) data acquisition system along with a dual-plane sensor was employed to measure the solids concentration distribution. The instrument provides measurements of the resistivity distribution map within the sensor planes. The resistivity map is then converted to solids concentration using the Maxwell equation (36).

Figure 4.2 shows the EIT reconstruction grid. The map divides the bed cross section into 316 pixels of equal area. The solids concentration within each pixel is measured.

For each set of experiments, 8000 conductivity maps were collected at a sampling rate of 820 Hz at each velocity from each sensor plane. The resulting concentration maps were used to calculate solids concentration fluctuations maps.

4.3 Analysis

The root-mean-square (RMS) solids concentration fluctuations computed from:

$$\acute{C}_s = \sqrt{\frac{1}{N}\sum_{i=1}^{N}(\bar{C}_s - C_{si})^2} \tag{4.1}$$

where N, $\acute{C}_s$,$\bar{C}_s$ and C_{si} are the number of measurements, RMS solids concentration fluctuations, average solids concentration and instantaneous solids concentration,

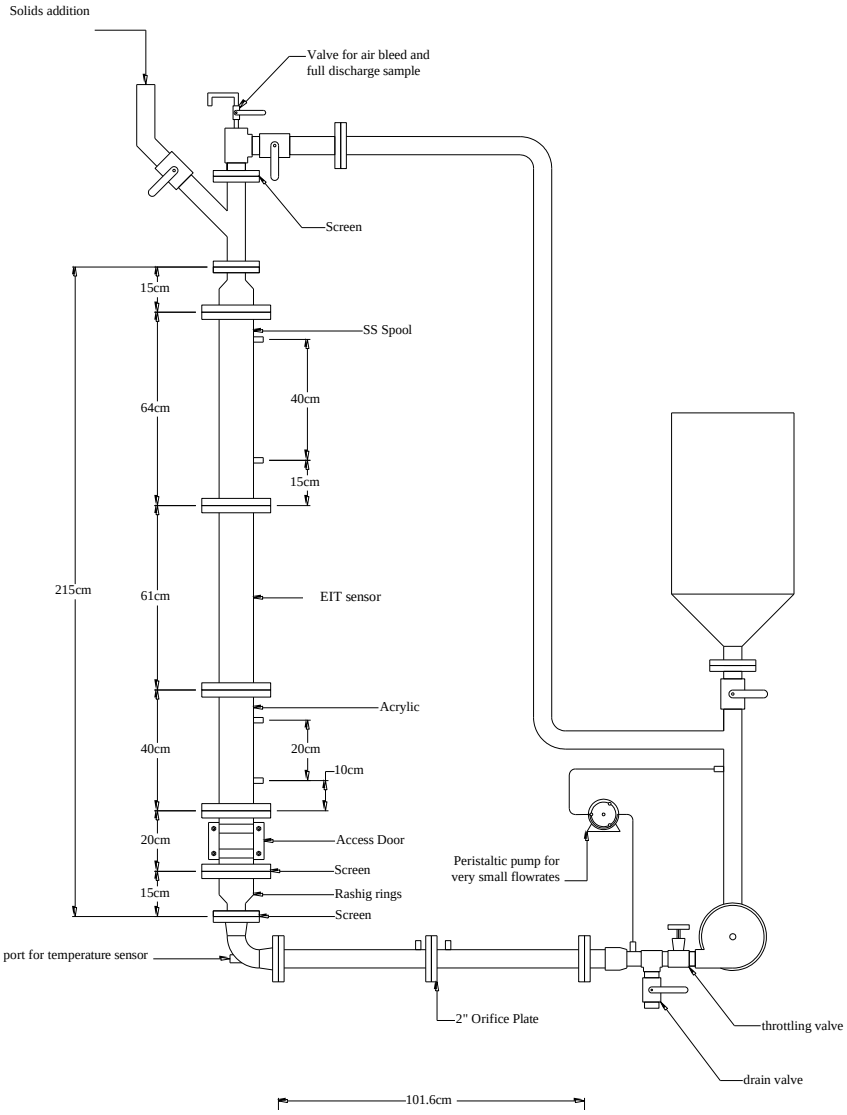

Figure 4.1: Schematic of the 10.16 *cm* fluidized bed setup

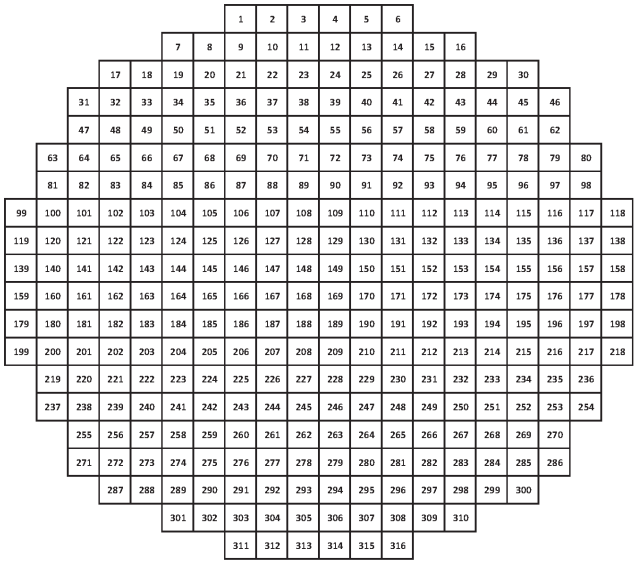

Figure 4.2: Schematic diagram of EIT reconstruction grid

respectively. The average solids concentration was also calculated using:

$$\bar{C}_s = \frac{1}{N}\sum_{i=1}^{N} C_{si} \tag{4.2}$$

The Confidence Interval for measurements was estimated as (66):

$$C.I. = \pm 1.96 \times SE \tag{4.3}$$

where SE is the Standard Error and is defined as:

$$SE = \frac{S}{\sqrt{N}} \tag{4.4}$$

Here, S and N are standard deviation and number of measurements, respectively.

The particle Reynolds number at terminal settling velocity was calculated from:

$$Re_t = \frac{\rho_f u_t d_p}{\mu_f} \tag{4.5}$$

The terminal Stokes number is also calculated using (44):

$$St_t = \frac{\rho_s}{\rho_f}\frac{Re_t}{9} \tag{4.6}$$

4.4 Results and discussion

Figures 4.3–4.5 show typical solids concentration and concentration fluctuations maps for 2, 3 and 4 mm glass beads, respectively. In these figures, r is the distance from the center of the column and R is the column radius. The magnitude of the local solids concentration fluctuations is typically similar everywhere except near the wall where it is usually higher. The higher concentration fluctuation values near the wall could be due to particle-wall collisions and the higher shear zone near the wall.

Solids radial concentration and concentration fluctuation distributions which have been obtained from the concentration maps, are shown in Figures 4.6–4.8. Solids concentration maps and radial concentration profiles both show that the local concentration is lower in the center. The reduced concentration in the central region has been observed previously and is said to be associated with aggregative (bubbling) liquid fluidization (82; 85; 86).

This phenomenon is illustrated in Figure 4.9 where concentration maps from two different axial locations are compared. The results shown here correspond to conditions where the first sensor plane is inside the bed and the second one is above the bed. The results clearly show that the bed expansion is higher in the centre due to the bubbling flow regime and production of mushroom type flow structures.

Foscolo and Gibilaro (82) developed a model to predict the onset of aggregate (bubbling) behavior in liquid fluidized beds by considering the primary interaction forces of buoyancy and drag that support the particle weight. Based on their fluid-particle interaction model, they obtained a method to estimate the elastic wave velocity, u_e, which is analogous to the sonic velocity in compressible flows:

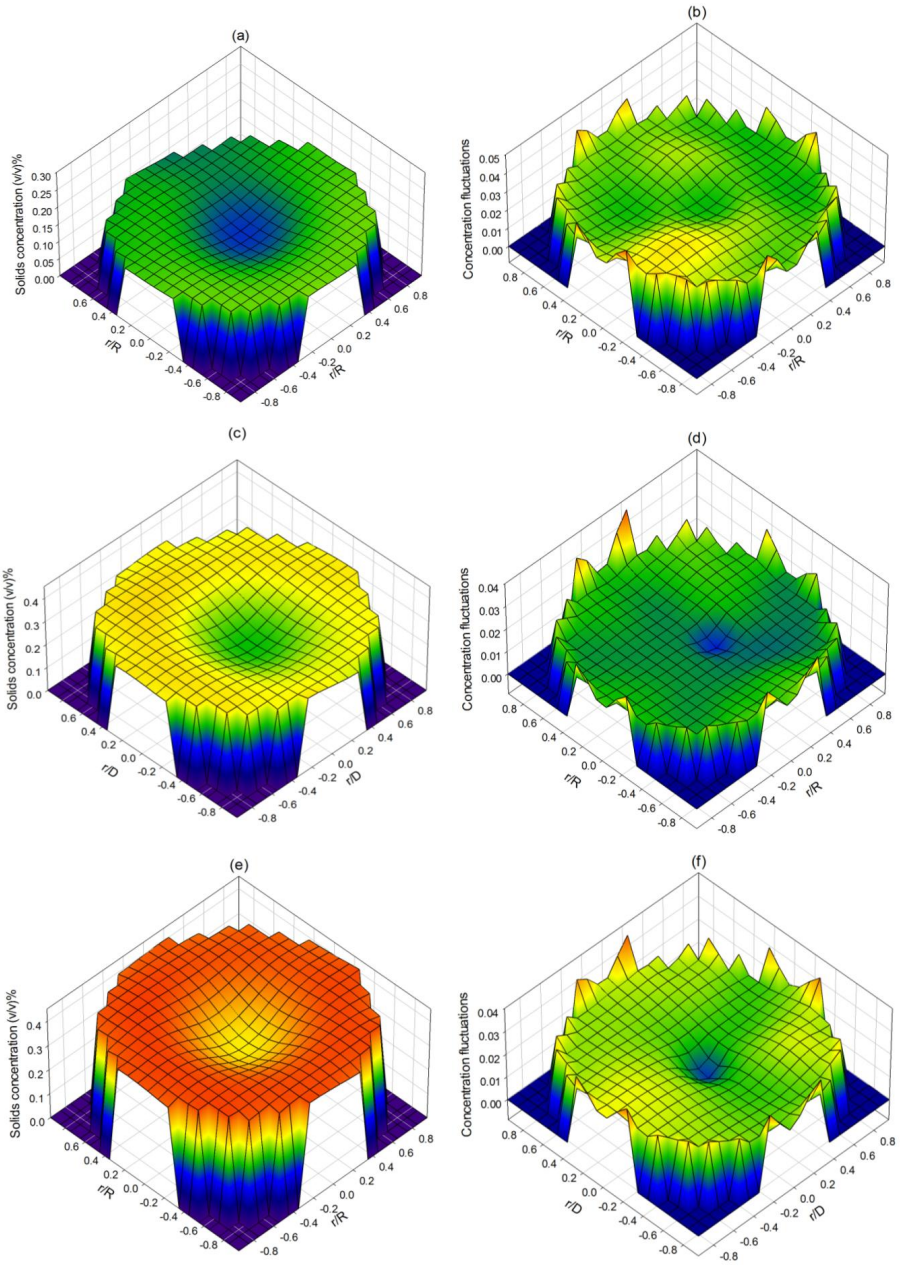

Figure 4.3: Solids concentration and concentration fluctuations map for 2 mm glass beads: (a) and (b) $C_s = 15\%$; (c) and (d) $C_s = 30\%$; (e) and (f) $C_s = 40\%$.

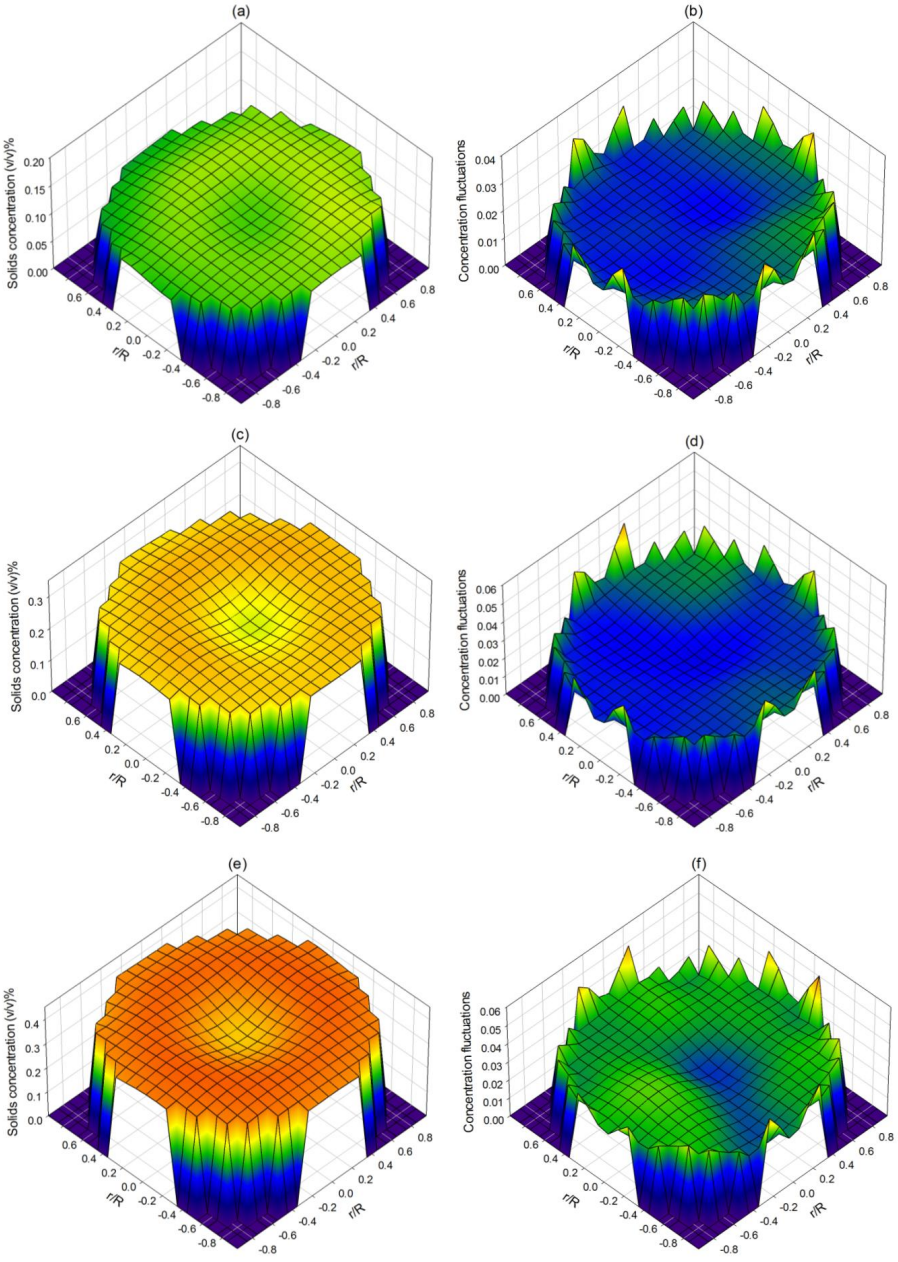

Figure 4.4: Solids concentration and concentration fluctuations map for 3 mm glass beads: (a) and (b) $C_s = 11\%$; (c) and (d) $C_s = 26\%$; (e) and (f) $C_s = 38\%$.

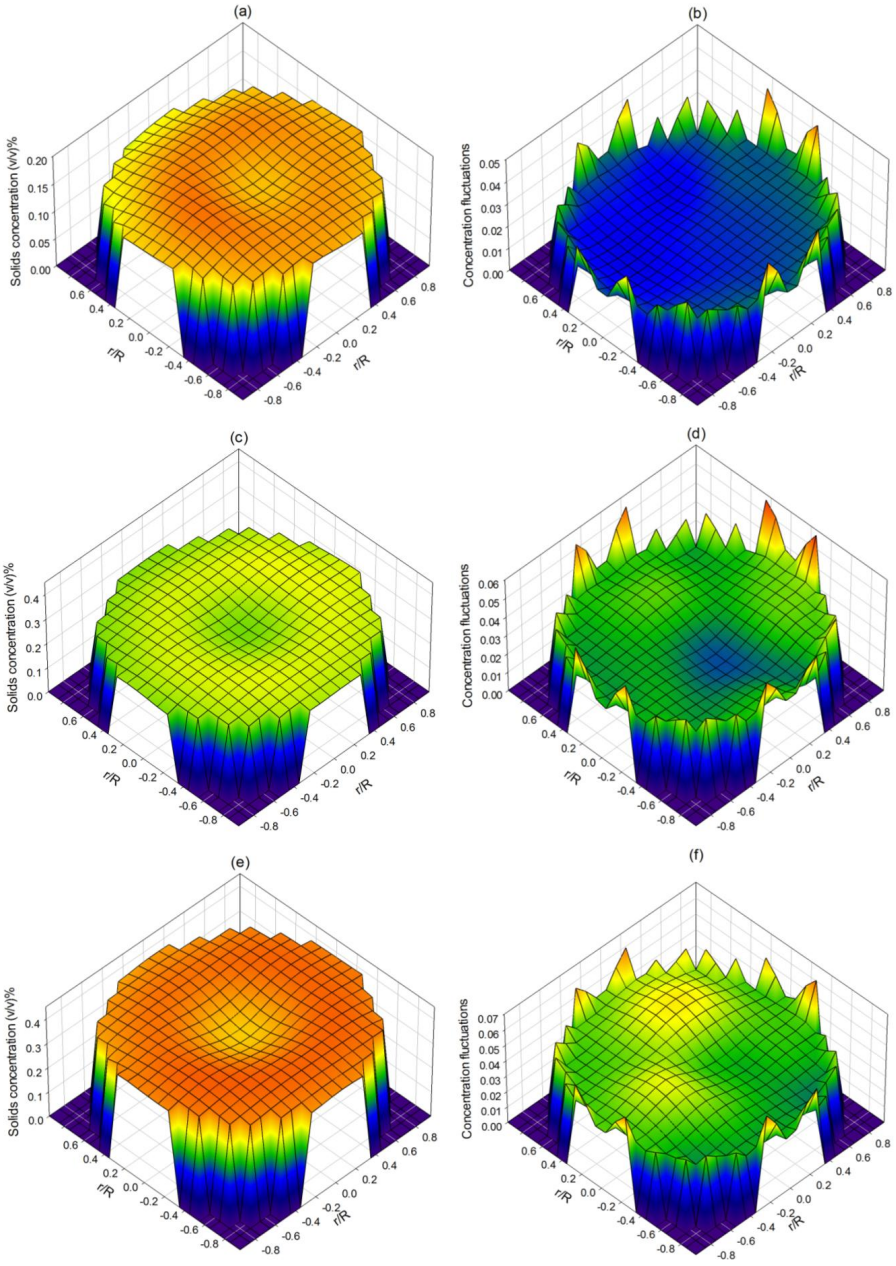

Figure 4.5: Solids concentration and concentration fluctuations map for 4 mm glass beads: (a) and (b) $C_s = 15.5\%$; (c) and (d) $C_s = 28\%$; (e) and (f) $C_s = 38\%$.

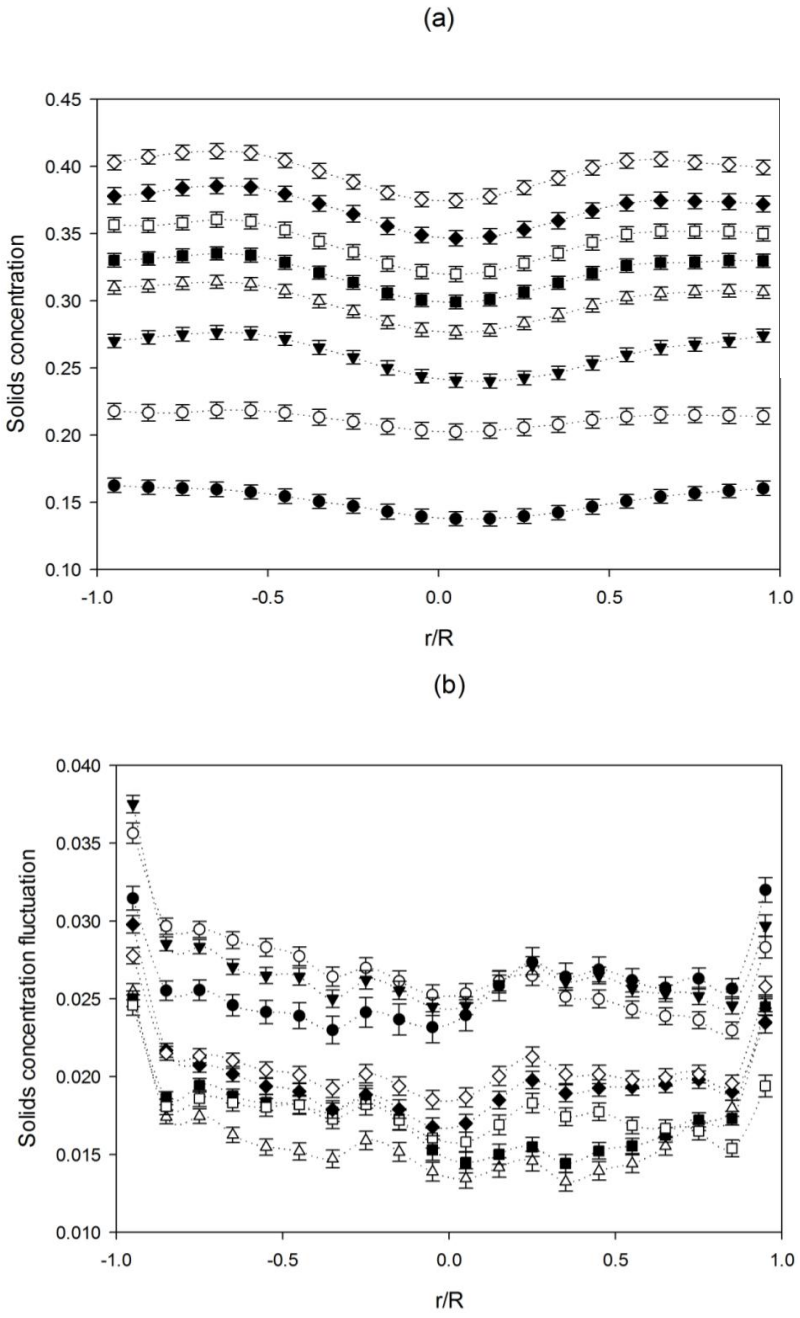

Figure 4.6: Solids concentration and concentration fluctuations profiles for 2 *mm* glass beads: $C_s = 15\%$ (●); $C_s = 21\%$ (○); $C_s = 26\%$ (▼); $C_s = 30\%$ (△); $C_s = 32\%$ (■); $C_s = 34\%$ (□); $C_s = 37\%$ (◆); $C_s = 40\%$ (◇).

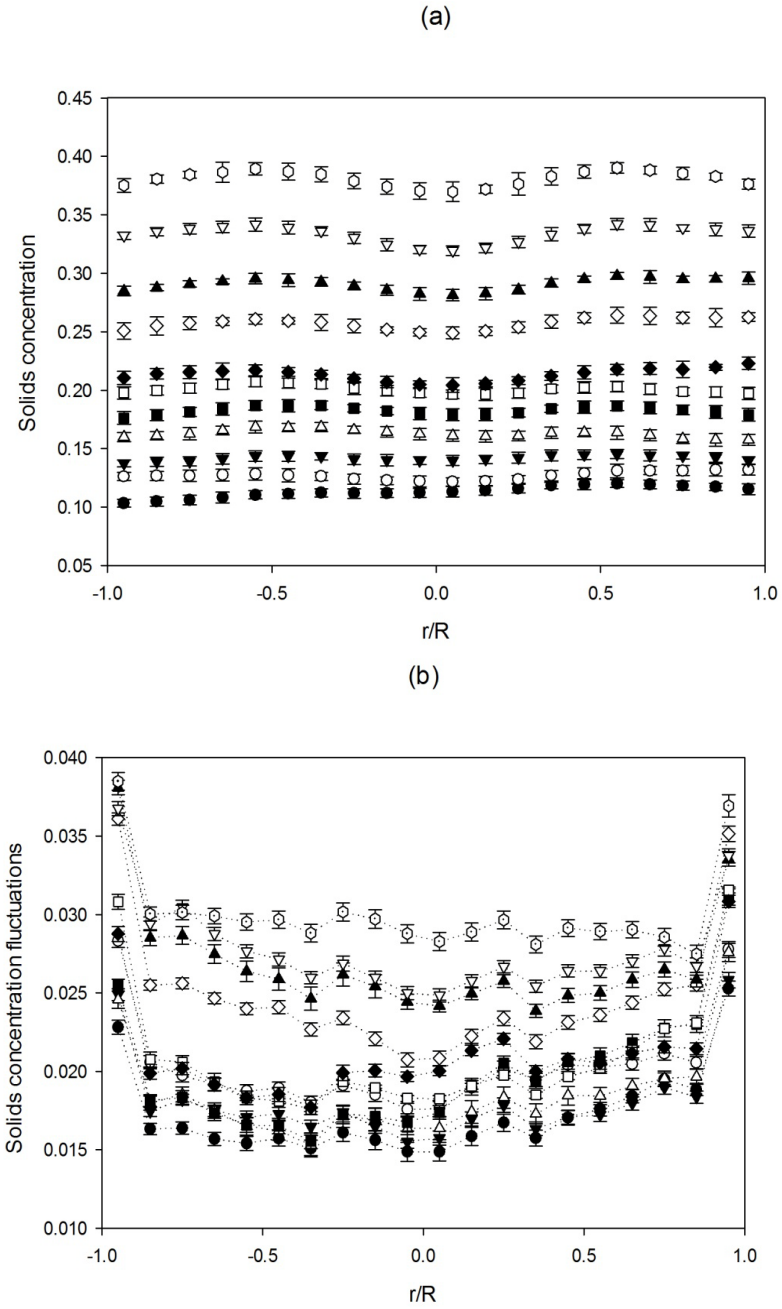

Figure 4.7: Solids concentration and concentration fluctuations profiles for 3 *mm* glass beads: $C_s = 11\%$ (●); $C_s = 12.5\%$ (○); $C_s = 14\%$ (▼); $C_s = 16\%$ (△); $C_s = 18\%$ (■); $C_s = 20\%$ (□); $C_s = 21\%$ (◆); $C_s = 26\%$ (◇); $C_s = 29\%$ (▲); $C_s = 33\%$ (▽); $C_s = 38\%$ (⬡).

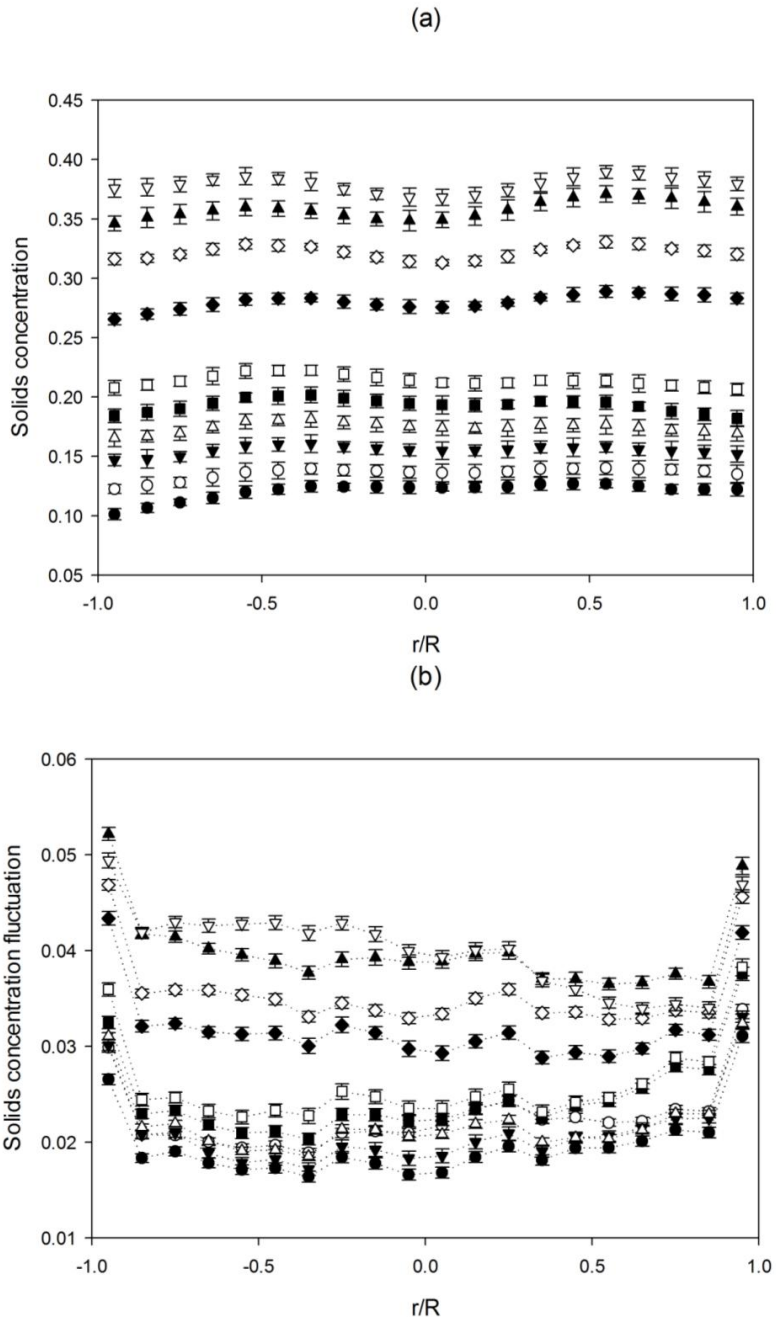

Figure 4.8: Solids concentration and concentration fluctuations profiles for 4 mm glass beads: $C_s = 12\%$ (●); $C_s = 13.5\%$ (○); $C_s = 15.5\%$ (▼); $C_s = 17.5\%$ (△); $C_s = 19\%$ (■); $C_s = 21.5\%$ (□); $C_s = 28\%$ (◆); $C_s = 32\%$ (◇); $C_s = 36\%$ (▲); $C_s = 38\%$ (▽).

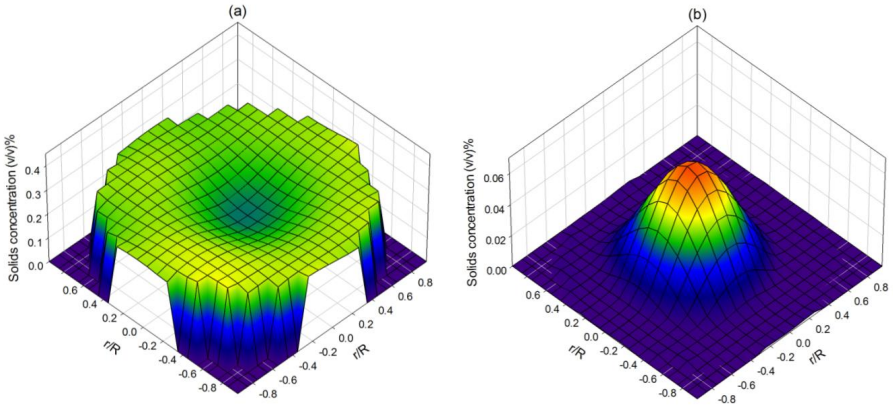

Figure 4.9: Solids concentration maps for 3 mm glass beads at $C_s = 26\%$: (a) Sensor plane 1 (inside the bed); (b) Sensor plane 2 (above the bed)

$$u_e = [\frac{3.2gd_p(1-\epsilon)(\rho_p - \rho)}{\rho_p}]^{0.5} \tag{4.7}$$

where ϵ is the void fraction. They noted that the stability of a liquid fluidized bed is determined by the elastic velocity and the voidage propagation velocity, u_ϵ, which is given by:

$$u_\epsilon = nu_t(1-\epsilon)\epsilon^{0.5} \tag{4.8}$$

where n is the Richardson-Zaki exponent. They introduced a stability criterion based on a dimensionless function, F_u:

$$F_u = \frac{u_e - u_\epsilon}{u_e} \tag{4.9}$$

Positive values of F_u indicate particulate fluidization, while negative values indicate bubbling (aggregative) solid–liquid fluidization.

The F_u values as a function of solids concentration for 2, 3 and 4 mm glass bead particles are shown in Figures 4.10. For 3 and 4 mm particles, solids concentrations between 15% and 39% will results in negative Fu values and bubbly behavior. This

is in agreement with experimental data where the low concentration region in the center is not present, but gradually develops as the solids concentration increases.

In the case of the fluidization experiments conducted with the 2 mm glass beads, F_u is positive at all solids concentrations meaning that particulate fluidization is expected at all fluidization velocities. This prediction contradicts the experimental results, which clearly show the lower concentration region in the center of the bed. The discrepancy is probably related to the fact that transition from particulate to bubbling fluidization is a gradual process and is preceded by the development of propagating high voidage bands, which have also been detected for 1.5 mm glass beads (85). In this case, the voidage bands do not continue to form complete void regions, but will produce lower time-averaged solids concentrations in the center of the column.

The cross sectional averaged concentration fluctuations are calculated from the concentration fluctuations map and the results were compared to experimental work of Zenit et al. (44) for 3 mm glass beads. This comparison is illustrated in Figure 4.11. The cross-sectional averaged values show good agreement with those obtained by Zenit et al. (44).

Kechroud et al. (60) measured the liquid velocity fluctuations above a solid-liquid fluidized bed. They compared their results with solids concentration fluctuations previously obtained by other researchers. They showed that a strong analogy between fluid velocity fluctuations and solids concentration fluctuations exists in solid-liquid fluidized beds. Comparison between cross-sectional averaged solids concentration fluctuations obtained from EIT measurements and the liquid velocity fluctuations obtained by Kechroud et al. (60) is illustrated in Figure 4.12. The results confirm Kechroud et al. conclusion and demonstrate good agreement between solids concentration fluctuations measured here and the liquid velocity fluctuations.

The minimum superficial fluid velocity required to fluidize a bed of particles to a given solids concentration is typically taken as the hindered settling velocity of particles at the same solids concentration (81). Thus, the Richardson-Zaki equation

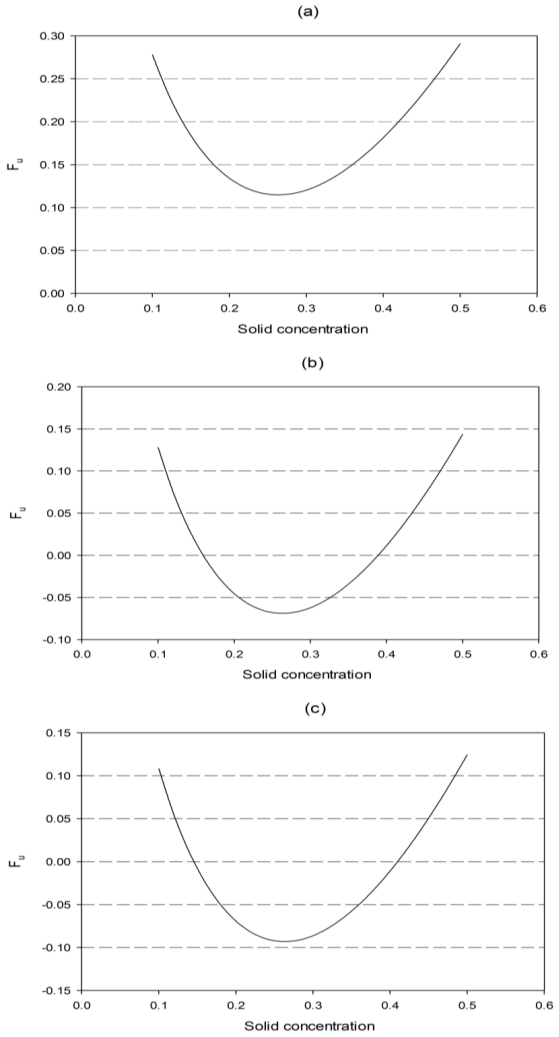

Figure 4.10: Stability criterion (F_u) as a function of solids concentration: (a) 2 mm glass beads; (b) 3 mm glass beads; (c) 4 mm glass beads.

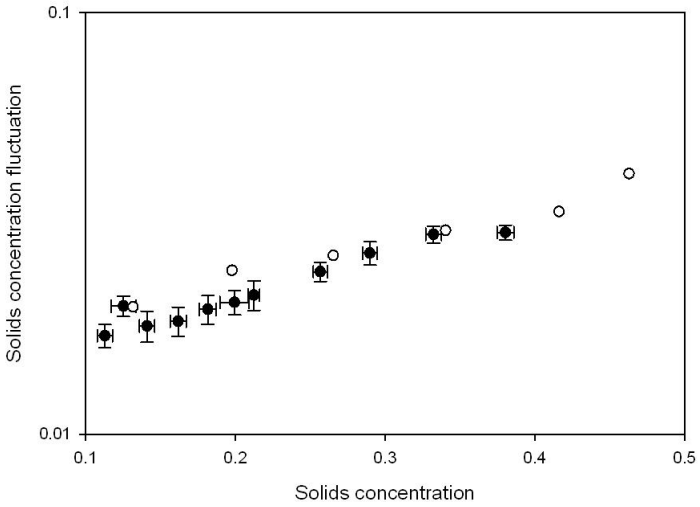

Figure 4.11: Cross sectional averaged concentration fluctuation for 3 *mm* glass beads: Current Experimental results (●); Data obtained from Zenit and Hunt(○).

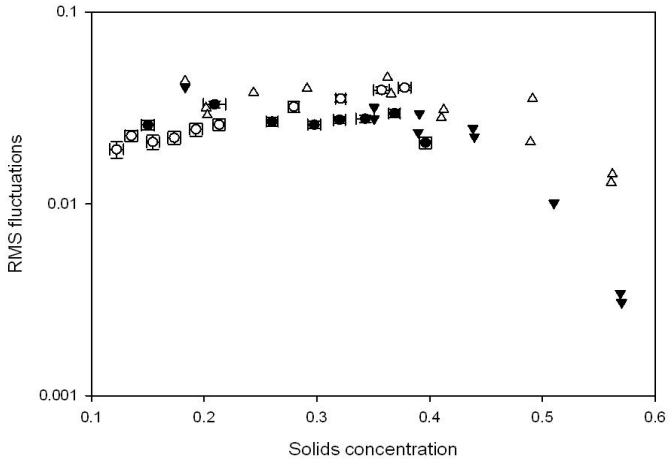

Figure 4.12: Comparison between RMS solids concentration (current study) and liquid velocity fluctuations in solid-liquid fluidized beds (Kechroud et al.): RMS solids concentration fluctuations (●) and liquid velocity fluctuation (▼) for 2 *mm* glass beads; RMS solids concentration fluctuations (○) and liquid velocity fluctuations (△) for 4 *mm* glass beads.

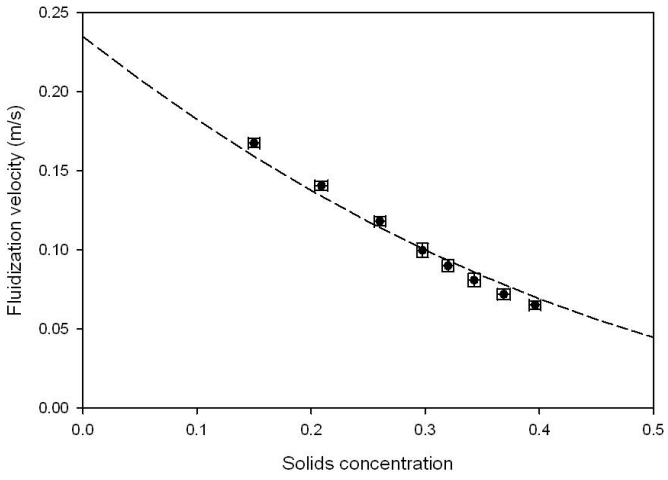

Figure 4.13: Fluidization velocity vs. solids concentration in the bed for 2 mm glass beads: Current experimental results (●); Richardson-Zaki equation with n = 2.4 (Dashed line)

for hindered settling velocity could be used for solid-liquid fluidization:

$$u_0 = u_t(1 - C_s)^n \tag{4.10}$$

where u_0 is fluidization velocity. Zenit et al. (19) used the value of $n = 2.4$ for glass beads based on their experimental results. The comparison of fluidization velocity versus solids concentration obtained from EIT measurements with predictions made using the Richardson-Zaki equation ($n = 2.4$) for 2 mm and 4 mm glass beads is shown in Figures 4.13 and 4.14. The results show that the Richardson-Zaki law slightly underestimates fluidization velocity at lower solids concentrations whereas it slightly overestimates it at higher solids concentrations. The main reason for this deviation is an important assumption implicit in the Richardson-Zaki equation, i.e. that the flow is homogenous. The experimental results show that, for the range of concentrations tested, the flow is in the bubbly fluidization (inhomogeneous) regime and the assumption of homogenous flow is not valid.

Gevrin et al. (20) derived a simplified momentum balance equation for fluidized

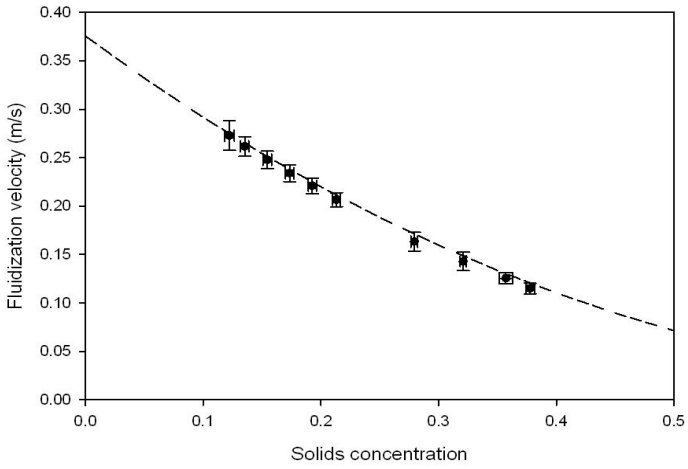

Figure 4.14: Fluidization velocity vs. solids concentration in the bed for 4 *mm* glass beads: Current experimental results (●); Richardson-Zaki equation with n = 2.4 (Dashed line)

beds:

$$(\frac{u_0}{u_t})^2 \frac{C_{D0}}{C_{Dt}} = (1 - C_s)^{4.7} \tag{4.11}$$

Here, C_{D0} and C_{Dt} are the drag coefficients at fluidization velocity and terminal settling velocity, respectively. They also used an Eulerian two-fluid formulation for dynamic simulation of a solid-liquid fluidized bed. Figure 4.15 shows a comparison between the Richardson-Zaki law (Equation 4.10), simplified balance model (Equation 4.11), simulations by Gevrin et al. (20) and experimental results from the present study for 3 *mm* glass beads. Note that the Richardson-Zaki equation and simplified balance model are indicating different particle terminal settling velocities (fluidization velocity at zero concentration) in Figure 4.15. The experimental terminal settling velocity is used in Richardson-Zaki equation while the Schiller-Nauman drag law was implemented in the simplified model (20). The results show that the simplified balance slightly overestimates the fluidization velocity, which could be the result of neglecting the nonlinear contribution of local fluctuations on solids concentration, slip velocity and pressure gradient.

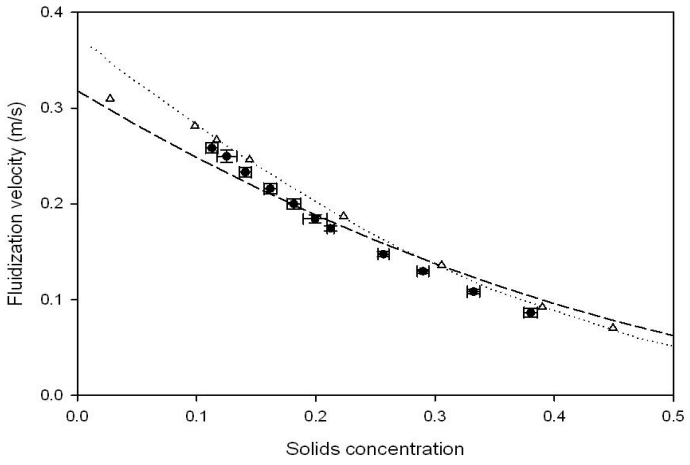

Figure 4.15: Fluidization velocity vs. solids concentration in the bed for 3 *mm* glass beads: Current experimental results (●); Richardson-Zaki equation with n = 2.4 (Dashed line); Gevrin et al. simulations (△); Simplified balance model (Dotted line).

Overall, there is relatively good agreement between the simulations and the experimental results.

4.5 Summary

Measurements of radial solids concentration and concentration fluctuations showed that solids volume fractions are usually lower in the center of the bed. This phenomenon is thought to correspond to the bubbling fluidization regime and the production of mushroom type structures in a liquid fluidized bed. The model of Foscolo and Gibilaro (82) was used to predict the flow regime transition in solid-liquid fluidized beds. The model predictions were in relatively good agreement with experimental observations.

Cross-sectional averaged solids concentrations versus fluidization velocity results were also compared against the Richardson-Zaki equation and the numerical study of Gevrin et al. (20). The comparison showed relatively good agreement between

experimental results, numerical predictions and Richardson-Zaki results.

Measurements of solids concentration fluctuations showed that the magnitude of the fluctuations were generally higher near the wall where particle-wall interactions are dominant. Such measurements are important for better understanding and modeling of local hydrodynamics and fluid-particle interactions. Cross-sectional averaged solids concentration fluctuations were compared to those obtained by Zenit and Hunt (44). Good agreement between the two data sets was observed.

5

Conclusions and Recommendations

5.1 General summary

The research presented in this dissertation focuses on the different aspects of turbulent, heterogeneous slurry flow modeling. The major contribution of this thesis is to advance, through reliable experimental investigation, the fundamental understanding of energy consumption, particle-particle interactions and fluid-particle interactions. Specifically, a modeling framework to optimize the energy consumption of slurry pipelines based on current phenomenological models was developed. Additionally, the basis for improving existing models and developing more advanced models through the measurement of solids concentration fluctuations and turbulent intensity distributions was provided. The analysis of these measurements provides valuable information about particle-particle and fluid-particle interactions in solid-liquid flows.

The second chapter dealt with energy consumption in slurry pipelines. The idea of Specific Energy Consumption (SEC), along with two different modeling schemes, was used to develop an energy consumption model for coarse particle slurries. For coarse particles smaller than 100 μm, but not so small as to cause significant non-Newtonian viscous effects, the equivalent-fluid model was used to determine the optimum operating conditions for a slurry pipeline. The model predictions were

also compared with a wide range of experimental data. The results showed that for slurries of this type, the equivalent-fluid model provides reasonable predictions of friction loss for solids concentrations less than 30% by volume. For slurries of this type, the minimum SEC occurs at a solids volume fraction of approximately 0.3. The exact value will depend on the particle size distribution and particle shape, through their effect on the slurry's maximum settled bed concentration, C_{max}.

For slurry flows with particle sizes greater than 150 μm, the near-wall lift model was used to calculate SEC and identify the optimum operating conditions. For these mixtures, the turbulence dispersion force does not fully maintain the particle suspension, resulting in asymmetric concentration profiles. The effect of particle size, pipe diameter, mixture velocity and solids concentration on the energy efficiency of horizontal slurry pipeline flows was evaluated. The analysis shows that at solids concentrations around 30% by volume, a minimum SEC is achieved, regardless of particle size or pipe diameter. However, the exact value of optimum SEC value increases with increasing particle diameter and decreases with increasing pipe diameter. The agreement between model predictions and experimental data verifies the utility of the model developed in this study.

In spite of the many advantages of the phenomenological models used to predict friction (pressure) loss and deposition velocity, there are many questions that these models are unable to answer. Examples include the flow in complex geometries such as pumps and hydrocyclones. The issue is that these models are designed to provide global (integral) parameters for certain geometries over specific operating conditions. For this reason, it is necessary to utilize computational models, but at this point in time, the accuracy of the existing models applicable to dense slurry flows, e.g. two fluid Eulerian-Eulerian models, is sometimes very poor. One of the major obstacles to better understand these complicated flows is the lack of reliable experimental data to evaluate the performance of existing modeling efforts. Despite the fact that there are many well-developed measurement techniques for dilute multiphase flow applications, one of the difficulties associated with experiments involving concentrated multiphase

flows is the lack of viable measurement techniques.

In the third chapter, an existing electrical tomography measurement technique was combined with advanced signal processing methods to develop a measurement procedure applicable to concentrated slurry flows. The procedure allowed for the measurement of two-dimensional solids concentration and velocity distributions, solids concentration fluctuations and solids turbulent intensity distributions at high solids concentrations and mixture velocities. Measurements were taken for the horizontal flow of a concentrated mixture of 100 μm sand and water in a 50 mm (diameter) pipeline loop. In general, the solids concentration fluctuations and solids axial turbulent intensities were found to be higher near the wall because of particle-wall collisions and because of the presence of the high shear zone near the wall. At constant solids concentrations, the magnitude of the concentration fluctuations increased with increasing mixture velocity.

Time-series power spectra of concentration- and velocity- fluctuations (averaged over the pipe cross section) were obtained using Fast Fourier Transform (FFT). This analysis showed that, for the 100 μm sand particles studied here, the rate of decay in solids fluctuations is closely related to the turbulent energy decay in the dissipation range for single–phase flow, suggesting that solids concentration fluctuations for this system are produced primarily through particle-fluid turbulence interactions. Comparison of the calculated turbulent length scale with the solids length scale (i.e. particle diameter) illustrated that, for these slurries, the particles interact with turbulent eddies in the dissipative range of the turbulent energy spectrum. Additionally, measurements of the local, time-averaged solids velocity distributions were used to calculate velocity defect profiles for these flows. The velocity defect profiles were very similar to those expected for single-phase turbulent flow (at the same flow conditions), particularly in the core of the flow.

The cross-sectional averaged concentration fluctuations were compared to experimental data previously reported for fluidized bed experiments and for gravity driven flows. The pipe flow results of the present study were consistent with the findings

previously reported: that is, that the magnitude of the concentration fluctuations increases with in situ concentration and should be expected to increase with increasing Stokes number. We have demonstrated that the solids concentration fluctuation results obtained for turbulent slurry pipeline flow can be compared to those collected using fluidized beds if an appropriate Stokes number is defined.

In Chapter 4, solids concentration and concentration fluctuations distributions in a solid-liquid fluidized bed were measured using the procedure developed for pipe flows and reported in Chapter 2. Glass bead particles with different sizes were fluidized in water. Previous experimental studies were limited to cross-sectional average values with no information on the solids concentrations and concentration fluctuation distributions within the flow domain. Such local information is important especially in determining the mechanism(s) responsible for producing solids fluctuations (e.g. particle-wall interactions). The measured radial solids concentration and concentration fluctuations showed that solids volume fractions are usually lower in the center of the bed. This phenomenon is thought to correspond to the bubbling fluidization regime and the production of mushroom type structures in a liquid fluidized bed. The Foscolo and Gibilaro (82) model was used to predict the flow regime transition in solid-liquid fluidized beds. The model predictions were in relatively good agreement with the experimental measurements.

Measurements of solids concentration fluctuations in the fluidized bed showed that the magnitude of the fluctuations was generally higher near the wall where particle-wall interactions are dominant. Cross-sectional averaged solids concentration fluctuations were compared to those obtained by Zenit and Hunt (44). Good agreement between the two data sets was observed. Cross-sectional averaged solids concentrations versus fluidization velocity results were also compared against the Richardson-Zaki equation and the numerical study of Gevrin et al. (20). The comparison showed relatively good agreement between experimental results, numerical simulations and the Richardson-Zaki equation.

5.2 Novel contributions

5.2.1 A measurement procedure to study concentrated solid-liquid flows

An experimental procedure was developed to study concentrated solid-liquid systems by combining the electrical impedance tomography technique and advanced signal processing methods. The combination was shown to provide accurate, high-frequency measurements in concentrated solid-liquid systems. This procedure is applicable to a wide range of vessel sizes without further complication, which makes it a unique way to study the scaling of solid-liquid flows from lab to pilot scale.

5.2.2 Instantaneous local measurements in concentrated solid-liquid flow

An important contribution to the field of fluid-particle dynamics was made through the experimental investigation of fluid-particle interactions in highly concentrated solid-liquid flows. These measurements, which are the first of their kind, revealed new information regarding the nature of fluid-particle interactions in solid-liquid flows. The local information allowed for the study of the contribution and importance of different mechanisms e.g. particle-wall interactions versus fluid-particle interactions. This is a significant improvement over previous studies, where the results were based on cross-sectional averaged information.

5.3 Uncertainties and challenges

There are some uncertainties associated with this study that need to be mentioned. First, the effect of the presence of the wall on the measurements must be accounted for, especially in the fluidized bed experiments where the difference between particle and vessel size was about one order of magnitude. This uncertainty can be addressed through additional experiments using different particle and vessel sizes.

The image reconstruction schemes chosen in the analysis of electrical tomogra-

phy measurements is another source of error in this study. The selection of a reconstruction scheme is a trade-off between spatial resolution and measurement speed. Although it is possible to obtain higher resolution results with more advanced reconstruction schemes, this requires huge amounts of post processing time. As the focus of this study was to develop the measurement procedure, a "fast" reconstruction scheme was used to analyze the data. The effect of the choice of the image reconstruction scheme can be addressed by implementing and developing new schemes and then evaluating the contribution of the error associated with each reconstruction scheme.

Finally, the uncertainty in liquid turbulent intensity distributions needs to be resolved and turbulent modulation must be considered. Currently, there is no turbulent modulation model applicable for highly concentrated mixtures. As a result, single-phase fluid turbulence was used as a basis for comparison in this research. The best possible way to overcome this challenge is to develop a measurement procedure to obtain measurements of fluid phase turbulent intensity in a concentrated solid-liquid mixture. Preliminary tests conducted as a part of the present study showed that adding salt solution as a tracer to the mixture could potentially be used to determine the fluid turbulent intensity using electrical tomography. However, creating a robust procedure will require a substantial experimental and signal processing investigation and a separate thesis project needs to be dedicated to this subject.

5.4 Recommendations for future work

Future fundamental research studies stemming from this project can be divided into short-term and long-term projects. In the short-term, the measurement procedure developed in this study could be used to study different particles having a wide range of Stokes number (i.e. particles with different densities and sizes). Experiments in fluidization columns and pipelines with larger diameters are also important to study and allow one to characterize the wall effect.

Image reconstruction schemes for electrical tomography is another interesting research topic. The resolution of electrical tomography mainly relies on one's choice of image reconstruction scheme. More advanced schemes will produce tomography data with higher resolution which reveals more detailed information about smaller scales.

As mentioned earlier, there is no reliable turbulent modulation model for highly concentrated solid-liquid mixtures. Measuring fluid turbulent intensity distributions is critical for developing a concrete modeling framework. A longer term research project can be devoted to the creation of measurement procedures to obtain fluid turbulent intensity data for flows containing high solids concentrations.

Bibliography

[1] Crowe C, Sommerfeld M, Tsuji Y. Multiphase flows with droplets and particles. CRC Press; 1998.

[2] Shook CA, Gillies RG, Sanders RS. Pipeline hydrotransport with applications in the oil sand industry. Saskatoon,SK, CA: SRC Publications; 2002.

[3] Wilson KC, Addie GR, Clift R. Slurry transport using centrifugal pumps. 3rd ed. New York: Springer; 2006.

[4] Durand R, Condolios E. The hydraulic transport of coal. proc. Colloq. on Hydraulic Transport of Coal, London, UK; 1954.

[5] Newitt DM, Richardson JF, Abbot M, Turtle RB. Hydraulic conveying of solids in horizontal pipes. Trans Inst of Chemi Engrs. 1955;33:93–113.

[6] Wilson KC. A unified physically based analysis of solid-liquid pipeline flow. Hydrotransport 4: BHR Group, Cranfield, UK; 1976. p. 1–12.

[7] Shook CA, Roco MA. Slurry flows: Principles and practice. Boston: Buttherworth-Heinemann; 1991.

[8] Gillies RG, Shook CA. Modelling high concentration settling slurry flows. Canadian Journal of Chemical Engineering. 2000;78(4):709–716.

[9] Gillies RG, Shook CA, Wilson KC. An improved two-layer model for horizontal slurry pipeline flows. Canadian Journal of Chemical Engineering. 1991;69:173–178.

[10] Gillies RG, , Shook CA. Concentration distribution of sand slurries in horizontal pipeflows. Particulate Science and Technology. 1994;12:45–69.

[11] Wilson KC, Sellgren A, Addie GR. Near-wall fluid lift of particles in slurry pipelines. 10th Int. Conf. on Transport and Sedimentation of Solids Particles,Worclaw, Poland; 2000. p. 435–444.

[12] Wilson KC, Sellgren A. Interaction of particles and near-wall lift in slurry pipelines. Journal of Hydraulic Engineering. 2003;129(1):73–76.

[13] Gillies RG, Shook CA, Xu J. Modelling heterogeneous slurry flows at high velocities. Canadian Journal of Chemical Engineering. 2004;82(5):1060 – 1065.

[14] Gillies DP. Particle contribution to kinematic friction in slurry pipeline flow. University of Alberta, M.Sc. Thesis; 2013.

[15] Bagnold R. Experiments on a gravity-free dispersion of large solids spheres in a Newtonian fluid under shear. Proc Roy Soc A. 1954;255:40–63.

[16] Shirolkar JS, Coimbra CFM, McQuay MQ. Fundamental aspects of modeling turbulent particle dispersion in dilute flows. Progress in Energy and Combustion Science. 1996;22(4):363–399.

[17] Sundaresan ATCS. Analysis of the flow in inhomogeneous particle beds using the spatially averaged two-fluid equations. International Journal of Multiphase Flow. 2006;32(1):106–131.

[18] Ishii M, Mishima K. Two-fluid model and hydrodynamic constitutive relations. Nuclear Engineering and Design. 1984;82(2-3):107–126.

[19] Zenit R, Hunt ML, Brennen CE. Collisional particle pressure measurements in solid-liquid flows. Journal of Fluid Mechanics. 1997;353:261–283.

[20] Gevrin F, Masbernat O, Simonin O. Granular pressure and particle velocity fluctuations prediction in liquid fluidized beds. Chemical Engineering Science. 2008;63(9):2450 – 2464.

[21] Jenkins JT, Savage SB. Theory for the rapid flow of identical, smooth, nearly elastic, spherical particles. Journal of Fluid Mechanics. 1983;130:187–202.

[22] Gidaspow G. Multiphase flow and fluidization. Academic Press; 1994.

[23] Huilin L, Yurong H, Gidaspow D. Hydrodynamic modelling of binary mixture in a gas bubbling fluidized bed using the kinetic theory of granular flow. Chemical Engineering Science. 2003;58(7):1197–1205.

[24] Krampa-Morlu FM, Bugg JD, Bergstorm DJ, Sanders RS. Frictional pressure drop calculations for liquid-solid vertical flows using the two-fluid model. Proc. 14th Annual Conf. Computational Fluid Dynamics Society of Canada, Kingston, CA; 2006.

[25] Sun X, Ishii M, Kelly JM. Modified two-fluid model for the two-group interfacial area transport equation. Annals of Nuclear Energy. 2003;30(16):1601–1622.

[26] Bradshaw P. Understanding and prediction of turbulent flow. International Journal of Heat and Fluid Flow. 1997;18(1):45–54.

[27] Hara T, Kato S. Numerical simulation of thermal plumes in free space using the standard k-epsilon model. Fire Safety Journal. 2004;39(2):105–129.

[28] Enwald H, Peirano E, Almstedt A. Eulerian two-phase flow theory applied to fluidization. International Journal of Multiphase Flow. 1996;22:21–66.

[29] Campbell CS. Granular material flows - An overview. Powder Technology. 2006;162(3):208–229.

[30] Lun CKK, Savage SB. The effects of an impact velocity dependent coefficient of restitution on stresses developed by sheared granular materials. Acta Mechanica. 1986;63(1-4):15–44.

[31] Wen CY, Yu YH. Mechanics of fluidization. Chem Eng Prog Symp Series. 1996;62:100–111.

[32] Graham L, Hamilton R, Rudman M. Coarse solids concentration profiles in laminar pipe flows. In: Proc. HYDROTRANSPORT 15. BHR Group; 2002. p. 149–158.

[33] Ding J, Lyczkowski RW, Sha WT, Altobelli SA, Fukushima E. Numerical analysis of liquid-solids suspension velocities and concentrations obtained by NMR imaging. Powder Technology. 1993;77(3):301–312.

[34] Nakagawa M, Altobelli SA, Caprihan A, Fukushima E, Jeong E. Non-invasive measurements of granular flows by magnetic resonance imaging. Experiments in Fluids. 1993;16(1):54–60.

[35] Williams RA, Beck MS. Process Tomography: Principles, Techniques and Application. Butterworth-Heinemann; 1995.

[36] Dyakowski T, Jeanmeure LFC, Jaworski AJ. Application of electrical tomography for gas-solids and liquid-solids flows- A review. Powder Technology. 2000;112:174–192.

[37] Pachowko AD, Wang M, Poole C, Rhodes D. The use of Electrical Resistance Tomography (ERT) to monitor flow patterns in horizontal slurry transport pipelines. Banff, AB, Canada; 2003.

[38] Zhu K, Madhusudana Rao S, Wang C, Sundaresan S. Electrical capacitance tomography measurements on vertical and inclined pneumatic conveying of granular solids. Chemical Engineering Science. 2003;58(18):4225–4245.

[39] Azzopardi BJ, Jackson K, Robinson JP, Kaji R, Byars M, Hunt A. Fluctuations in dense phase pneumatic conveying of pulverised coal measured using Electrical Capacitance Tomography. Chemical Engineering Science. 2008;63(9):2548 – 2558.

[40] Bolton GT, Hooper CW, Mann R, Stitt EH. Flow distribution and velocity measurement in a radial flow fixed bed reactor using electrical resistance tomography. Chemical Engineering Science. 2004;59(10):1989 – 1997.

[41] Fangary YS, Williams RA, Neil WA, Bond J, Faulks I. Application of Electrical Resistance Tomography to detect deposition in hydraulic conveying systems. Powder Technology. 1998;95(1):61 – 66.

[42] Azzi A, Azzopardi BJ, Abdulkareem NH, Hunt A. Study of fluidization using electrical capacitance tomography. 7th International Conference on Multiphase Flow; 2010.

[43] Pozo MD, Briens CL, Wild G. Particle-particle collisions in liquid-solid and gas-liquid-solid fluidized beds. Chemical Engineering Science. 1993;48(18):3313 – 3319.

[44] Zenit R, Hunt ML. Solid fraction fluctuations in solid-liquid flows. International Journal of Multiphase Flow. 2000;26(5):763–781.

[45] Schaan JJ. Pipeline flow of Newtonian fine particle slurries. University of Saskatchewan, M.Sc. thesis; 2001.

[46] Korving AC. High concentrated fine-sand slurry flow in pipelines: an experimental study. Hydrotransport 15: BHR Group, Cranfield, UK; 2002. p. 769–776.

[47] Wilson KC, Sanders RS, Gillies RG, Shook CA. Verification of the near-wall model for slurry flow. Powder Technology. 2010;197(3):247–253.

[48] Wilson KC, Sellgren A. Behaviour of intermediate-particle slurries in pipelines. Proc. HYDROTRANSPORT 18: BHR Group, Cranfield, UK; 2010. p. 117–128.

[49] Gibert R. Transport hydraulique er refoulement des mixtures en conduit. Annales des Ponts et Chausees. 1960;Mai-Juin 1960- Juil- Aout 1960.

[50] Wilson KC. Algorithm for coarse-particle transport in horizontal and inclined pipes. Int. Symp. on Hydraulic Transp. of Coal and other Minerals (ISHT88),Bhubaneswar, India: CSIR and Indian Institute of Metals; 1988. p. 103–126.

[51] Wilson KC, Nnadi FN. Behaviour of mobile beds at high shear stress. 22nd Int. Conf. on Coastal Eng.,Delft, Netherlands: CSIR and Indian Institute of Metals; 1988. p. 2536–2451.

[52] Shook CA, Daniel SM, Scott JA, Holgate JP. Flow of suspensions of solids in pipelines, Part 2: Two mechanisms of particle suspensions. Canadian Journal of Chemical Engineering. 1968;46:238–244.

[53] Kaushal DR, Tomita Y. Experimental investigation for near-wall lift of coarser particles in slurry pipeline using Gamma-ray densitometer. Powder Technology. 2007;172(3):177 – 187.

[54] Whitlock L, Wilson KC, Sellgren A. Effect of near wall lift on frictional characteristics of sand slurries. Proc. HYDROTRANSPORT 16: BHR Group, Cranfield, UK; 2004. p. 443–454.

[55] Kaushal DR, Sato K, Toyota T, Funatsu K, Tomita Y. Effect of particle size distribution on pressure drop and concentration profile in pipeline flow of highly concentrated slurry. International Journal of Multiphase Flow. 2005;31(7):809–823.

[56] Zenit R, Hunt ML. The impulsive motion of a liquid resulting from a particle collision. Journal of Fluid Mechanics. 1998;375:345–361.

[57] Buyevich YA, Kapbasov SK. Random fluctuation in a fluidized bed. Chemical Engineering Science. 1994;49(8):1229 – 1243.

[58] Zenit R, Hunt ML. Mechanics of immersed particle collisions. Journal of Fluids Engineering, Transactions of the ASME. 1999;121(1):179–184.

[59] Picciotto M, Marchioli C, Reeks MW, Soldati A. Statistics of velocity and preferential accumulation of micro-particles in boundary layer turbulence. Nuclear Engineering and Design. 2005;235(10-12):1239–1249.

[60] Kechroud N, Brahimi M, Djati A. Characterization of dynamic behaviour of continuous phase in liquid fluidized bed. Powder Technology. 2010;200:149–157.

[61] Didwania AK, Homsy GM. Flow regimes and flow transitions in liquid fluidized beds. International Journal of Multiphase Flow. 1981;7:593–580.

[62] Varaksin AY, Polyakov AF. Experimental study of fluctuations of particle velocity in turbulent flow of air in a pipe. High Temperature. 2000;38(5):764–770.

[63] Norman JT, Bonnecaze RT. Measurement of solids distribution in suspension flows using electrical resistance tomography. Canadian Journal of Chemical Engineering. 2005;83(1):24–36.

[64] Xu J, Wu Y, Wang M, Munir B, Oluwadarey HI, Schlaberg HI, et al. Measurement of solid slurry flow via correlation of Electromagnetic Flow Meter, electrical resistance tomography and mechanistic modelling. Journal of Hydrodynamics. 2009;21(4):557–563.

[65] Datta U, Dyakowski T, Mylvaganam S. Estimation of particulate velocity components in pneumatic transport using pixel based correlation with dual plane ECT. Chemical Engineering Journal. 2007;130(2-3):87 – 99.

[66] Walpole RE, Myers RH, Myers SL, Ye K. Probability and statistics for engineers and scientists. 8th ed. Upper Saddle River, NJ, USA: Pearson Prentice Hall; 2007.

[67] Sanders RS, Sun R, Gillies RG, McKibben MJ, Litzenberger C, Shook CA. Deposition velocities for particles of intermediate size in turbulent flow. Hydrotransport 16: BHR Group, Cranfield, UK; 2004. p. 429–442.

[68] Oppenheim AV, Schafer RW, Buck JR. Discrete-time signal processing. Upper Saddle River, NJ, USA: Prentice Hall; 1999.

[69] Press WA, Flannery BP, Teukolsky SA, Vetterling WA. Numerical recipes in C. Cambridge,UK: Cambridge University Press; 1988.

[70] Kulick JD, Fessler JR, Eaton JK. Particle response and turbulence modification in fully developed channel flow. Journal of Fluid Mechanics. 1994;277:109–134.

[71] Alajbegovic A, Assad A, Bonetto F, Lahey RTJ. Phase distribution and turbulence structure for solid/fluid upflow in a pipe. International Journal of Multiphase Flow. 1994;20(3):453 – 479.

[72] Truesdell GC, Elghobashi S. On the two-way interaction between homogeneous turbulence and dispersed solid particles. II. Particle dispersion. Physics of Fluids. 1994;6(3):1405–1407.

[73] Lightstone MF, Hodgson SM. Turbulence modulation in gas-particle flows: A comparison of selected models. Canadian Journal of Chemical Engineering. 2004;82(2):209–219.

[74] Thomas DG. Transport characteristics of suspension: VIII. A note on the viscosity of Newtonian suspensions of uniform spherical particles. Journal of Colloid Science. 1965;20(3):267–277.

[75] Pope SB. Turbulent flows. 5th ed. Cambridge,UK: Cambridge University Press; 2008.

[76] Hughmark GA. Turbulent properties in the core of pipe flow. Industrial and Engineering Chemistry Fundamentals. 1977;16:307–308.

[77] Longwell PA. Mechanics of fluid flows. New York: McGraw-Hill; 1966.

[78] Saffman PG. The lift on a small sphere in shear flow. Journal of Fluid Mechanics. 1965;22:385–400.

[79] Collins LR, Keswani A. Reynolds number scaling of particle clustering in turbulent aerosols. New Journal of Physics. 2004;6:119–135.

[80] Aguilar-Corona A, Zenit R, Masbernat O. Collisions in a liquid fluidized bed. International Journal of Multiphase Flow. 2011;37(7).

[81] Yang WC, editor. Handbook of fluidization and fluid-particle systems. 1st ed. Marcel Dekker, Inc.; 2003.

[82] Foscolo PU, Gibilaro LG. A fully predictive criterion for transition between particulate and aggregate fluidisation. Chemical Engineering Science. 1984;39:1667 – 1675.

[83] Batchelor GK. A new theory of the instability of a uniform fluidized bed. JFluid Mech. 1988;193 , 1988:75–110.

[84] Koch DL. Kinetic theory for a monodisperse gas-solid suspension. Physics of Fluids A. 1990;2(10):1711–1723.

[85] Gibilaro LG, Hossain I, Foscolo PU. Aggregate behaviour of liquid fluidized beds. Canadian Journal of Chemical Engineering. 1986;64(6):931–938.

[86] Patankar NA, Joseph DD. Modeling and numerical simulation of particulate flows by the Eulerian-Lagrangian approach. International Journal of Multiphase Flow. 2001;27(10):1659–1684.

[87] Wang M. Inverse solutions for electrical impedance tomography based on conjugate gradients methods. Measurement Science and Technology. 2002;13(1):101–117.

Appendix A

Horizontal pipe flow experimental procedure

The layout of SRC's 52 mm diameter pipeline ($L = 44m$), is shown in Figure 3.1 (p. 57). The loop contains a 2" x 3" AH Warman centrifugal pump with variable frequency motor control to adjust the flow rate. A straight, horizontal test section ($L = 4.88m, D = 53.1mm$), located where the flow is expected to be fully developed, was used for frictional pressure measurements using a Valydyne differential pressure transducer. Distance of the test section from the beginning of the long-radius bend and pump discharge are 27.2 and 5.1 m, respectively. of the A transparent observation section was inserted in the line to observe solids deposition. This pipeline flow loop has an internal volume of 90 L.

The loop is equipped with an electromagnetic flow meter to determine the mixture flow rate. A double pipe heat exchanger section utilizes glycol flowing countercurrent through the annulus to maintain the desired mixture temperature. The loop is also equipped with an Industrial Tomography System (ITS) Z8000 high speed Electrical Impedance Tomography (EIT) system and a dual-plane sensor to measure the instantaneous solids concentration and velocity maps.

Narrowly sized sand particles with $d_{50} = 100\mu m$ were used for the experiments. Subsamples of the solids were collected using a riffling device to acquire representative samples. These samples were used to determine the particle size distribution and the

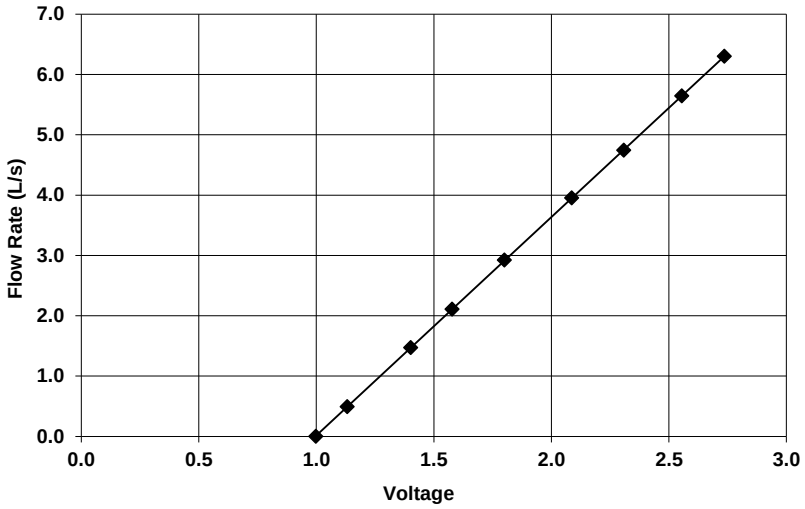

Figure A.1: Sample calibration curve for magnetic flow meter.

solids density. The procedure for density determination is to add a known volume of pure water to a known mass of dry solids to reach a set volume in an accurately calibrated volumetric flask (the mixture was de-aired by vacuum). The volume occupied by the solids could then be calculated to give an average solids density or specific gravity. Particle size distributions were conducted using a standard sieve analysis.

Magnetic flow meters and pressure transducers require calibration before installation in the loop. The magnetic flow meter was calibrated using city water and the bucket-and-stopwatch method. The mass of water that passed through the flow meter during a certain time was weighed to evaluate the actual flow rate. The voltage reading from the flow meter obtained at a given flow rate was recorded to find the calibration curve. Figure A.1 shows a sample calibration curve for the magnetic flow meter.

Pressure transducers were calibrated using a manometer and Meriam manometer fluid. The low pressure side of the transducer was left open to atmosphere while the high side was pressurized using high pressure air. The high side was also connected

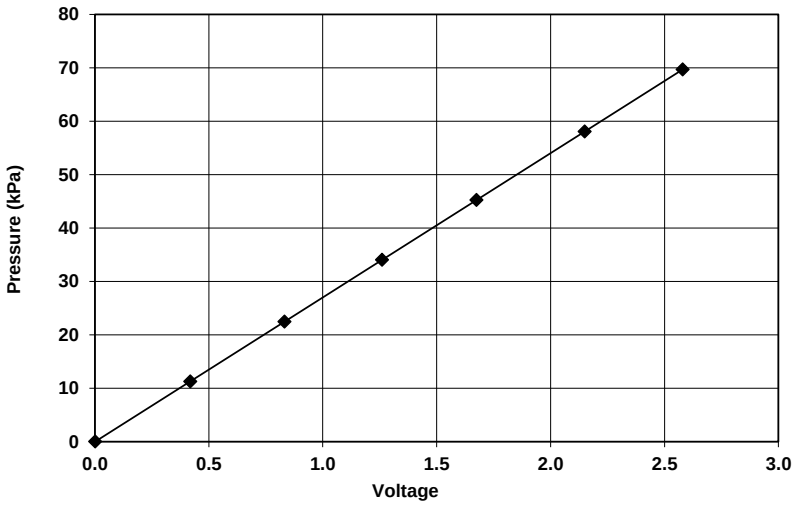

Figure A.2: Sample calibration curve for differential pressure transducers.

to the manometer where the actual pressure could be obtained from manometer readings. The transducers were calibrated in a way that a zero pressure difference correlated to zero voltage reading. The pressure difference was then increased to the next value and the pressure versus voltage measurement used to obtain calibration information for the transducers. A sample calibration curve for the pressure transducers is illustrated in Figure A.2.

After finishing the calibration and installing the measurement devices, the pipe loop was filled with hot tap water and circulated with the tank valve open to de-air the water. After complete de-airing, the system was allowed to cool down to the desired temperature and the EIT device was calibrated at different velocities using the de-aired water. In the next step, the pressure transducer lines were purged with high pressure de-aired water to remove any air bubbles from the lines. The presence of air bubbles can impact the pressure transducer readings significantly and increase the measurement error.

From pressure gradient versus velocity measurements for clear water at 20 °C, the effective roughness of the pipe wall was determined to be 10 μm in the test section.

A. Horizontal pipe flow experimental procedure

Desired solids concentrations were established by adding weighed quantities of sand. Solids were added to a water filled pipeline via the feed tank. Operating velocities were selected by setting the pump speed and monitoring the magnetic flow meter readings. At each solid concentration, EIT and pressure gradient measurements were taken at different mixture velocities. The mixture velocity in all experiments was kept above the deposition velocity to avoid the formation of a stationary bed in the pipe. Experiments were started at higher velocities and the mixture velocity decreased in a stepwise function until all required mixture velocities were covered.

To achieve the next higher concentration, a weighed amount of solids was added to the mixture to reach the desired concentration. All the previous measurement steps were again followed for the new solids concentration.

Appendix B

Fluidized bed experimental procedure

The experiments were performed in a 10.16 cm (i.d.) fluidized bed loop. A schematic layout of the the set up is shown in Figure 4.1(p. 91). The setup is equipped with a variable speed centrifugal pump to circulate the fluid at different velocities. The liquid velocity was measured using an orifice meter. The pressure drop across an orifice plate was measured using a Valydyne differential pressure transducer. A calming section was installed at the bottom of the bed to minimize the effect of upstream flow disturbance into the bed. Two sets of 500 micron screens were installed, one at the bottom and one at the top of the bed to hold the particles in the bed. An extra, coarser screen was also added to the bottom screen in order to support the weight of a packed bed of particles.

The apparatus was also equipped with an Industrial Tomography System (ITS) Z8000 Electrical Impedance Tomography (EIT) system along with a dual-plane sensor to measure the instantaneous solids concentration map within the bed.

Pressure transducers and the orifice meter were calibrated prior to installation in the column. The same method described in Appendix A was used to calibrate the pressure transducers. Figure B.1 shows an example of a calibration curve produced for pressure transducers on the fluidization rig.

The orifice meter was calibrated by running city water through the meter and

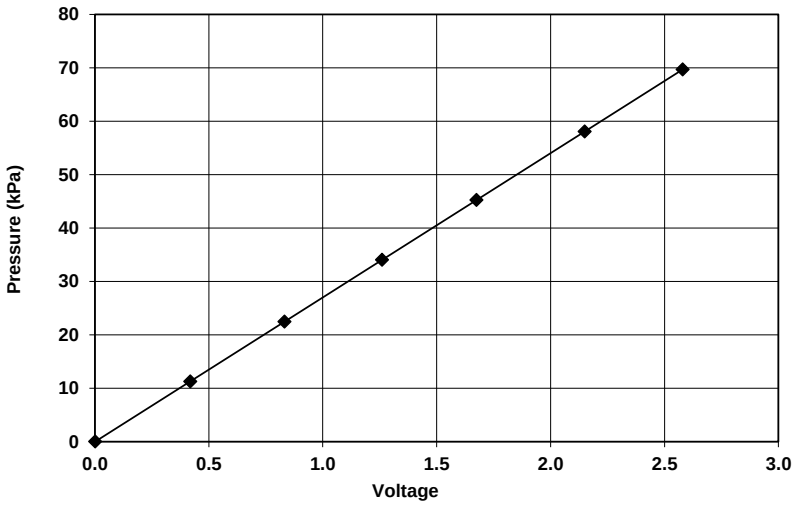

Figure B.1: Sample calibration curve for differential pressure transducers.

measuring the actual flow rate using the bucket-and-stopwatch method. The mass of water passing through the meter during a certain amount of time was weighed to evaluate the actual flow rate. The flow rate versus pressure drop measurements were used to determine the orifice discharge coefficient, which was found to be 0.65. The orifice discharge coefficient along with pressure drop measurement across the orifice was used to determine the flow rate and mixture velocity during the experiments. A sample orifice calibration curve is shown in Figure B.2.

Once the calibrated devices were installed in the setup, the system was filled with hot water and the fluid was circulated to de-air the carrier fluid by means of the air bleed valve at the top section of the setup. After de-airing, the EIT sensors were calibrated while operating at different fluid velocities. Knowing the solids density and column dimensions, the weight of solids needed to be added to system was calculated such that 10%, 25% and 40% of the bed volume could be occupied by particles. Solid particles then were added to the bed in three separate loadings from the solids addition port. As the addition of solids might introduce air into the system, the de-airing process was repeated.

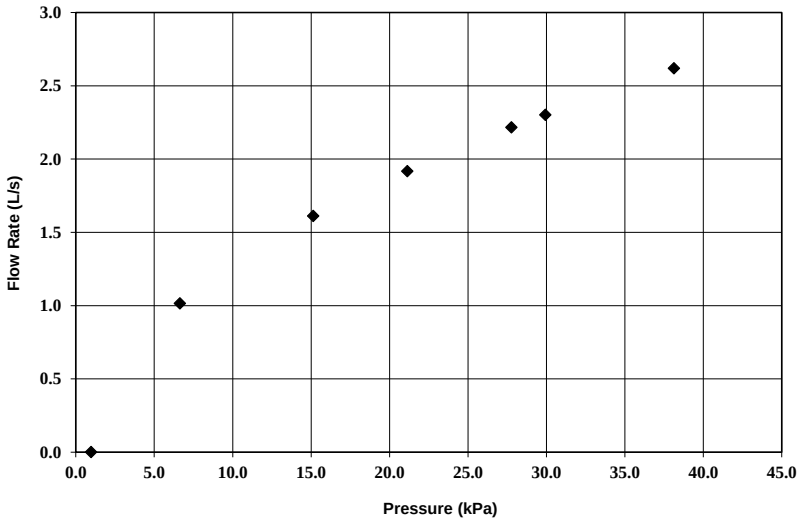

Figure B.2: Sample calibration curve for the orifice meter.

After each loading, experiments were carried out at different fluidization velocities. Different concentration distributions in the bed were achieved at each fluidization velocity and instantaneous solids concentration maps were obtained using the EIT. Flow rate and mixture velocity measurements obtained from the orifice meter were also monitored. The flow rate was kept at a constant velocity for 10 minutes to reach steady state conditions before any measurements were taken.

After finishing the experiments, the carrier fluid was drained using the drain valve and particles were recovered using the the access door located at the bottom section of the bed.

Appendix C

Measurement procedure: additional information

Electrical Impedance Tomography (EIT) was used to determine solids concentration and velocity distribution mesuremnts during this project. Information about the contents of a process vessel or pipe can be obtained using EIT equipment. In the sensor plane of the device, multiple electrodes are arranged around the boundary of the vessel at fixed location. These electrodes are in contact with the fluid but do not disturb the flow. The measurement procedure includes injecting a known electric current to two adjacent electrodes and measuring the resulting voltage from the all remaining pairs of neighbouring electrodes. The current is then applied to the next set of adjacent electrodes and the voltage measurements are repeated. The procedure continues until a full rotation of the electrical field is obtained. A schematic representation of the EIT principle is shown in Figure C.1 (36).

The next step is to construct an image using the boundary voltage measurements. The image reconstruction consists of dividing the vessel's cross section into pixels and obtaining the distribution of the specific electrical property (e.g. conductivity) of the materials in each pixels. The reconstruction grid used in the current study is shown in Figure 4.2 (p. 92). The choice of reconstruction algorithm is a function of process characteristics. The linear image reconstruction schemes such as Standard Back Projection (SBP) algorithm (36; 87) are simple, fast and have a

I= electrical current

V= potential difference

σ = Conductivity

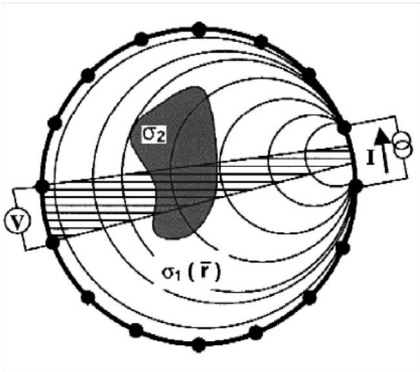

Figure C.1: Representation of EIT principle

high antinoise capability. However, they have limited accuracy where the difference between conductivity of two phase is high and in detecting phase boundaries. On the other hand, the iterative algorithms such as SCG (sensitivity theorem based inverse solution using conjugate gradient methods) (87) are more accurate in dealing with mixtures with high conductivity differences and for situations where detecting the boundary between two phases is required. However, they need to be used with care as they amplify the effect of process noise and their antinoise capability is not as high as with the linear algorithms. These methods are less useful in a process that exhibits a concentration gradient (87).

The concentration map can be obtained using the Maxwell equation (Equation 3.1) to convert the electrical conductivities obtained in each pixel to concentrations (36). Figure C.2 shows the solids concentration map and the radial profile obtained for a packed bed of 2 mm glass beads. The measurements showed a solids concentration of $C_s = 61.9\%$ which is close to the experimentally measured value of $C_s = 62.8\%$.

The effect of the selection of a specific image reconstruction scheme on the results is shown in Figures C.3 and C.4. Although both methods resulted in the same average concentration values, use of the SCG method shows more inhomogeneity in the radial

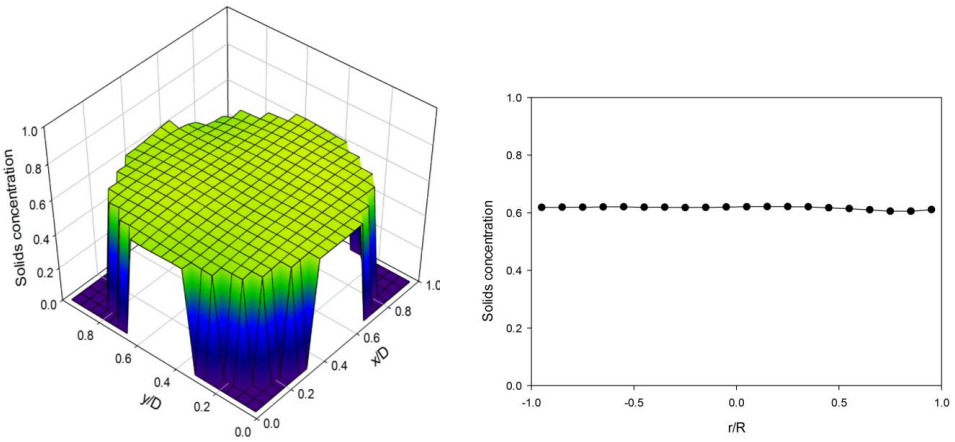

Figure C.2: Solids concentration map and radial profile for a packed bed of 2 mm glass beads

profile. There are two major factors which contribute to this effect. The first one is the inherent characteristic of SCG method to force a boundary between phases. Although this property is extremely useful in detecting boundaries in separated flows (such as stratified flow regime), it is not an advantage in dealing with dispersed flows. The second point is the iterative nature of the SCG scheme. The higher number of iterations will improve the quality of the results but the processing time will significantly increase. Figures C.3 and C.4 show the results after 5 iterations. The SBP reconstruction scheme has chosen to be the method of choice here due the flow regimes investigated in this study.

The EIT instrument was also used to measure the solids velocity distribution. This was achieved by combining dual-plane tomography measurements and a cross-correlation technique. The use of dual-plane tomography and cross-correlation is described in 3.2.2 (p. 60). Cross-correlation of the time signal of an individual pixel from first plane to its corresponding pixel in the second plane will give the solids velocity in that pixel. The velocity map is the product of performing pixel-to-pixel cross-correlation for all pixels in the flow domain. Figure C.5 shows a sample velocity

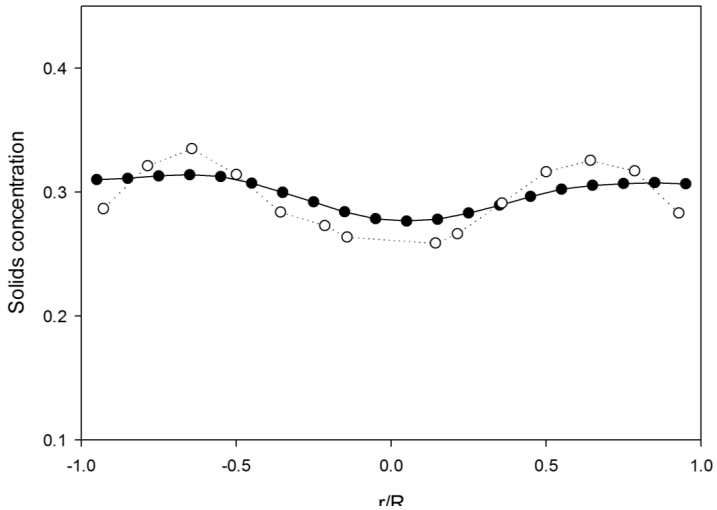

Figure C.3: Comparison of reconstructed solids concentration radial profile for a packed bed of 2 mm glass beads using SBP (●) and SCG (○) reconstruction schemes at $C_s = 30\%$

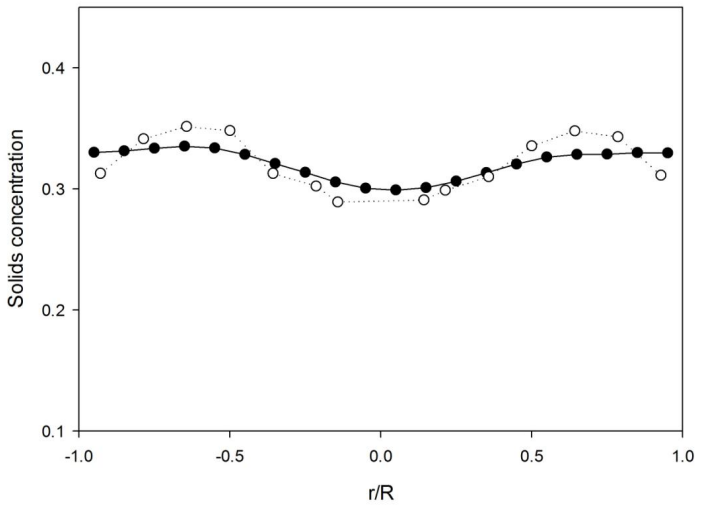

Figure C.4: Comparison of reconstructed solids concentration radial profile for a packed bed of 2 mm glass beads using SBP (●) and SCG (○) reconstruction schemes at $C_s = 32\%$

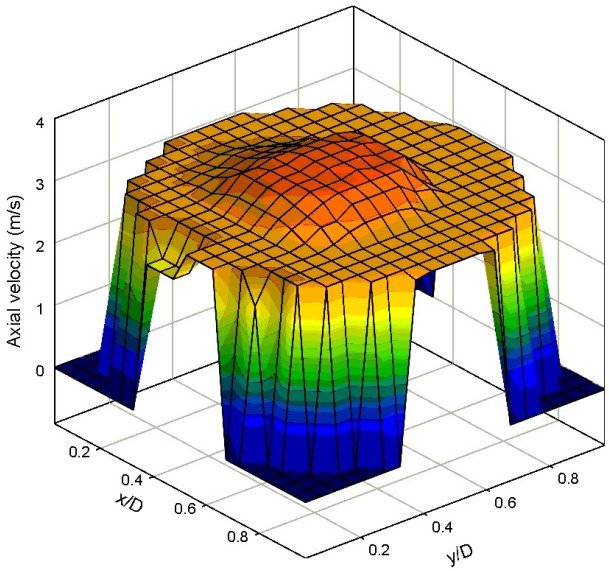

Figure C.5: Time averaged velocity map for 100 micron sand flowing in a 52 mm pipeline loop at $C_s = 30\%$ and V = 3 m/s

map obtained using this technique.

One of the important considerations in obtaining good velocity measurements using cross-correlation is the length of the signal. Using short signals for cross-correlation will result in non-physical velocities. The minimum signal length (L_{min}) required to obtain an accurate velocity varies for different types of signals. The cross-correlation was performed with signals of different lengths to investigate the effect of signal length on the velocity calculated using cross-correlation for the types of signals measured in the current study. Figure C.6 shows the effect of signal length on the cross-sectional averaged velocity for the flow of 100 μm sand in a 52 mm pipe at mixture velocity of 3 m/s. The result of this analysis showed that a signal consisting of at least 1000 data points is required for accurate velocity estimation.

The high speed concentration measurements can also be used to obtain solids instantaneous velocity and velocity fluctuations. The procedure for measuring instantaneous velocities is illustrated in Figure C.7 and consists of the following steps for each pixel:

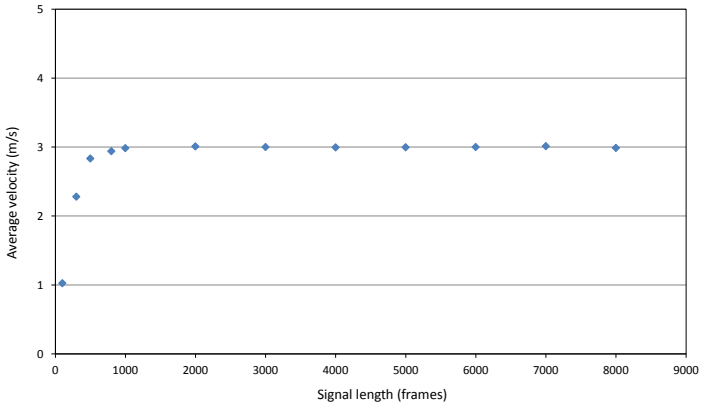

Figure C.6: Effect of signal length on velocity obtained using cross correlation for 100 micron sand flowing in a 52 mm pipeline loop at $C_s = 30\%$ and V = 3 m/s

1- Obtain the average velocity,$\bar{V_n}$, by cross-correlation of the entire signal

2- Select the first signal from 0 to L_{min} and calculate the first velocity, V_1, using the cross-correlation technique.

3- Determine the velocity time resolution (t_{vel}) and convert the time to number of frames (ΔN_f) using $\Delta N_f = \frac{t_{vel}}{M_s}$ where M_s is the measurement speed in frames per second.

4- Obtain the second velocity, V_2, by cross correlating the signal from ΔN_f to $L_{min} + \Delta N_f$.

5- Continue to calculate V_n, by cross-correlating the signal from $n\Delta N_f$ to $L_{min} + n\Delta N_f$.

6- Obtain the velocity fluctuation by subtracting the average velocity obtained in Step 1 using $\acute{V_n} = \bar{V_n} - V_n$

A sample velocity fluctuation map obtained using this procedure is shown in Figure C.8. The magnitude of the velocity fluctuations is a function of velocity time resolution. The effect of velocity time resolution on the magnitude of the velocity fluctuations is studied by obtaining the velocity fluctuations for a single data set at

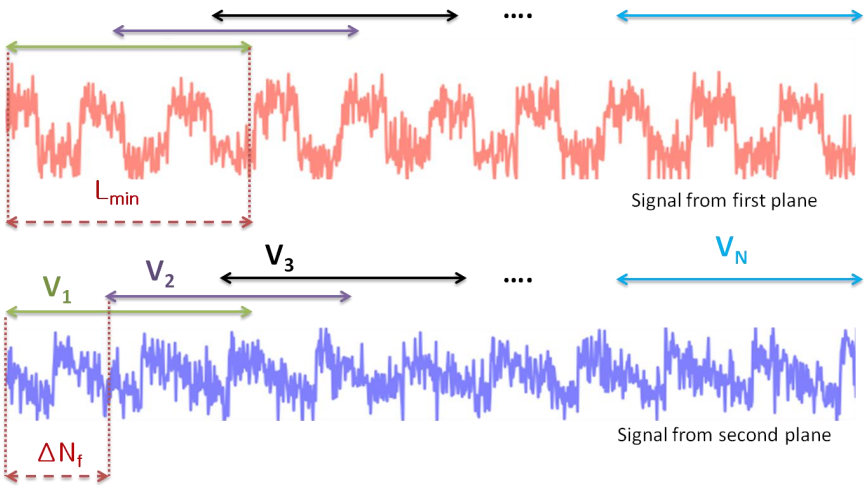

Figure C.7: The procedure for obtaining instantaneous velocity using cross-correlation

different time resolutions. The results of this analysis, which are illustrated in Figure C.9, show that time resolution equivalent of more than 10 frames, will change the velocity fluctuations. The profiles for time resolutions of 0.001, 0.007 and 0.012 s are basically the same with very minor deviations. As the time resolution increases, the magnitude of velocity fluctuations starts to change which is not favourable. As a result, the time resolution of 0.007 s, which is equivalent to 5 frames (based on measurement speed of 820 frames per second) was used to obtain instantaneous velocity and velocity fluctuations.

Time-series power spectra of velocity- fluctuations were obtained using the Welch method. In the Welch method, the averaged power spectra are estimated with data windowing (68). The Welch method reduces noise in the estimated power spectra in exchange for reducing the frequency resolution. The effect of velocity time resolution is investigated by obtaining the power spectrum for velocity fluctuation signal with different time resolution. Figure C.10 shows the effect of velocity time resolution on the power spectrum of the velocity fluctuations. As expected, the power spectrum

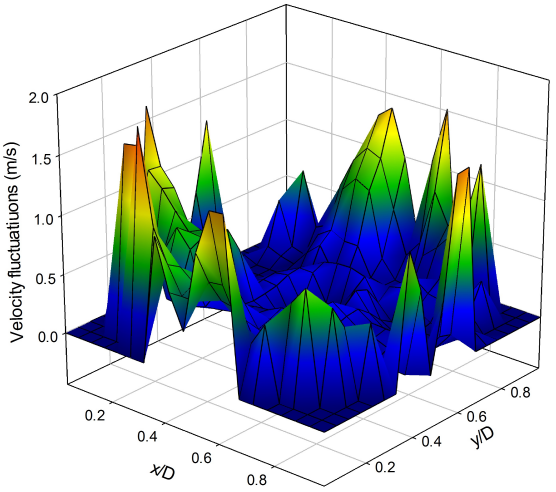

Figure C.8: Time averaged velocity fluctuation map for 100 micron sand flowing in a 52 mm pipeline loop at $C_s = 30\%$ and V = 3 m/s

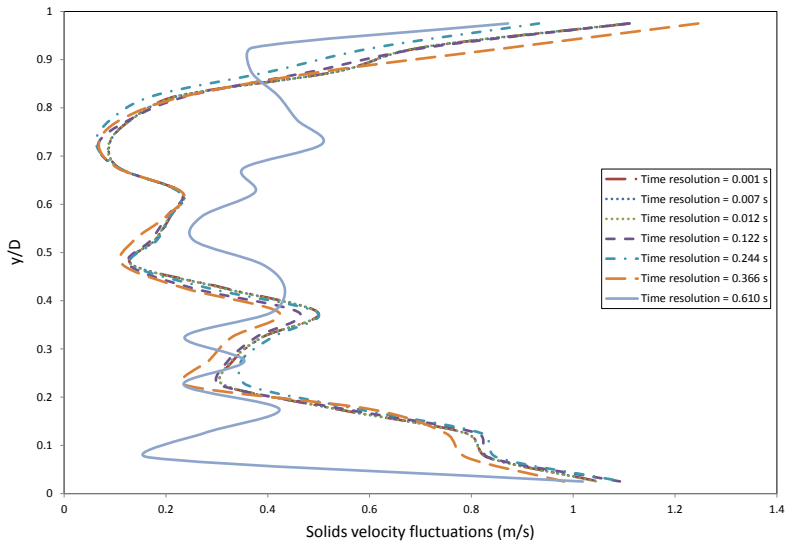

Figure C.9: Time averaged velocity fluctuation profiles for 100 micron sand flowing in a 52 mm pipeline loop at $C_s = 30\%$ and V = 3 m/s obtained using different time resolutions

shifted toward lower frequencies by increasing the time resolution. The results also indicate that the rate of energy decay is constant in all data sets except at very low frequencies.

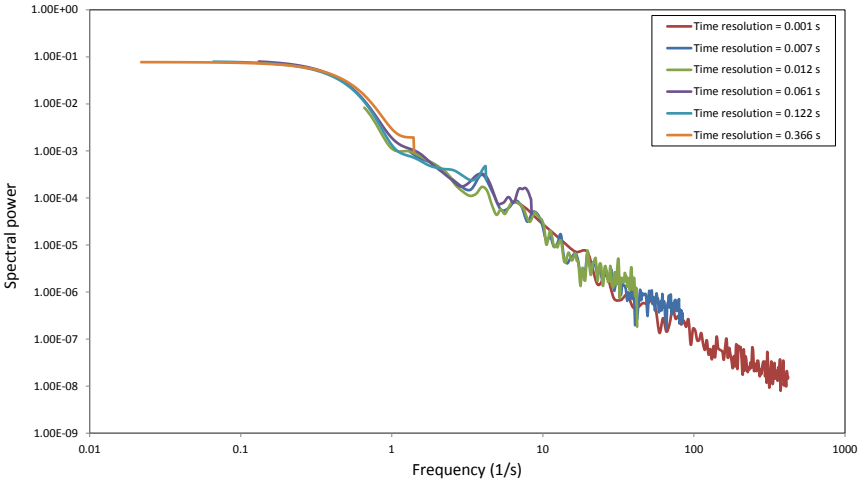

Figure C.10: Effect of velocity time resolution on the power spectrum of velocity fluctuations for 100 micron sand flowing in a 52 mm pipeline loop at C_s = 30% and V = 3 m/s

Appendix D

Matlab code

The code that was used to analyze the data is provided in this appendix. The code is programmed as a Graphical User Interface (GUI) for ease of data processing. The input comes from the dual-plane EIT measurements, which are exported in the comma-separated values (CSV) file format using ITS *Toolsuite* software. The output is based on the reconstruction grid shown in Figure 4.2 (p. 92). For each plane, an instantaneous concentration map for an individual frame is obtained directly from EIT measurements. The code then calculates the RMS concentration fluctuations map by finding the time-averaged concentration and deducting this value from instantaneous concentration in each pixel. The result is a solids concentration map and a solids concentration fluctuation map for each frame.

To obtain the velocity, pixel to pixel cross-correlation has been performed on the time series of instantaneous concentration values of two identical pixels in planes 1 and 2. The velocity fluctuation was obtained using the method described in Appendix C.

Time-average, cross-sectional average, chord-average and radial distribution data can be obtained from instantaneous velocity and concentration profiles whenever is required. The output is a *Micosoft Excel* file including all required parameters.

The important variables are described in the code as comments. Note that code is not optimized and further optimization is required to increase its speed and performance.

```
function varargout = simple_guibeta2(varargin)

gui_Singleton = 1;
gui_State = struct('gui_Name',       mfilename, ...
    'gui_Singleton',  gui_Singleton, ...
    'gui_OpeningFcn', @simple_guibeta2_OpeningFcn, ...
    'gui_OutputFcn',  @simple_guibeta2_OutputFcn, ...
    'gui_LayoutFcn',  [] , ...
    'gui_Callback',   []);
if nargin && ischar(varargin{1})
    gui_State.gui_Callback = str2func(varargin{1});
end

if nargout
    [varargout{1:nargout}] = gui_mainfcn(gui_State, varargin{:});
else
    gui_mainfcn(gui_State, varargin{:});
end

% --------------------------------------------------------------------
function Open_Callback(hObject, eventdata, handles)
s = '*.csv'
[file_name, mach_path] = uigetfile( ...
    {s, 'All CSV-Files (*.csv)'; }, ...
    'Select File',handles.filepath);

if isequal([file_name,mach_path],[0,0])
    return

  else
    File = fullfile(mach_path,file_name);
end
handles.File = File ;
handles.filepath = mach_path;
set( handles.Open_File, 'String', File );
guidata(hObject, handles);

function simple_guibeta2_OpeningFcn(hObject, eventdata, handles, varargin)

handles.output = hObject;
clc;
handles.filepath = 'c:\';
guidata(hObject, handles);

function varargout = simple_guibeta2_OutputFcn(hObject, eventdata, handles)

varargout{1} = handles.output;



function dropbar1_Callback(hObject, eventdata, handles)
```

```
choice = get(handles.dropbar1,'value');
axes(handles.axes2);

if choice == 1
    surf(handles.conc1);
    title('Solids concentration map');
    xlabel('x/D');
    ylabel ('y/D');
    zlabel ('Concentration (v/v)');
end

if choice == 2
    surf(handles.Cfluc_avg_profile1);
    title('Solids concentration fluctuations map');
    xlabel('x/D');
    ylabel ('y/D');
    zlabel ('Concentration fluctuations (v/v)');
end

if choice == 3
    surf(handles.Conc_fluc_intensity1);
    title('Solids concentration fluctuation  Intensity map 1');
    xlabel('x/D');
    ylabel ('y/D');
    zlabel ('concentration fluctuation intensity ');
end

if choice == 4
    plot(handles.conc_profilex1,handles.yd,'ro-');grid;
    title('Solids concnentration profile in x direction 1');
    xlabel('Concentration (v/v)');
    ylabel ('x/D');
end

if choice == 5
    plot(handles.conc_profiley1,handles.yd,'go-');grid
    title('Solids concnentration profile in y direction 1');
    xlabel('Concentration (v/v))');
    ylabel ('y/D');
end

if choice == 6
    plot(handles.Cfluc_avg_profilex1,handles.yd,'ro-');grid
    title('Solids concentration fluctuations profile in x direction 1');
    xlabel('Concentration fluctuations (v/v)');
    ylabel ('x/D');
end

if choice == 7
    plot(handles.Cfluc_avg_profiley1,handles.yd,'go-');grid
```

```
    title('Solids concentration fluctuations profile in y direction 1');
    xlabel('Concentration fluctuations (v/v)');
    ylabel ('y/D');
end

if choice == 8
    plot(handles.Conc_fluc_intensity_profilex1,handles.yd,'ro-');grid
    title('Concentration fluctuation intensity profile in x direction 1');
    xlabel('Fluctuation intensity');
    ylabel ('x/D');
end

if choice == 9
    plot(handles.Conc_fluc_intensity_profiley1,handles.yd,'go-');grid
    title('Concentration fluctuation intensity profile in y direction 1');
    xlabel('Fluctuation intensity');
    ylabel ('y/D');
end

if choice == 10
    surf(handles.conc2);
    title('Solids concentration map');
    xlabel('x/D');
    ylabel ('y/D');
    zlabel ('Concentration (v/v)');
end

if choice == 11
    surf(handles.Cfluc_avg_profile2);
    title('Solids concentration fluctuations map');
    xlabel('x/D');
    ylabel ('y/D');
    zlabel ('Concentration fluctuations (v/v)');
end

if choice == 12
    surf(handles.Conc_fluc_intensity2);
    title('Solids concentration fluctuation  Intensity map 1');
    xlabel('x/D');
    ylabel ('y/D');
    zlabel ('concentration fluctuation intensity ');
end

if choice == 13
    plot(handles.conc_profilex2,handles.yd,'ro-');grid;
    title('Solids concnentration profile in x direction 1');
    xlabel('Concentration (v/v)');
    ylabel ('x/D');
end

if choice == 14
```

```
    plot(handles.conc_profiley2,handles.yd,'go-');grid
    title('Solids concnentration profile in y direction 1');
    xlabel('Concentration (v/v))');
    ylabel ('y/D');
end

if choice == 15
    plot(handles.Cfluc_avg_profilex2,handles.yd,'ro-');grid
    title('Solids concentration fluctuations profile in x direction 1');
    xlabel('Concentration fluctuations (v/v)');
    ylabel ('x/D');
end

if choice == 16
    plot(handles.Cfluc_avg_profiley2,handles.yd,'go-');grid
    title('Solids concentration fluctuations profile in y direction 1');
    xlabel('Concentration fluctuations (v/v)');
    ylabel ('y/D');
end

if choice == 17
    plot(handles.Conc_fluc_intensity_profilex2,handles.yd,'ro-');grid
    title('Concentration fluctuation intensity profile in x direction 1');
    xlabel('Fluctuation intensity');
    ylabel ('x/D');
end

if choice == 18
    plot(handles.Conc_fluc_intensity_profiley2,handles.yd,'go-');grid
    title('Concentration fluctuation intensity profile in y direction 1');
    xlabel('Fluctuation intensity');
    ylabel ('y/D');
end

if choice == 19
    loglog(handles.pv1,handles.pp1);
    title('Cfluc periodogram 1');

end

if choice == 20
    loglog(handles.wv1,handles.wp1);
    title('Cfluc pwelch 1');

end

if choice == 21
    loglog(handles.pv2,handles.pp2);
    title('Cfluc periodogram 2');

end
```

```
if choice == 22
    loglog(handles.wv2,handles.wp2);
    title('Cfluc pwelch 2');

end

if choice == 23
    loglog(handles.spacial_average1);
    title('Spatial Average 1');

end

if choice == 24
    loglog(handles.spacial_average2);
    title('Spatial Average 2');

end

if choice == 25

    cut_frequency=handles.cutfreq;
    w=cut_frequency*2*9.7/8000;
    data=handles.spacial_average1';
    z=iddata(data,[],0.0012);
    zf=idfilt(z,4,w,'high');
    handles.Filtered_Cflucavg1=zf.outputdata;

    loglog(handles.Filtered_Cflucavg1);
    title('Filtered Spatial Average 1');

end

if choice == 26

    cut_frequency=handles.cutfreq;
    w=cut_frequency*2*9.7/8000;
    data=handles.spacial_average2';
    z=iddata(data,[],0.0012);
    zf=idfilt(z,4,w,'high');
    handles.Filtered_Cflucavg2=zf.outputdata;


    loglog(handles.Filtered_Cflucavg2);
    title('Filtered Spatial Average 2');
    end

if choice == 27
    surf(handles.vel);
    title('Solids velocity map');
    xlabel('x/D');
```

```
    ylabel ('y/D');
    zlabel ('Velocity (m/s)');

end

if choice == 28

    surf(handles.vel_fluc);
    title('Solids velocity fluctuations map');
    xlabel('x/D');
    ylabel ('y/D');
    zlabel ('Velocity fluctuations (m/s)');
end

if choice == 29

    surf(handles.turb_intens);
    title('Solids turbulent Intensity map');
    xlabel('x/D');
    ylabel ('y/D');
    zlabel ('Turbulent Intensity ');

end

if choice == 30

    plot(handles.vel_profilex,handles.yd,'ro-');grid
    title('Solids velocity profile in x direction');
    xlabel('Velocity (m/s)');
    ylabel ('x/D');

end

if choice == 31

    plot(handles.vel_profiley,handles.yd,'go-');grid;
    title('Solids velocity profile  in y direction');
    xlabel('Velocity (m/s)');
    ylabel ('y/D');

end

if choice == 32

    plot(handles.vel_fluc_profilex,handles.yd,'ro-');grid
    title('Solids velocity fluctuations profile in x direction');
    xlabel('Velocity fluctuations (m/s)');
    ylabel ('x/D');

end
```

```
if choice == 33

    plot(handles.vel_fluc_profiley,handles.yd,'go-');grid
    title('Solids velocity fluctuations profile in y direction');
    xlabel('Velocity fluctuations (m/s)');
    ylabel ('y/D');

end

if choice == 34

    plot(handles.turb_intens_profilex,handles.yd,'ro-');grid
    title('Solids tubulent intensity profile in x direction');
    xlabel('Turbulent intensity');
    ylabel ('x/D');

end

if choice == 35

    plot(handles.turb_intens_profiley,handles.yd,'go-');grid
    title('Solids tubulent intensity profile in y direction');
    xlabel('Turbulent intensity');
    ylabel ('y/D');

end

if choice == 36
    loglog(handles.vpf,handles.vpp);
    title('Velocity fluc periodogram');

end

if choice == 37
    loglog(handles.vwf,handles.vwp);
    title('Velocity fluc pwelch');

end
guidata(hObject, handles);

function dropbar1_CreateFcn(hObject, eventdata, handles)

if ispc && isequal(get(hObject,'BackgroundColor'),
    get(0,'defaultUicontrolBackgroundColor'))
    set(hObject,'BackgroundColor','white');
end
% --------------------------------------------------------------------
function File_Callback(hObject, eventdata, handles)
function Execute_Callback(hObject, eventdata, handles)

clc;
```

```
col = get(handles.Execute,'backg');
set(handles.Execute,'str','RUNNING...','backg',[1 .6 .6]);
pause(.01);
S= handles.File;
A = csvread(S,2,2);
[m,n]=size(A);
frames=m;%# of frames
t=1:m;
npixel=n/2;%# of pixels in
number_of_frames= str2num(get(handles.nofr,'string'));
Total_time= str2num(get(handles.tottime,'string'));
time_delay=Total_time/number_of_frames;
gap= str2num(get(handles.sensgap,'string'));
step1= str2num(get(handles.nofav,'string'));
initial1= str2num(get(handles.initial,'string'));
th= str2num(get(handles.velth,'string'));
nfftc = str2num(get(handles.nfftcb,'string'));
nfftv = str2num(get(handles.nfftvb,'string'));
m1=fix((m-initial1)/step1);
num1=m-initial1;
sfc = number_of_frames/Total_time;
sfv = sfc/step1;
%%%%%%%%%%%%%%% Memory allocation for differnt tables%%%%%%%%%%%%%%%%%%%%%%%%%%%%
conc1=zeros(20,20);
conc2=zeros(20,20);
conc_profilex1=zeros(1,20);
conc_profilex2=zeros(1,20);
conc_profiley1=zeros(1,20);
conc_profiley2=zeros(1,20);
Cavg1=zeros(1,npixel);
Cavg2=zeros(1,npixel);
Cfluc1=zeros(m,n);
Cfluc2=zeros(m,n);
Cfluc_avg1=zeros(1,npixel);
Cfluc_avg2=zeros(1,npixel);
Cfluc_intensity1=zeros(1,npixel);
Cfluc_intensity2=zeros(1,npixel);
Cfluc_avg_profile1=zeros(20,20);
Cfluc_avg_profile2=zeros(20,20);
Cfluc_avg_profilex1=zeros(1,20);
Cfluc_avg_profilex2=zeros(1,20);
Cfluc_avg_profiley1=zeros(1,20);
Cfluc_avg_profiley2=zeros(1,20);
Cflucavg1=zeros(1,m);
Cflucavg2=zeros(1,m);
Conc_fluc_intensity2=zeros(20,20);
Conc_fluc_intensity1=zeros(20,20);
Conc_fluc_intensity_profilex1=zeros(1,20);
Conc_fluc_intensity_profilex2=zeros(1,20);
Conc_fluc_intensity_profiley1=zeros(1,20);
Conc_fluc_intensity_profiley2=zeros(1,20);
```

```
D=zeros(npixel,m1);
D1=zeros(1,npixel);
Error_conc1=zeros(1,npixel);
Error_conc2=zeros(1,npixel);
Error1=zeros(1,npixel);
Error2=zeros(1,npixel);
Filtered_Cflucavg1=zeros(m,1);
Filtered_Cflucavg2=zeros(m,1);
I=zeros(npixel,m1);
I1=zeros(1,npixel);
M=zeros(npixel,m1);
M1=zeros(1,npixel);
Std_error1=zeros(20,20);
Std_error2=zeros(20,20);
Std_error_conc1=zeros(20,20);
Std_error_conc2=zeros(20,20);
Std_error_profilex1=zeros(1,20);
Std_error_profilex2=zeros(1,20);
Std_error_profiley1=zeros(1,20);
Std_error_profiley2=zeros(1,20);
Std_error_conc_profilex1=zeros(1,20);
Std_error_conc_profilex2=zeros(1,20);
Std_error_conc_profiley1=zeros(1,20);
Std_error_conc_profiley2=zeros(1,20);
tur_intensity=zeros(1,npixel);
turb_intens=zeros(20,20);
turb_intens_profilex=zeros(1,20);
turb_intens_profiley=zeros(1,20);
v=zeros(npixel,m1);
v_fluc=zeros(npixel,m1);
v_fluc_spatial_average=zeros(1,m1);
vel_fluc=zeros(20,20);
vel_fluc_profilex=zeros(1,20);
vel_fluc_profiley=zeros(1,20);
vel=zeros(20,20);
vel_profilex=zeros(1,20);
vel_profiley=zeros(1,20);
v1=zeros(1,npixel);
v_fluc_avg=zeros(1,npixel);
yd=zeros(1,20);
%%%%%%%%%%%%%%%%%%%%%%%%%%%%%%%%%%%%%%%%%%%%%%%%%%%%%%%%%%%%%%%%%%%%%%%%%%%%
for i=1:npixel;
    X=A(:,i);
    Y=A(:,i+npixel);
    %----------------------Concentration calculations--------------------
    c1=sum(X)/m;
    c2=sum(Y)/m;
    Error_conc1(i)=std(X)/sqrt(length(X));
    Error_conc2(i)=std(Y)/sqrt(length(Y));
    Cavg1(i)=c1;
    Cavg2(i)=c2;
```

```
for j=1:m;
    Cfluc1(j,i)=(X(j,1)-c1);
    Cfluc2(j,i)=(Y(j,1)-c2);
end
%%%%%%%%%%%%%%%%%%%%%%%%%%%%%%%%%%%%%%%%%%%%%%%%%%%%%%%%%%%%%%%%%%%%%%%%%%%%%%%
X1=Cfluc1(:,i);
X2=Cfluc2(:,i);
c1=(sum(X1.^2)/m)^0.5;
c2=(sum(X2.^2)/m)^0.5;
Error1(i)=1.96*std(X1)/sqrt(length(X1));
Error2(i)=1.96*std(X2)/sqrt(length(X2));
Cfluc_avg1(i)=c1;
Cfluc_avg2(i)=c2;
Cfluc_intensity1(i)=Cfluc_avg1(i)/ (Cavg1(i)+eps);
Cfluc_intensity2(i)=Cfluc_avg2(i)/ (Cavg2(i)+eps);
%----------------------Cross-correlation calculations ---------------------
X3= dtrend(X);
Y3= dtrend(Y);
X2=smooth(X3);
Y2=smooth(Y3);
XC1=xcorr(X2,Y2);
[k1,l1]=max(XC1);
M1(i)=k1;
I1(i)=l1;
D1(i)=m-I1(i);%# of frames delay between signals
v1(i)=gap/(D1(i)*time_delay);%velocity between two grid

s=step1-mod(num1,step1);
X=dtrend(X);
Y=dtrend(Y);
for j = 1 : s;
    X(m+j)=0;
    Y(m+j)=0;
end
for ii = 1:m1;
    plane1=X((ii-1)*step1+1: (ii-1)*step1+initial1+1);
    plane2=Y((ii-1)*step1+1: (ii-1)*step1+initial1+1);
    XC=xcorr(plane1,plane2);
    [k,l]=max(XC);
    M(i,ii)=k;
    I(i,ii)=l;
    D(i,ii)=initial1-I(i,ii);%# of frames delay between signals
    v(i,ii)=gap/(D(i,ii)*time_delay);%velocity between two grid
end
nn=length(v(i,:));
p=0;
c=0;
for jj = 1 :nn;
    if (v(i,jj) >= 0) & (v(i,jj) ~= Inf)& (v(i,jj) <= th) ;
        p=p+v(i,jj);
        c=c+1;
```

```
        else
            v(i,jj) = 0;
            p=p;
        end
    end
    v_fluc(i,:)= abs(v(i,:)-p/c*ones(1,nn));
    pp=0;
    cc=0;
    for kk = 1 :nn;
        if (v_fluc(i,kk) >= 0) & (v(i,kk) ~= Inf) & (v_fluc(i,kk) <= th);
            pp=pp+(v_fluc(i,kk))^2;
            cc=cc+1;
        else
            pp=pp;
        end
    end
    v_fluc_avg (i)=sqrt(1/cc *pp);
    tur_intensity(i)= v_fluc_avg (i)/(v1(i)+eps);

end

[dd, ee]=size (v_fluc);
for aa= 1:ee;
    v_fluc_spatial_average(aa)=sum(v_fluc(:,aa))/dd;
end
for i=1:m;
    X=Cfluc1(i,:);
    c1=sum(X)/n;
    Cflucavg1(i)=c1;
    X=Cfluc2(i,:);
    c1=sum(X)/n;
    Cflucavg2(i)=c1;
end
data=Cflucavg1;
[pp1,pv1]=periodogram(data,[],nfftc,sfc);
[wp1,wv1]=pwelch(data,[],[],nfftc,sfc);
data=Cflucavg2;
[pp2,pv2]=periodogram(data,[],nfftc,sfc);
[wp2,wv2]=pwelch(data,[],[],nfftc,sfc);

handles.cutfreq = str2num(get(handles.cutf,'string'));
cut_frequency = str2num(get(handles.cutf,'string'));
w=cut_frequency*2*9.7/8000;

data=Cflucavg1';
z=iddata(data,[],0.0012);
zf=idfilt(z,4,w,'high');
Filtered_Cflucavg1=zf.outputdata;

data=Cflucavg2';
z=iddata(data,[],0.0012);
```

```
zf=idfilt(z,4,w,'high');
Filtered_Cflucavg2=zf.outputdata;

datav=v_fluc_spatial_average;
size(datav)
[vpp,vpf]=periodogram(datav,[],nfftv,sfv);%sfv is velocity sampling frequency
[vwp,vwf]=pwelch(datav,[],[],nfftv,sfv)

for i=1:6;
    conc1(1,i+7)=Cavg1(i);
    Cfluc_avg_profile1(1,i+7)=Cfluc_avg1(i);
    Conc_fluc_intensity1(1,i+7)=Cfluc_intensity1(i);
    conc2(1,i+7)=Cavg2(i);
    Cfluc_avg_profile2(1,i+7)=Cfluc_avg2(i);
    Conc_fluc_intensity2(1,i+7)=Cfluc_intensity2(i);
    Std_error1(1,i+7)=Error1(i);
    Std_error2(1,i+7)=Error2(i);
    Std_error_conc1(1,i+7)=Error_conc1(i);
    Std_error_conc2(1,i+7)=Error_conc2(i);
    vel_fluc(1,i+7)=v_fluc_avg(i);
    turb_intens(1,i+7)=tur_intensity(i);
    vel(1,i+7)=v1(i);
end
for i=7:16;

    conc1(2,i-1)=Cavg1(i);
    Cfluc_avg_profile1(2,i-1)=Cfluc_avg1(i);
    Conc_fluc_intensity1(2,i-1)=Cfluc_intensity1(i);
    conc2(2,i-1)=Cavg2(i);
    Cfluc_avg_profile2(2,i-1)=Cfluc_avg2(i);
    Conc_fluc_intensity2(2,i-1)=Cfluc_intensity2(i);
    Std_error1(2,i-1)=Error1(i);
    Std_error2(2,i-1)=Error2(i);
    Std_error_conc1(2,i-1)=Error_conc1(i);
    Std_error_conc2(2,i-1)=Error_conc2(i);
    vel_fluc(2,i-1)=v_fluc_avg(i);
    turb_intens(2,i-1)=tur_intensity(i);
    vel(2,i-1)=v1(i);
end
for i=17:30;

    conc1(3,i-13)=Cavg1(i);
    Cfluc_avg_profile1(3,i-13)=Cfluc_avg1(i);
    Conc_fluc_intensity1(3,i-13)=Cfluc_intensity1(i);
    conc2(3,i-13)=Cavg2(i);
    Cfluc_avg_profile2(3,i-13)=Cfluc_avg2(i);
    Conc_fluc_intensity2(3,i-13)=Cfluc_intensity2(i);
    Std_error1(3,i-13)=Error1(i);
    Std_error2(3,i-13)=Error2(i);
    Std_error_conc1(3,i-13)=Error_conc1(i);
    Std_error_conc2(3,i-13)=Error_conc2(i);
```

```
    vel_fluc(3,i-13)=v_fluc_avg(i);
    turb_intens(3,i-13)=tur_intensity(i);
    vel(3,i-13)=v1(i);
end
for i=31:46;

    conc1(4,i-28)=Cavg1(i);
    Cfluc_avg_profile1(4,i-28)=Cfluc_avg1(i);
    Conc_fluc_intensity1(4,i-28)=Cfluc_intensity1(i);
    conc2(4,i-28)=Cavg2(i);
    Cfluc_avg_profile2(4,i-28)=Cfluc_avg2(i);
    Conc_fluc_intensity2(4,i-28)=Cfluc_intensity2(i);
    Std_error1(4,i-28)=Error1(i);
    Std_error2(4,i-28)=Error2(i);
    Std_error_conc1(4,i-28)=Error_conc1(i);
    Std_error_conc2(4,i-28)=Error_conc2(i);
    vel_fluc(4,i-28)=v_fluc_avg(i);
    turb_intens(4,i-28)=tur_intensity(i);
    vel(4,i-28)=v1(i);
end
for i=47:62;

    conc1(5,i-44)=Cavg1(i);
    Cfluc_avg_profile1(5,i-44)=Cfluc_avg1(i);
    Conc_fluc_intensity1(5,i-44)=Cfluc_intensity1(i);
    conc2(5,i-44)=Cavg2(i);
    Cfluc_avg_profile2(5,i-44)=Cfluc_avg2(i);
    Conc_fluc_intensity2(5,i-44)=Cfluc_intensity2(i);
    Std_error1(5,i-44)=Error1(i);
    Std_error2(5,i-44)=Error2(i);
    Std_error_conc1(5,i-44)=Error_conc1(i);
    Std_error_conc2(5,i-44)=Error_conc2(i);
    vel_fluc(5,i-44)=v_fluc_avg(i);
    turb_intens(5,i-44)=tur_intensity(i);
    vel(5,i-44)=v1(i);
end
for i=63:80;

    conc1(6,i-61)=Cavg1(i);
    Cfluc_avg_profile1(6,i-61)=Cfluc_avg1(i);
    Conc_fluc_intensity1(6,i-61)=Cfluc_intensity1(i);
    conc2(6,i-61)=Cavg2(i);
    Cfluc_avg_profile2(6,i-61)=Cfluc_avg2(i);
    Conc_fluc_intensity2(6,i-61)=Cfluc_intensity2(i);
    Std_error1(6,i-61)=Error1(i);
    Std_error2(6,i-61)=Error2(i);
    Std_error_conc1(6,i-61)=Error_conc1(i);
    Std_error_conc2(6,i-61)=Error_conc2(i);
    vel_fluc(6,i-61)=v_fluc_avg(i);
    turb_intens(6,i-61)=tur_intensity(i);
    vel(6,i-61)=v1(i);
```

```
end
for i=81:98;

    conc1(7,i-79)=Cavg1(i);
    Cfluc_avg_profile1(7,i-79)=Cfluc_avg1(i);
    Conc_fluc_intensity1(7,i-79)=Cfluc_intensity1(i);
    conc2(7,i-79)=Cavg2(i);
    Cfluc_avg_profile2(7,i-79)=Cfluc_avg2(i);
    Conc_fluc_intensity2(7,i-79)=Cfluc_intensity2(i);
    Std_error1(7,i-79)=Error1(i);
    Std_error2(7,i-79)=Error2(i);
    Std_error_conc1(7,i-79)=Error_conc1(i);
    Std_error_conc2(7,i-79)=Error_conc2(i);
    vel_fluc(7,i-79)=v_fluc_avg(i);
    turb_intens(7,i-79)=tur_intensity(i);
    vel(7,i-79)=v1(i);
end
for i=99:118;

    conc1(8,i-98)=Cavg1(i);
    Cfluc_avg_profile1(8,i-98)=Cfluc_avg1(i);
    Conc_fluc_intensity1(8,i-98)=Cfluc_intensity1(i);
    conc2(8,i-98)=Cavg2(i);
    Cfluc_avg_profile2(8,i-98)=Cfluc_avg2(i);
    Conc_fluc_intensity2(8,i-98)=Cfluc_intensity2(i);
    Std_error1(8,i-98)=Error1(i);
    Std_error2(8,i-98)=Error2(i);
    Std_error_conc1(8,i-98)=Error_conc1(i);
    Std_error_conc2(8,i-98)=Error_conc2(i);
    vel_fluc(8,i-98)=v_fluc_avg(i);
    turb_intens(8,i-98)=tur_intensity(i);
    vel(8,i-98)=v1(i);
end
for i=119:138;

    conc1(9,i-118)=Cavg1(i);
    Cfluc_avg_profile1(9,i-118)=Cfluc_avg1(i);
    Conc_fluc_intensity1(9,i-118)=Cfluc_intensity1(i);
    conc2(9,i-118)=Cavg2(i);
    Cfluc_avg_profile2(9,i-118)=Cfluc_avg2(i);
    Conc_fluc_intensity2(9,i-118)=Cfluc_intensity2(i);
    Std_error1(9,i-118)=Error1(i);
    Std_error2(9,i-118)=Error2(i);
    Std_error_conc1(9,i-118)=Error_conc1(i);
    Std_error_conc2(9,i-118)=Error_conc2(i);
    vel_fluc(9,i-118)=v_fluc_avg(i);
    turb_intens(9,i-118)=tur_intensity(i);
    vel(9,i-118)=v1(i);
end
for i=139:158;
```

```
    conc1(10,i-138)=Cavg1(i);
    Cfluc_avg_profile1(10,i-138)=Cfluc_avg1(i);
    Conc_fluc_intensity1(10,i-138)=Cfluc_intensity1(i);
    conc2(10,i-138)=Cavg2(i);
    Cfluc_avg_profile2(10,i-138)=Cfluc_avg2(i);
    Conc_fluc_intensity2(10,i-138)=Cfluc_intensity2(i);
    Std_error1(10,i-138)=Error1(i);
    Std_error2(10,i-138)=Error2(i);
    Std_error_conc1(10,i-138)=Error_conc1(i);
    Std_error_conc2(10,i-138)=Error_conc2(i);
    vel_fluc(10,i-138)=v_fluc_avg(i);
    turb_intens(10,i-138)=tur_intensity(i);
    vel(10,i-138)=v1(i);
end
for i= 159:178;

    conc1(11,i-158)=Cavg1(i);
    Cfluc_avg_profile1(11,i-158)=Cfluc_avg1(i);
    Conc_fluc_intensity1(11,i-158)=Cfluc_intensity1(i);
    conc2(11,i-158)=Cavg2(i);
    Cfluc_avg_profile2(11,i-158)=Cfluc_avg2(i);
    Conc_fluc_intensity2(11,i-158)=Cfluc_intensity2(i);
    Std_error1(11,i-158)=Error1(i);
    Std_error2(11,i-158)=Error2(i);
    Std_error_conc1(11,i-158)=Error_conc1(i);
    Std_error_conc2(11,i-158)=Error_conc2(i);
    vel_fluc(11,i-158)=v_fluc_avg(i);
    turb_intens(11,i-158)=tur_intensity(i);
    vel(11,i-158)=v1(i);
end
for i=179:198;

    conc1(12,i-178)=Cavg1(i);
    Cfluc_avg_profile1(12,i-178)=Cfluc_avg1(i);
    Conc_fluc_intensity1(12,i-178)=Cfluc_intensity1(i);
    conc2(12,i-178)=Cavg2(i);
    Cfluc_avg_profile2(12,i-178)=Cfluc_avg2(i);
    Conc_fluc_intensity2(12,i-178)=Cfluc_intensity2(i);
    Std_error1(12,i-178)=Error1(i);
    Std_error2(12,i-178)=Error2(i);
    Std_error_conc1(12,i-178)=Error_conc1(i);
    Std_error_conc2(12,i-178)=Error_conc2(i);
    vel_fluc(12,i-178)=v_fluc_avg(i);
    turb_intens(12,i-178)=tur_intensity(i);
    vel(12,i-178)=v1(i);
end
for i=199:218;

    conc1(13,i-198)=Cavg1(i);
    Cfluc_avg_profile1(13,i-198)=Cfluc_avg1(i);
    Conc_fluc_intensity1(13,i-198)=Cfluc_intensity1(i);
```

```
    conc2(13,i-198)=Cavg2(i);
    Cfluc_avg_profile2(13,i-198)=Cfluc_avg2(i);
    Conc_fluc_intensity2(13,i-198)=Cfluc_intensity2(i);
    Std_error1(13,i-198)=Error1(i);
    Std_error2(13,i-198)=Error2(i);
    Std_error_conc1(13,i-198)=Error_conc1(i);
    Std_error_conc2(13,i-198)=Error_conc2(i);
    vel_fluc(13,i-198)=v_fluc_avg(i);
    turb_intens(13,i-198)=tur_intensity(i);
    vel(13,i-198)=v1(i);
end
for i=219:236;

    conc1(14,i-217)=Cavg1(i);
    Cfluc_avg_profile1(14,i-217)=Cfluc_avg1(i);
    Conc_fluc_intensity1(14,i-217)=Cfluc_intensity1(i);
    conc2(14,i-217)=Cavg2(i);
    Cfluc_avg_profile2(14,i-217)=Cfluc_avg2(i);
    Conc_fluc_intensity2(14,i-217)=Cfluc_intensity2(i);
    Std_error1(14,i-217)=Error1(i);
    Std_error2(14,i-217)=Error2(i);
    Std_error_conc1(14,i-217)=Error_conc1(i);
    Std_error_conc2(14,i-217)=Error_conc2(i);
    vel_fluc(14,i-217)=v_fluc_avg(i);
    turb_intens(14,i-217)=tur_intensity(i);
    vel(14,i-217)=v1(i);

end
for i=237:254;

    conc1(15,i-235)=Cavg1(i);
    Cfluc_avg_profile1(15,i-235)=Cfluc_avg1(i);
    Conc_fluc_intensity1(15,i-235)=Cfluc_intensity1(i);
    conc2(15,i-235)=Cavg2(i);
    Cfluc_avg_profile2(15,i-235)=Cfluc_avg2(i);
    Conc_fluc_intensity2(15,i-235)=Cfluc_intensity2(i);
    Std_error1(15,i-235)=Error1(i);
    Std_error2(15,i-235)=Error2(i);
    Std_error_conc1(15,i-235)=Error_conc1(i);
    Std_error_conc2(15,i-235)=Error_conc2(i);
    vel_fluc(15,i-235)=v_fluc_avg(i);
    turb_intens(15,i-235)=tur_intensity(i);
    vel(15,i-235)=v1(i);
end
for i=255:270;

    conc1(16,i-252)=Cavg1(i);
    Cfluc_avg_profile1(16,i-252)=Cfluc_avg1(i);
    Conc_fluc_intensity1(16,i-252)=Cfluc_intensity1(i);
    conc2(16,i-252)=Cavg2(i);
    Cfluc_avg_profile2(16,i-252)=Cfluc_avg2(i);
```

```
    Conc_fluc_intensity2(16,i-252)=Cfluc_intensity2(i);
    Std_error1(16,i-252)=Error1(i);
    Std_error2(16,i-252)=Error2(i);
    Std_error_conc1(16,i-252)=Error_conc1(i);
    Std_error_conc2(16,i-252)=Error_conc2(i);
    vel_fluc(16,i-252)=v_fluc_avg(i);
    turb_intens(16,i-252)=tur_intensity(i);
    vel(16,i-252)=v1(i);
end
for i= 271:286;

    conc1(17,i-268)=Cavg1(i);
    Cfluc_avg_profile1(17,i-268)=Cfluc_avg1(i);
    Conc_fluc_intensity1(17,i-268)=Cfluc_intensity1(i);
    conc2(17,i-268)=Cavg2(i);
    Cfluc_avg_profile2(17,i-268)=Cfluc_avg2(i);
    Conc_fluc_intensity2(17,i-268)=Cfluc_intensity2(i);
    Std_error1(17,i-268)=Error1(i);
    Std_error2(17,i-268)=Error2(i);
    Std_error_conc1(17,i-268)=Error_conc1(i);
    Std_error_conc2(17,i-268)=Error_conc2(i);
    vel_fluc(17,i-268)=v_fluc_avg(i);
    turb_intens(17,i-268)=tur_intensity(i);
    vel(17,i-268)=v1(i);
end
for i=287:300;

    conc1(18,i-283)=Cavg1(i);
    Cfluc_avg_profile1(18,i-283)=Cfluc_avg1(i);
    Conc_fluc_intensity1(18,i-283)=Cfluc_intensity1(i);
    conc2(18,i-283)=Cavg2(i);
    Cfluc_avg_profile2(18,i-283)=Cfluc_avg2(i);
    Conc_fluc_intensity2(18,i-283)=Cfluc_intensity2(i);
    Std_error1(18,i-283)=Error1(i);
    Std_error2(18,i-283)=Error2(i);
    Std_error_conc1(18,i-283)=Error_conc1(i);
    Std_error_conc2(18,i-283)=Error_conc2(i);
    vel_fluc(18,i-283)=v_fluc_avg(i);
    turb_intens(18,i-283)=tur_intensity(i);
    vel(18,i-283)=v1(i);
end
for i= 301:310;

    conc1(19,i-295)=Cavg1(i);
    Cfluc_avg_profile1(19,i-295)=Cfluc_avg1(i);
    Conc_fluc_intensity1(19,i-295)=Cfluc_intensity1(i);
    conc2(19,i-295)=Cavg2(i);
    Cfluc_avg_profile2(19,i-295)=Cfluc_avg2(i);
    Conc_fluc_intensity2(19,i-295)=Cfluc_intensity2(i);
    Std_error1(19,i-295)=Error1(i);
    Std_error2(19,i-295)=Error2(i);
```

```
    Std_error_conc1(19,i-295)=Error_conc1(i);
    Std_error_conc2(19,i-295)=Error_conc2(i);
    vel_fluc(19,i-295)=v_fluc_avg(i);
    turb_intens(19,i-295)=tur_intensity(i);
    vel(19,i-295)=v1(i);
end
for i=311:316;

    conc1(20,i-303)=Cavg1(i);
    Cfluc_avg_profile1(20,i-303)=Cfluc_avg1(i);
    Conc_fluc_intensity1(20,i-303)=Cfluc_intensity1(i);
    conc2(20,i-303)=Cavg2(i);
    Cfluc_avg_profile2(20,i-303)=Cfluc_avg2(i);
    Conc_fluc_intensity2(20,i-303)=Cfluc_intensity2(i);
    Std_error1(20,i-303)=Error1(i);
    Std_error2(20,i-303)=Error2(i);
    Std_error_conc1(20,i-303)=Error_conc1(i);
    Std_error_conc2(20,i-303)=Error_conc2(i);
    vel_fluc(20,i-303)=v_fluc_avg(i);
    turb_intens(20,i-303)=tur_intensity(i);
    vel(20,i-303)=v1(i);
end

%%%%%%%%%%%%%%%%%x and y profiles calculations%%%%%%%%%%%%%%

for iii = 1 : 20
    yd (iii)= .025+(iii-1)*0.05;
    %--------Concentration profiles Plane 1------------------
    a7=~((conc1(:,iii)==0) | (conc1(:,iii)==Inf));
    b7= (conc1(:,iii));
    b7(isnan(b7))=0;
    b7(isinf(b7))=0;
    conc_profilex1(iii) =  sum (b7)/(sum(a7)+eps);

    a8=~((conc1(iii,:)==0) | (conc1(iii,:)==Inf));
    b8= (conc1(iii,:));
    b8(isnan(b8))=0;
    b8(isinf(b8))=0;
    conc_profiley1(iii) =  sum (b8)/(sum(a8)+eps);
    %-------Concentration fluctuation profiles Plane 1--------
    a9=~((Cfluc_avg_profile1(:,iii)==0) | (Cfluc_avg_profile1(:,iii)==Inf));
    b9= (Cfluc_avg_profile1(:,iii));
    b9(isnan(b9))=0;
    b9(isinf(b9))=0;
    Cfluc_avg_profilex1(iii) =  sum (b9)/(sum(a9)+eps);

    a10=~((Cfluc_avg_profile1(iii,:)==0) | (Cfluc_avg_profile1(iii,:)==Inf));
    b10= (Cfluc_avg_profile1(iii,:));
    b10(isnan(b10))=0;
    b10(isinf(b10))=0;
    Cfluc_avg_profiley1(iii) =  sum (b10)/(sum(a10)+eps);
```

```
%------Concentration fluctuation intensity Plane 1-------
a11=~((Conc_fluc_intensity1(:,iii)==0) | (Conc_fluc_intensity1(:,iii)==Inf));
b11= (Conc_fluc_intensity1(:,iii));
b11(isnan(b11))=0;
b11(isinf(b11))=0;
Conc_fluc_intensity_profilex1(iii) =  sum (b11)/(sum(a11)+eps);

a12=~((Conc_fluc_intensity1(iii,:)==0) | (Conc_fluc_intensity1(iii,:)==Inf));
b12= (Conc_fluc_intensity1(iii,:));
b12(isnan(b12))=0;
b12(isinf(b12))=0;
Conc_fluc_intensity_profiley1(iii) =  sum (b12)/(sum(a12+eps));
%----Concentration fluctuations Standard error profiles Plane 1-------
a13=~((Std_error1(:,iii)==0) | (Std_error1(:,iii)==Inf));
b13= (Std_error1(:,iii));
b13(isnan(b13))=0;
b13(isinf(b13))=0;
Std_error_profilex1(iii) =  sum (b13)/(sum(a13)+eps);

a14=~((Std_error1(iii,:)==0) | (Std_error1(iii,:)==Inf));
b14= (Std_error1(iii,:));
b14(isnan(b14))=0;
b14(isinf(b14))=0;
Std_error_profiley1(iii) =  sum (b14)/(sum(a14)+eps);
%-----Concentration  Standard error profiles Plane 1--------------------
a15=~((Std_error_conc1(:,iii)==0) | (Std_error_conc1(:,iii)==Inf));
b15= (Std_error_conc1(:,iii));
b15(isnan(b15))=0;
b15(isinf(b15))=0;
Std_error_conc_profilex1(iii) =  sum (b15)/(sum(a15)+eps);

a16=~((Std_error_conc1(iii,:)==0) | (Std_error_conc1(iii,:)==Inf));
b16= (Std_error_conc1(iii,:));
b16(isnan(b16))=0;
b16(isinf(b16))=0;
Std_error_conc_profiley1(iii) =  sum (b16)/(sum(a16)+eps);
%------Concentration profiles Plane 2---------------------------------
a7=~((conc2(:,iii)==0) | (conc2(:,iii)==Inf));
b7= (conc2(:,iii));
b7(isnan(b7))=0;
b7(isinf(b7))=0;
conc_profilex2(iii) =  sum (b7)/(sum(a7)+eps);


a8=~((conc2(iii,:)==0) | (conc2(iii,:)==Inf));
b8= (conc2(iii,:));
b8(isnan(b8))=0;
b8(isinf(b8))=0;
conc_profiley2(iii) =  sum (b8)/(sum(a8)+eps);
%----Concentration fluctuation profiles Plane 2-----------------------
a9=~((Cfluc_avg_profile2(:,iii)==0) | (Cfluc_avg_profile2(:,iii)==Inf));
```

```
    b9= (Cfluc_avg_profile2(:,iii));
    b9(isnan(b9))=0;
    b9(isinf(b9))=0;
    Cfluc_avg_profilex2(iii) =  sum (b9)/(sum(a9)+eps);

    a10=~((Cfluc_avg_profile2(iii,:)==0) | (Cfluc_avg_profile2(iii,:)==Inf));
    b10= (Cfluc_avg_profile2(iii,:));
    b10(isnan(b10))=0;
    b10(isinf(b10))=0;
    Cfluc_avg_profiley2(iii) =  sum (b10)/(sum(a10)+eps);
    %---Concentration fluctuation intensity Plane 2-------------------------
    a11=~((Conc_fluc_intensity2(:,iii)==0) | (Conc_fluc_intensity2(:,iii)==Inf));
    b11= (Conc_fluc_intensity2(:,iii));
    b11(isnan(b11))=0;
    b11(isinf(b11))=0;
    Conc_fluc_intensity_profilex2(iii) =  sum (b11)/(sum(a11)+eps);

    a12=~((Conc_fluc_intensity2(iii,:)==0) | (Conc_fluc_intensity2(iii,:)==Inf));
    b12= (Conc_fluc_intensity2(iii,:));
    b12(isnan(b12))=0;
    b12(isinf(b12))=0;
    Conc_fluc_intensity_profiley2(iii) =  sum (b12)/(sum(a12)+eps);
    %-----Concentration fluctuations Standard error profiles Plane 2---------
    a13=~((Std_error2(:,iii)==0) | (Std_error2(:,iii)==Inf));
    b13= (Std_error2(:,iii));
    b13(isnan(b13))=0;
    b13(isinf(b13))=0;
    Std_error_profilex2(iii) =  sum (b13)/(sum(a13)+eps);

    a14=~((Std_error2(iii,:)==0) | (Std_error2(iii,:)==Inf));
    b14= (Std_error2(iii,:));
    b14(isnan(b14))=0;
    b14(isinf(b14))=0;
    Std_error_profiley2(iii) =  sum (b14)/(sum(a14)+eps);
    %------Concentration  Standard error profiles Plane 2-------------
    a15=~((Std_error_conc2(:,iii)==0) | (Std_error_conc2(:,iii)==Inf));
    b15= (Std_error_conc2(:,iii));
    b15(isnan(b15))=0;
    b15(isinf(b15))=0;
    Std_error_conc_profilex2(iii) =  sum (b15)/(sum(a15)+eps);

    a16=~((Std_error_conc2(iii,:)==0) | (Std_error_conc2(iii,:)==Inf));
    b16= (Std_error_conc1(iii,:));
    b16(isnan(b16))=0;
    b16(isinf(b16))=0;
    Std_error_conc_profiley2(iii) =  sum (b16)/(sum(a16)+eps);
end
```

```
%%%%%%%x and y profiles calculations%%%%%%%%%%%%%%%%%%%%%%%%%%%%%

for iii = 1 : 20
    yd (iii)= .025+(iii-1)*0.05;
    %------velocity fluctuation profiles-----------------------------
    a1=~((vel_fluc(:,iii)==0) | (vel_fluc(:,iii)==Inf));
    b1= (vel_fluc(:,iii));
    b1(isnan(b1))=0;
    b1(isinf(b1))=0;
    vel_fluc_profilex(iii) =  sum (b1)/(sum(a1)+eps);

    a2=~((vel_fluc(iii,:)==0) |(vel_fluc(iii,:)==Inf));
    b2= (vel_fluc(iii,:));
    b2(isnan(b2))=0;
    b2(isinf(b2))=0;
    vel_fluc_profiley(iii) =  sum (b2)/(sum(a2)+eps);
    %-------velocity profiles-----------------------------------
    a3=~((vel(:,iii)==0) | (vel(:,iii)==Inf));
    b3= (vel(:,iii));
    b3(isnan(b3))=0;
    b3(isinf(b3))=0;
    vel_profilex(iii) =  sum (b3)/(sum(a3)+eps);

    a4=~((vel(iii,:)==0) | (vel(iii,:)==Inf));
    b4= (vel(iii,:));
    b4(isnan(b4))=0;
    b4(isinf(b4))=0;
    vel_profiley(iii) =  sum (b4)/(sum(a4+eps));
    %------Turbulent intensity profiles-------------------------
    a5=~((turb_intens(:,iii)==0) | (turb_intens(:,iii)==Inf));
    b5=(turb_intens(:,iii));
    b5(isnan(b5))=0;
    b5(isinf(b5))=0;
    turb_intens_profilex(iii) =  sum (b5)/(sum (a5)+eps);

    a6=~((turb_intens(iii,:)==0) | (turb_intens(iii,:)==Inf));
    b6=(turb_intens(iii,:));
    b6(isnan(b6))=0;
    b6(isinf(b6))=0;
    turb_intens_profiley(iii) =  sum (b6)/(sum(a6)+eps);
    %-------Concentration profiles Plane 1--------------------
    a7=~((conc1(:,iii)==0) | (conc1(:,iii)==Inf));
    b7= (conc1(:,iii));
    b7(isnan(b7))=0;
    b7(isinf(b7))=0;
    conc_profilex1(iii) =  sum (b7)/(sum(a7)+eps);

    a8=~((conc1(iii,:)==0) | (conc1(iii,:)==Inf));
    b8= (conc1(iii,:));
    b8(isnan(b8))=0;
    b8(isinf(b8))=0;
```

```
conc_profiley1(iii) =  sum (b8)/(sum(a8)+eps);
%-----Concentration fluctuation profiles Plane 1----------
a9=~((Cfluc_avg_profile1(:,iii)==0) | (Cfluc_avg_profile1(:,iii)==Inf));
b9= (Cfluc_avg_profile1(:,iii));
b9(isnan(b9))=0;
b9(isinf(b9))=0;
Cfluc_avg_profilex1(iii) =  sum (b9)/(sum(a9)+eps);

a10=~((Cfluc_avg_profile1(iii,:)==0) | (Cfluc_avg_profile1(iii,:)==Inf));
b10= (Cfluc_avg_profile1(iii,:));
b10(isnan(b10))=0;
b10(isinf(b10))=0;
Cfluc_avg_profiley1(iii) =  sum (b10)/(sum(a10)+eps);
%------Concentration fluctuation intensity Plane 1-------------
a11=~((Conc_fluc_intensity1(:,iii)==0) | (Conc_fluc_intensity1(:,iii)==Inf));
b11= (Conc_fluc_intensity1(:,iii));
b11(isnan(b11))=0;
b11(isinf(b11))=0;
Conc_fluc_intensity_profilex1(iii) =  sum (b11)/(sum(a11)+eps);

a12=~((Conc_fluc_intensity1(iii,:)==0) | (Conc_fluc_intensity1(iii,:)==Inf));
b12= (Conc_fluc_intensity1(iii,:));
b12(isnan(b12))=0;
b12(isinf(b12))=0;
Conc_fluc_intensity_profiley1(iii) =  sum (b12)/(sum(a12+eps));
%-----Concentration profiles Plane 2-----------------------------
a7=~((conc2(:,iii)==0) | (conc2(:,iii)==Inf));
b7= (conc2(:,iii));
b7(isnan(b7))=0;
b7(isinf(b7))=0;
conc_profilex2(iii) =  sum (b7)/(sum(a7)+eps);

a8=~((conc2(iii,:)==0) | (conc2(iii,:)==Inf));
b8= (conc2(iii,:));
b8(isnan(b8))=0;
b8(isinf(b8))=0;
conc_profiley2(iii) =  sum (b8)/(sum(a8)+eps);
%-----Concentration fluctuation profiles Plane 2-------------------------
a9=~((Cfluc_avg_profile2(:,iii)==0) | (Cfluc_avg_profile2(:,iii)==Inf));
b9= (Cfluc_avg_profile2(:,iii));
b9(isnan(b9))=0;
b9(isinf(b9))=0;
Cfluc_avg_profilex2(iii) =  sum (b9)/(sum(a9)+eps);

a10=~((Cfluc_avg_profile2(iii,:)==0) | (Cfluc_avg_profile2(iii,:)==Inf));
b10= (Cfluc_avg_profile2(iii,:));
b10(isnan(b10))=0;
b10(isinf(b10))=0;
Cfluc_avg_profiley2(iii) =  sum (b10)/(sum(a10)+eps);
%-----Concentration fluctuation intensity Plane 2-----------------------------
a11=~((Conc_fluc_intensity2(:,iii)==0) | (Conc_fluc_intensity2(:,iii)==Inf));
```

```
    b11= (Conc_fluc_intensity2(:,iii));
    b11(isnan(b11))=0;
    b11(isinf(b11))=0;
    Conc_fluc_intensity_profilex2(iii) =  sum (b11)/(sum(a11)+eps);

    a12=~((Conc_fluc_intensity2(iii,:)==0) | (Conc_fluc_intensity2(iii,:)==Inf));
    b12= (Conc_fluc_intensity2(iii,:));
    b12(isnan(b12))=0;
    b12(isinf(b12))=0;
    Conc_fluc_intensity_profiley2(iii) =  sum (b12)/(sum(a12)+eps);
end

set(handles.Execute,'str','Run','backg',col)



handles.vel = vel;
handles.vel_fluc = vel_fluc;
handles.turb_intens = turb_intens;
handles.vel_profilex = vel_profilex;
handles.vel_profiley = vel_profiley;
handles.vel_fluc_profilex = vel_fluc_profilex;
handles.vel_fluc_profiley = vel_fluc_profiley;
handles.turb_intens_profilex = turb_intens_profilex;
handles.turb_intens_profiley = turb_intens_profiley;
handles.conc1 = conc1;
handles.Cfluc_avg_profile1 = Cfluc_avg_profile1;
handles.Conc_fluc_intensity1 = Conc_fluc_intensity1;
handles.conc_profilex1 = conc_profilex1;
handles.conc_profiley1 = conc_profiley1;
handles.Cfluc_avg_profilex1 = Cfluc_avg_profilex1;
handles.Cfluc_avg_profiley1 = Cfluc_avg_profiley1;
handles.Conc_fluc_intensity_profilex1 = Conc_fluc_intensity_profilex1;
handles.Conc_fluc_intensity_profiley1 = Conc_fluc_intensity_profiley1;
handles.pp1 = pp1;
handles.pv1 = pv1;
handles.wp1 = wp1;
handles.wv1 = wv1;
handles.spacial_average1 = Cflucavg1;
handles.Filtered_Cflucavg1 = Filtered_Cflucavg1;
handles.conc2 = conc2;
handles.Cfluc_avg_profile2 = Cfluc_avg_profile2;
handles.Conc_fluc_intensity2 = Conc_fluc_intensity2;
handles.conc_profilex2 = conc_profilex2;
handles.conc_profiley2 = conc_profiley2;
handles.Cfluc_avg_profilex2 = Cfluc_avg_profilex2;
handles.Cfluc_avg_profiley2 = Cfluc_avg_profiley2;
handles.Conc_fluc_intensity_profilex2 = Conc_fluc_intensity_profilex2;
handles.Conc_fluc_intensity_profiley2 = Conc_fluc_intensity_profiley2;
handles.pp2 = pp2;
```

```
handles.pv2 = pv2;
handles.wp2 = wp2;
handles.wv2 = wv2;
handles.yd = yd;
handles.spacial_average2 = Cflucavg2;
handles.Filtered_Cflucavg2 = Filtered_Cflucavg2;
handles.vpp = vpp;
handles.vpf = vpf;
handles.vwp = vwp;
handles.vwf = vwf;

axes(handles.axes2)

surf(handles.conc1);
title('Solids concentration map');
xlabel('x/D');
ylabel ('y/D');
zlabel ('Concentration (v/v)');

axes(handles.axes3)

surf(handles.vel);
title('Solids velocity map');
xlabel('x/D');
ylabel ('y/D');
zlabel ('Velocity (m/s)');

axes(handles.axes4)

plot(handles.conc_profilex1,handles.yd,'ro-');grid;
title('Solids concnentration profile in x direction 1');
xlabel('Concentration (v/v)');
ylabel ('x/D');

axes(handles.axes5)

plot(handles.vel_profilex,handles.yd,'ro-');grid
title('Solids velocity profile in x direction');
xlabel('Velocity (m/s)');
ylabel ('x/D');

guidata(hObject, handles);


% --------------------------------------------------------------------
function saveas_Callback(hObject, eventdata, handles)
S2 = strcat(handles.File,'analysed_result.xls');

xlswrite(S2,handles.vel,'Velocity Map');
xlswrite(S2,handles.vel_fluc,'Velocity Fluctuation');
xlswrite(S2,handles.turb_intens,'Turbulant Intensity Map');
```

```
xlswrite(S2,handles.vel_profilex','Velocity profile x');
xlswrite(S2,handles.vel_profiley','Velocity profile y');
xlswrite(S2,handles.vel_fluc_profilex','Velocity profile fluc x');
xlswrite(S2,handles.vel_fluc_profiley','Velocity profile fluc y');
xlswrite(S2,handles.turb_intens_profilex','Turb Intens profile x');
xlswrite(S2,handles.turb_intens_profiley','Turb Intens profile y');
xlswrite(S2,handles.conc1,'Concentration map P1');
xlswrite(S2,handles.Cfluc_avg_profile1','Conc Fluc avg profile P1');
xlswrite(S2,handles.Conc_fluc_intensity1','Conc Fluc Intensity P1');
xlswrite(S2,handles.conc_profilex1','Conc profile x P1');
xlswrite(S2,handles.conc_profiley1','Conc profile y P1');
xlswrite(S2,handles.Cfluc_avg_profilex1','Conc fluc avg x P1');
xlswrite(S2,handles.Cfluc_avg_profiley1','Conc fluc avg y P1');
xlswrite(S2,handles.Conc_fluc_intensity_profilex1','Conc fluc intens profile x P1');
xlswrite(S2,handles.Conc_fluc_intensity_profiley1','Conc fluc intens profile y P1');
xlswrite(S2,handles.pp1,'Spectrum periodogram p1','A1');
xlswrite(S2,handles.pv1,'Spectrum periodogram p1','B1');
xlswrite(S2,handles.wp1,'Spectrum pwelch p1','A1');
xlswrite(S2,handles.wv1,'Spectrum pwelch p1','B1');
xlswrite(S2,handles.spacial_average1','Spacial average p1');
xlswrite(S2,handles.Filtered_Cflucavg1,'Filtered Spacial average p1');
xlswrite(S2,handles.conc2,'Concentration map P2');
xlswrite(S2,handles.Cfluc_avg_profile2','Conc Fluc avg profile P2');
xlswrite(S2,handles.Conc_fluc_intensity2','Conc Fluc Intensity P2');
xlswrite(S2,handles.conc_profilex2','Conc profile x P2');
xlswrite(S2,handles.conc_profiley2','Conc profile y P2');
xlswrite(S2,handles.Cfluc_avg_profilex2','Conc fluc avg x P2');
xlswrite(S2,handles.Cfluc_avg_profiley2','Conc fluc avg y P2');
xlswrite(S2,handles.Conc_fluc_intensity_profilex2','Conc fluc intens profile x P2');
xlswrite(S2,handles.Conc_fluc_intensity_profiley2','Conc fluc intens profile y P2');
xlswrite(S2,handles.pp2,'Spectrum periodogram p2','A1');
xlswrite(S2,handles.pv2,'Spectrum periodogram p2','B1');
xlswrite(S2,handles.wp2,'Spectrum pwelch p2','A1');
xlswrite(S2,handles.wv2,'Spectrum pwelch p2','B1');
xlswrite(S2,handles.spacial_average2','Spacial average p2');
xlswrite(S2,handles.Filtered_Cflucavg2,'Filtered Spacial average p2');
xlswrite(S2,handles.comment,'comment');
xlswrite(S2,handles.vpp,'VelSpectrum periodogram','A1');
xlswrite(S2,handles.vpf,'VelSpectrum periodogram','B1');
xlswrite(S2,handles.vwp,'VelSpectrum pwelch','A1');
xlswrite(S2,handles.vwf,'VelSpectrum pwelch','B1');


function dropbar2_Callback(hObject, eventdata, handles)
choice = get(handles.dropbar2,'value');
axes(handles.axes3)

if choice == 1
    surf(handles.conc1);
    title('Solids concentration map');
    xlabel('x/D');
```

```
    ylabel ('y/D');
    zlabel ('Concentration (v/v)');
end

if choice == 2
    surf(handles.Cfluc_avg_profile1);
    title('Solids concentration fluctuations map');
    xlabel('x/D');
    ylabel ('y/D');
    zlabel ('Concentration fluctuations (v/v)');
end

if choice == 3
    surf(handles.Conc_fluc_intensity1);
    title('Solids concentration fluctuation  Intensity map 1');
    xlabel('x/D');
    ylabel ('y/D');
    zlabel ('concentration fluctuation intensity ');
end

if choice == 4
    plot(handles.conc_profilex1,handles.yd,'ro-');grid;
    title('Solids concnentration profile in x direction 1');
    xlabel('Concentration (v/v)');
    ylabel ('x/D');
end

if choice == 5
    plot(handles.conc_profiley1,handles.yd,'go-');grid
    title('Solids concnentration profile in y direction 1');
    xlabel('Concentration (v/v))');
    ylabel ('y/D');
end

if choice == 6
    plot(handles.Cfluc_avg_profilex1,handles.yd,'ro-');grid
    title('Solids concentration fluctuations profile in x direction 1');
    xlabel('Concentration fluctuations (v/v)');
    ylabel ('x/D');
end

if choice == 7
    plot(handles.Cfluc_avg_profiley1,handles.yd,'go-');grid
    title('Solids concentration fluctuations profile in y direction 1');
    xlabel('Concentration fluctuations (v/v)');
    ylabel ('y/D');
end

if choice == 8
    plot(handles.Conc_fluc_intensity_profilex1,handles.yd,'ro-');grid
    title('Concentration fluctuation intensity profile in x direction 1');
```

```
    xlabel('Fluctuation intensity');
    ylabel ('x/D');
end

if choice == 9
    plot(handles.Conc_fluc_intensity_profiley1,handles.yd,'go-');grid
    title('Concentration fluctuation intensity profile in y direction 1');
    xlabel('Fluctuation intensity');
    ylabel ('y/D');
end

if choice == 10
    surf(handles.conc2);
    title('Solids concentration map');
    xlabel('x/D');
    ylabel ('y/D');
    zlabel ('Concentration (v/v)');
end

if choice == 11
    surf(handles.Cfluc_avg_profile2);
    title('Solids concentration fluctuations map');
    xlabel('x/D');
    ylabel ('y/D');
    zlabel ('Concentration fluctuations (v/v)');
end

if choice == 12
    surf(handles.Conc_fluc_intensity2);
    title('Solids concentration fluctuation  Intensity map 1');
    xlabel('x/D');
    ylabel ('y/D');
    zlabel ('concentration fluctuation intensity ');
end

if choice == 13
    plot(handles.conc_profilex2,handles.yd,'ro-');grid;
    title('Solids concnentration profile in x direction 1');
    xlabel('Concentration (v/v)');
    ylabel ('x/D');
end

if choice == 14
    plot(handles.conc_profiley2,handles.yd,'go-');grid
    title('Solids concnentration profile in y direction 1');
    xlabel('Concentration (v/v))');
    ylabel ('y/D');
end

if choice == 15
    plot(handles.Cfluc_avg_profilex2,handles.yd,'ro-');grid
```

```
    title('Solids concentration fluctuations profile in x direction 1');
    xlabel('Concentration fluctuations (v/v)');
    ylabel ('x/D');
end

if choice == 16
    plot(handles.Cfluc_avg_profiley2,handles.yd,'go-');grid
    title('Solids concentration fluctuations profile in y direction 1');
    xlabel('Concentration fluctuations (v/v)');
    ylabel ('y/D');
end

if choice == 17
    plot(handles.Conc_fluc_intensity_profilex2,handles.yd,'ro-');grid
    title('Concentration fluctuation intensity profile in x direction 1');
    xlabel('Fluctuation intensity');
    ylabel ('x/D');
end

if choice == 18
    plot(handles.Conc_fluc_intensity_profiley2,handles.yd,'go-');grid
    title('Concentration fluctuation intensity profile in y direction 1');
    xlabel('Fluctuation intensity');
    ylabel ('y/D');
end

if choice == 19
    loglog(handles.pv1,handles.pp1);
    title('Cfluc periodogram 1');

end

if choice == 20
    loglog(handles.wv1,handles.wp1);
    title('Cfluc pwelch 1');

end

if choice == 21
    loglog(handles.pv2,handles.pp2);
    title('Cfluc periodogram 2');

end

if choice == 22
    loglog(handles.wv2,handles.wp2);
    title('Cfluc pwelch 2');

end

if choice == 23
```

```
    loglog(handles.spacial_average1);
    title('Spatial Average 1');

end

if choice == 24
    loglog(handles.spacial_average2);
    title('Spatial Average 2');

end

if choice == 25

    cut_frequency=handles.cutfreq;
    w=cut_frequency*2*9.7/8000;
    data=handles.spacial_average1';
    z=iddata(data,[],0.0012);
    zf=idfilt(z,4,w,'high');
    handles.Filtered_Cflucavg1=zf.outputdata;

    loglog(handles.Filtered_Cflucavg1);
    title('Filtered Spatial Average 1');

end

if choice == 26

    cut_frequency=handles.cutfreq;
    w=cut_frequency*2*9.7/8000;
    data=handles.spacial_average2';
    z=iddata(data,[],0.0012);
    zf=idfilt(z,4,w,'high');
    handles.Filtered_Cflucavg2=zf.outputdata;


    loglog(handles.Filtered_Cflucavg2);
    title('Filtered Spatial Average 2');

end

if choice == 27
    surf(handles.vel);
    title('Solids velocity map');
    xlabel('x/D');
    ylabel ('y/D');
    zlabel ('Velocity (m/s)');

end

if choice == 28
```

```
    surf(handles.vel_fluc);
    title('Solids velocity fluctuations map');
    xlabel('x/D');
    ylabel ('y/D');
    zlabel ('Velocity fluctuations (m/s)');
end

if choice == 29

    surf(handles.turb_intens);
    title('Solids turbulent Intensity map');
    xlabel('x/D');
    ylabel ('y/D');
    zlabel ('Turbulent Intensity ');

end

if choice == 30

    plot(handles.vel_profilex,handles.yd,'ro-');grid
    title('Solids velocity profile in x direction');
    xlabel('Velocity (m/s)');
    ylabel ('x/D');

end

if choice == 31

    plot(handles.vel_profiley,handles.yd,'go-');grid;
    title('Solids velocity profile  in y direction');
    xlabel('Velocity (m/s)');
    ylabel ('y/D');

end

if choice == 32

    plot(handles.vel_fluc_profilex,handles.yd,'ro-');grid
    title('Solids velocity fluctuations profile in x direction');
    xlabel('Velocity fluctuations (m/s)');
    ylabel ('x/D');

end

if choice == 33

    plot(handles.vel_fluc_profiley,handles.yd,'go-');grid
    title('Solids velocity fluctuations profile in y direction');
    xlabel('Velocity fluctuations (m/s)');
    ylabel ('y/D');
```

```
end

if choice == 34

    plot(handles.turb_intens_profilex,handles.yd,'ro-');grid
    title('Solids tubulent intensity profile in x direction');
    xlabel('Turbulent intensity');
    ylabel ('x/D');

end

if choice == 35

    plot(handles.turb_intens_profiley,handles.yd,'go-');grid
    title('Solids tubulent intensity profile in y direction');
    xlabel('Turbulent intensity');
    ylabel ('y/D');

end

if choice == 36
    loglog(handles.vpf,handles.vpp);
    title('Velocity fluc periodogram');

end

if choice == 37
    loglog(handles.vwf,handles.vwp);
    title('Velocity fluc pwelch');

end

guidata(hObject, handles);

function dropbar2_CreateFcn(hObject, eventdata, handles)


if ispc && isequal(get(hObject,'BackgroundColor'),
    get(0,'defaultUicontrolBackgroundColor'))
    set(hObject,'BackgroundColor','white');
end

function cutf_Callback(hObject, eventdata, handles)
handles.cutfreq = str2num(get(handles.cutf,'string'))

guidata(hObject, handles);



function cutf_CreateFcn(hObject, eventdata, handles)
```

```
if ispc && isequal(get(hObject,'BackgroundColor'),
    get(0,'defaultUicontrolBackgroundColor'))
    set(hObject,'BackgroundColor','white');
end


function sensgap_Callback(hObject, eventdata, handles)

function sensgap_CreateFcn(hObject, eventdata, handles)

if ispc && isequal(get(hObject,'BackgroundColor'),
    get(0,'defaultUicontrolBackgroundColor'))
    set(hObject,'BackgroundColor','white');
end


function nofav_Callback(hObject, eventdata, handles)

function nofav_CreateFcn(hObject, eventdata, handles)

if ispc && isequal(get(hObject,'BackgroundColor'),
    get(0,'defaultUicontrolBackgroundColor'))
    set(hObject,'BackgroundColor','white');
end

function nofr_Callback(hObject, eventdata, handles)

function nofr_CreateFcn(hObject, eventdata, handles)

if ispc && isequal(get(hObject,'BackgroundColor'),
    get(0,'defaultUicontrolBackgroundColor'))
    set(hObject,'BackgroundColor','white');
end

function nofr_CreateFcn(hObject, eventdata, handles)

function tottime_CreateFcn(hObject, eventdata, handles)

if ispc && isequal(get(hObject,'BackgroundColor'),
    get(0,'defaultUicontrolBackgroundColor'))
    set(hObject,'BackgroundColor','white');
end



function velth_Callback(hObject, eventdata, handles)

function velth_CreateFcn(hObject, eventdata, handles)

if ispc && isequal(get(hObject,'BackgroundColor'),
    get(0,'defaultUicontrolBackgroundColor'))
```

```
    set(hObject,'BackgroundColor','white');
end


function dropbar3_Callback(hObject, eventdata, handles)

choice = get(handles.dropbar3,'value');
axes(handles.axes4);

if choice == 1
    surf(handles.conc1);
    title('Solids concentration map');
    xlabel('x/D');
    ylabel ('y/D');
    zlabel ('Concentration (v/v)');
end

if choice == 2
    surf(handles.Cfluc_avg_profile1);
    title('Solids concentration fluctuations map');
    xlabel('x/D');
    ylabel ('y/D');
    zlabel ('Concentration fluctuations (v/v)');
end

if choice == 3
    surf(handles.Conc_fluc_intensity1);
    title('Solids concentration fluctuation  Intensity map 1');
    xlabel('x/D');
    ylabel ('y/D');
    zlabel ('concentration fluctuation intensity ');
end

if choice == 4
    plot(handles.conc_profilex1,handles.yd,'ro-');grid;
    title('Solids concnentration profile in x direction 1');
    xlabel('Concentration (v/v)');
    ylabel ('x/D');
end

if choice == 5
    plot(handles.conc_profiley1,handles.yd,'go-');grid
    title('Solids concnentration profile in y direction 1');
    xlabel('Concentration (v/v))');
    ylabel ('y/D');
end

if choice == 6
    plot(handles.Cfluc_avg_profilex1,handles.yd,'ro-');grid
    title('Solids concentration fluctuations profile in x direction 1');
    xlabel('Concentration fluctuations (v/v)');
```

```
    ylabel ('x/D');
end

if choice == 7
    plot(handles.Cfluc_avg_profiley1,handles.yd,'go-');grid
    title('Solids concentration fluctuations profile in y direction 1');
    xlabel('Concentration fluctuations (v/v)');
    ylabel ('y/D');
end

if choice == 8
    plot(handles.Conc_fluc_intensity_profilex1,handles.yd,'ro-');grid
    title('Concentration fluctuation intensity profile in x direction 1');
    xlabel('Fluctuation intensity');
    ylabel ('x/D');
end

if choice == 9
    plot(handles.Conc_fluc_intensity_profiley1,handles.yd,'go-');grid
    title('Concentration fluctuation intensity profile in y direction 1');
    xlabel('Fluctuation intensity');
    ylabel ('y/D');
end

if choice == 10
    surf(handles.conc2);
    title('Solids concentration map');
    xlabel('x/D');
    ylabel ('y/D');
    zlabel ('Concentration (v/v)');
end

if choice == 11
    surf(handles.Cfluc_avg_profile2);
    title('Solids concentration fluctuations map');
    xlabel('x/D');
    ylabel ('y/D');
    zlabel ('Concentration fluctuations (v/v)');
end

if choice == 12
    surf(handles.Conc_fluc_intensity2);
    title('Solids concentration fluctuation  Intensity map 1');
    xlabel('x/D');
    ylabel ('y/D');
    zlabel ('concentration fluctuation intensity ');
end

if choice == 13
    plot(handles.conc_profilex2,handles.yd,'ro-');grid;
    title('Solids concnentration profile in x direction 1');
```

```
    xlabel('Concentration (v/v)');
    ylabel ('x/D');
end

if choice == 14
    plot(handles.conc_profiley2,handles.yd,'go-');grid
    title('Solids concnentration profile in y direction 1');
    xlabel('Concentration (v/v))');
    ylabel ('y/D');
end

if choice == 15
    plot(handles.Cfluc_avg_profilex2,handles.yd,'ro-');grid
    title('Solids concentration fluctuations profile in x direction 1');
    xlabel('Concentration fluctuations (v/v)');
    ylabel ('x/D');
end

if choice == 16
    plot(handles.Cfluc_avg_profiley2,handles.yd,'go-');grid
    title('Solids concentration fluctuations profile in y direction 1');
    xlabel('Concentration fluctuations (v/v)');
    ylabel ('y/D');
end

if choice == 17
    plot(handles.Conc_fluc_intensity_profilex2,handles.yd,'ro-');grid
    title('Concentration fluctuation intensity profile in x direction 1');
    xlabel('Fluctuation intensity');
    ylabel ('x/D');
end

if choice == 18
    plot(handles.Conc_fluc_intensity_profiley2,handles.yd,'go-');grid
    title('Concentration fluctuation intensity profile in y direction 1');
    xlabel('Fluctuation intensity');
    ylabel ('y/D');
end

if choice == 19
    loglog(handles.pv1,handles.pp1);
    title('Cfluc periodogram 1');

end

if choice == 20
    loglog(handles.wv1,handles.wp1);
    title('Cfluc pwelch 1');

end
```

```
if choice == 21
    loglog(handles.pv2,handles.pp2);
    title('Cfluc periodogram 2');

end

if choice == 22
    loglog(handles.wv2,handles.wp2);
    title('Cfluc pwelch 2');

end

if choice == 23
    loglog(handles.spacial_average1);
    title('Spatial Average 1');

end

if choice == 24
    loglog(handles.spacial_average2);
    title('Spatial Average 2');

end

if choice == 25

    cut_frequency=handles.cutfreq;
    w=cut_frequency*2*9.7/8000;
    data=handles.spacial_average1';
    z=iddata(data,[],0.0012);
    zf=idfilt(z,4,w,'high');
    handles.Filtered_Cflucavg1=zf.outputdata;

    loglog(handles.Filtered_Cflucavg1);
    title('Filtered Spatial Average 1');
    %xlabel('Fluctuation intensity');
    %ylabel ('y/D');
end

if choice == 26

    cut_frequency=handles.cutfreq;
    w=cut_frequency*2*9.7/8000;
    data=handles.spacial_average2';
    z=iddata(data,[],0.0012);
    zf=idfilt(z,4,w,'high');
    handles.Filtered_Cflucavg2=zf.outputdata;


    loglog(handles.Filtered_Cflucavg2);
    title('Filtered Spatial Average 2');
```

```
end

if choice == 27
    surf(handles.vel);
    title('Solids velocity map');
    xlabel('x/D');
    ylabel ('y/D');
    zlabel ('Velocity (m/s)');

end

if choice == 28

    surf(handles.vel_fluc);
    title('Solids velocity fluctuations map');
    xlabel('x/D');
    ylabel ('y/D');
    zlabel ('Velocity fluctuations (m/s)');
end

if choice == 29

    surf(handles.turb_intens);
    title('Solids turbulent Intensity map');
    xlabel('x/D');
    ylabel ('y/D');
    zlabel ('Turbulent Intensity ');

end

if choice == 30

    plot(handles.vel_profilex,handles.yd,'ro-');grid
    title('Solids velocity profile in x direction');
    xlabel('Velocity (m/s)');
    ylabel ('x/D');

end

if choice == 31

    plot(handles.vel_profiley,handles.yd,'go-');grid;
    title('Solids velocity profile  in y direction');
    xlabel('Velocity (m/s)');
    ylabel ('y/D');

end

if choice == 32
```

```
    plot(handles.vel_fluc_profilex,handles.yd,'ro-');grid
    title('Solids velocity fluctuations profile in x direction');
    xlabel('Velocity fluctuations (m/s)');
    ylabel ('x/D');

end

if choice == 33

    plot(handles.vel_fluc_profiley,handles.yd,'go-');grid
    title('Solids velocity fluctuations profile in y direction');
    xlabel('Velocity fluctuations (m/s)');
    ylabel ('y/D');

end

if choice == 34

    plot(handles.turb_intens_profilex,handles.yd,'ro-');grid
    title('Solids tubulent intensity profile in x direction');
    xlabel('Turbulent intensity');
    ylabel ('x/D');

end

if choice == 35

    plot(handles.turb_intens_profiley,handles.yd,'go-');grid
    title('Solids tubulent intensity profile in y direction');
    xlabel('Turbulent intensity');
    ylabel ('y/D');

end

if choice == 36
    loglog(handles.vpf,handles.vpp);
    title('Velocity fluc periodogram');

end

if choice == 37
    loglog(handles.vwf,handles.vwp);
    title('Velocity fluc pwelch');
    end

guidata(hObject, handles);



function dropbar3_CreateFcn(hObject, eventdata, handles)
```

```
if ispc && isequal(get(hObject,'BackgroundColor'),
    get(0,'defaultUicontrolBackgroundColor'))
    set(hObject,'BackgroundColor','white');
end

function dropbar4_Callback(hObject, eventdata, handles)

choice = get(handles.dropbar4,'value');
axes(handles.axes5);

if choice == 1
    surf(handles.conc1);
    title('Solids concentration map');
    xlabel('x/D');
    ylabel ('y/D');
    zlabel ('Concentration (v/v)');
end

if choice == 2
    surf(handles.Cfluc_avg_profile1);
    title('Solids concentration fluctuations map');
    xlabel('x/D');
    ylabel ('y/D');
    zlabel ('Concentration fluctuations (v/v)');
end

if choice == 3
    surf(handles.Conc_fluc_intensity1);
    title('Solids concentration fluctuation  Intensity map 1');
    xlabel('x/D');
    ylabel ('y/D');
    zlabel ('concentration fluctuation intensity ');
end

if choice == 4
    plot(handles.conc_profilex1,handles.yd,'ro-');grid;
    title('Solids concnentration profile in x direction 1');
    xlabel('Concentration (v/v)');
    ylabel ('x/D');
end

if choice == 5
    plot(handles.conc_profiley1,handles.yd,'go-');grid
    title('Solids concnentration profile in y direction 1');
    xlabel('Concentration (v/v))');
    ylabel ('y/D');
end

if choice == 6
    plot(handles.Cfluc_avg_profilex1,handles.yd,'ro-');grid
    title('Solids concentration fluctuations profile in x direction 1');
```

```
    xlabel('Concentration fluctuations (v/v)');
    ylabel ('x/D');
end

if choice == 7
    plot(handles.Cfluc_avg_profiley1,handles.yd,'go-');grid
    title('Solids concentration fluctuations profile in y direction 1');
    xlabel('Concentration fluctuations (v/v)');
    ylabel ('y/D');
end

if choice == 8
    plot(handles.Conc_fluc_intensity_profilex1,handles.yd,'ro-');grid
    title('Concentration fluctuation intensity profile in x direction 1');
    xlabel('Fluctuation intensity');
    ylabel ('x/D');
end

if choice == 9
    plot(handles.Conc_fluc_intensity_profiley1,handles.yd,'go-');grid
    title('Concentration fluctuation intensity profile in y direction 1');
    xlabel('Fluctuation intensity');
    ylabel ('y/D');
end

if choice == 10
    surf(handles.conc2);
    title('Solids concentration map');
    xlabel('x/D');
    ylabel ('y/D');
    zlabel ('Concentration (v/v)');
end

if choice == 11
    surf(handles.Cfluc_avg_profile2);
    title('Solids concentration fluctuations map');
    xlabel('x/D');
    ylabel ('y/D');
    zlabel ('Concentration fluctuations (v/v)');
end

if choice == 12
    surf(handles.Conc_fluc_intensity2);
    title('Solids concentration fluctuation  Intensity map 1');
    xlabel('x/D');
    ylabel ('y/D');
    zlabel ('concentration fluctuation intensity ');
end

if choice == 13
    plot(handles.conc_profilex2,handles.yd,'ro-');grid;
```

```
    title('Solids concnentration profile in x direction 1');
    xlabel('Concentration (v/v)');
    ylabel ('x/D');
end

if choice == 14
    plot(handles.conc_profiley2,handles.yd,'go-');grid
    title('Solids concnentration profile in y direction 1');
    xlabel('Concentration (v/v))');
    ylabel ('y/D');
end

if choice == 15
    plot(handles.Cfluc_avg_profilex2,handles.yd,'ro-');grid
    title('Solids concentration fluctuations profile in x direction 1');
    xlabel('Concentration fluctuations (v/v)');
    ylabel ('x/D');
end

if choice == 16
    plot(handles.Cfluc_avg_profiley2,handles.yd,'go-');grid
    title('Solids concentration fluctuations profile in y direction 1');
    xlabel('Concentration fluctuations (v/v)');
    ylabel ('y/D');
end

if choice == 17
    plot(handles.Conc_fluc_intensity_profilex2,handles.yd,'ro-');grid
    title('Concentration fluctuation intensity profile in x direction 1');
    xlabel('Fluctuation intensity');
    ylabel ('x/D');
end

if choice == 18
    plot(handles.Conc_fluc_intensity_profiley2,handles.yd,'go-');grid
    title('Concentration fluctuation intensity profile in y direction 1');
    xlabel('Fluctuation intensity');
    ylabel ('y/D');
end

if choice == 19
    loglog(handles.pv1,handles.pp1);
    title('Cfluc periodogram 1');

end

if choice == 20
    loglog(handles.wv1,handles.wp1);
    title('Cfluc pwelch 1');

end
```

```
if choice == 21
    loglog(handles.pv2,handles.pp2);
    title('Cfluc periodogram 2');

end

if choice == 22
    loglog(handles.wv2,handles.wp2);
    title('Cfluc pwelch 2');

end

if choice == 23
    loglog(handles.spacial_average1);
    title('Spatial Average 1');

end

if choice == 24
    loglog(handles.spacial_average2);
    title('Spatial Average 2');
    end

if choice == 25

    cut_frequency=handles.cutfreq;
    w=cut_frequency*2*9.7/8000;
    data=handles.spacial_average1';
    z=iddata(data,[],0.0012);
    zf=idfilt(z,4,w,'high');
    handles.Filtered_Cflucavg1=zf.outputdata;

    loglog(handles.Filtered_Cflucavg1);
    title('Filtered Spatial Average 1');
end

if choice == 26

    cut_frequency=handles.cutfreq;
    w=cut_frequency*2*9.7/8000;
    data=handles.spacial_average2';
    z=iddata(data,[],0.0012);
    zf=idfilt(z,4,w,'high');
    handles.Filtered_Cflucavg2=zf.outputdata;


    loglog(handles.Filtered_Cflucavg2);
    title('Filtered Spatial Average 2');

end
```

```
if choice == 27
    surf(handles.vel);
    title('Solids velocity map');
    xlabel('x/D');
    ylabel ('y/D');
    zlabel ('Velocity (m/s)');

end

if choice == 28

    surf(handles.vel_fluc);
    title('Solids velocity fluctuations map');
    xlabel('x/D');
    ylabel ('y/D');
    zlabel ('Velocity fluctuations (m/s)');
end

if choice == 29

    surf(handles.turb_intens);
    title('Solids turbulent Intensity map');
    xlabel('x/D');
    ylabel ('y/D');
    zlabel ('Turbulent Intensity ');

end

if choice == 30

    plot(handles.vel_profilex,handles.yd,'ro-');grid
    title('Solids velocity profile in x direction');
    xlabel('Velocity (m/s)');
    ylabel ('x/D');

end

if choice == 31

    plot(handles.vel_profiley,handles.yd,'go-');grid;
    title('Solids velocity profile  in y direction');
    xlabel('Velocity (m/s)');
    ylabel ('y/D');

end

if choice == 32

    plot(handles.vel_fluc_profilex,handles.yd,'ro-');grid
    title('Solids velocity fluctuations profile in x direction');
```

```
    xlabel('Velocity fluctuations (m/s)');
    ylabel ('x/D');

end

if choice == 33

    plot(handles.vel_fluc_profiley,handles.yd,'go-');grid
    title('Solids velocity fluctuations profile in y direction');
    xlabel('Velocity fluctuations (m/s)');
    ylabel ('y/D');

end

if choice == 34

    plot(handles.turb_intens_profilex,handles.yd,'ro-');grid
    title('Solids tubulent intensity profile in x direction');
    xlabel('Turbulent intensity');
    ylabel ('x/D');

end

if choice == 35

    plot(handles.turb_intens_profiley,handles.yd,'go-');grid
    title('Solids tubulent intensity profile in y direction');
    xlabel('Turbulent intensity');
    ylabel ('y/D');

end

if choice == 36
    loglog(handles.vpf,handles.vpp);
    title('Velocity fluc periodogram');

end

if choice == 37
    loglog(handles.vwf,handles.vwp);
    title('Velocity fluc pwelch');

end
guidata(hObject, handles);



function dropbar4_CreateFcn(hObject, eventdata, handles)

if ispc && isequal(get(hObject,'BackgroundColor'),
    get(0,'defaultUicontrolBackgroundColor'))
```

```
    set(hObject,'BackgroundColor','white');
end



function comment_Callback(hObject, eventdata, handles)

temptext = get(hObject,'string');
handles.comment = temptext;
guidata(hObject, handles);

function comment_CreateFcn(hObject, eventdata, handles)



if ispc && isequal(get(hObject,'BackgroundColor'),
    get(0,'defaultUicontrolBackgroundColor'))
    set(hObject,'BackgroundColor','white');
end


function initial_Callback(hObject, eventdata, handles)

function initial_CreateFcn(hObject, eventdata, handles)

if ispc && isequal(get(hObject,'BackgroundColor'),
    get(0,'defaultUicontrolBackgroundColor'))
    set(hObject,'BackgroundColor','white');
end

% --------------------------------------------------------------------
function Saveconc_Callback(hObject, eventdata, handles)

S2 = strcat(handles.File,'analysed_result.xls');


xlswrite(S2,handles.conc1,'Concentration map P1');
xlswrite(S2,handles.Cfluc_avg_profile1','Conc Fluc avg profile P1');
xlswrite(S2,handles.Conc_fluc_intensity1','Conc Fluc Intensity P1');
xlswrite(S2,handles.conc_profilex1','Conc profile x P1');
xlswrite(S2,handles.conc_profiley1','Conc profile y P1');
xlswrite(S2,handles.Cfluc_avg_profilex1','Conc fluc avg x P1');
xlswrite(S2,handles.Cfluc_avg_profiley1','Conc fluc avg y P1');
xlswrite(S2,handles.Conc_fluc_intensity_profilex1','Conc fluc intens profile x P1');
xlswrite(S2,handles.Conc_fluc_intensity_profiley1','Conc fluc intens profile y P1');
xlswrite(S2,handles.spacial_average1','Spacial average p1');
xlswrite(S2,handles.Filtered_Cflucavg1,'Filtered Spacial average p1');
xlswrite(S2,handles.conc2,'Concentration map P2');
xlswrite(S2,handles.Cfluc_avg_profile2','Conc Fluc avg profile P2');
xlswrite(S2,handles.Conc_fluc_intensity2','Conc Fluc Intensity P2');
xlswrite(S2,handles.conc_profilex2','Conc profile x P2');
```

```
xlswrite(S2,handles.conc_profiley2','Conc profile y P2');
xlswrite(S2,handles.Cfluc_avg_profilex2','Conc fluc avg x P2');
xlswrite(S2,handles.Cfluc_avg_profiley2','Conc fluc avg y P2');
xlswrite(S2,handles.Conc_fluc_intensity_profilex2','Conc fluc intens profile x P2');
xlswrite(S2,handles.Conc_fluc_intensity_profiley2','Conc fluc intens profile y P2');


% ------------------------------------------------------------------------
function savevel_Callback(hObject, eventdata, handles)

S2 = strcat(handles.File,'analysed_result.xls');

xlswrite(S2,handles.vel,'Velocity Map');
xlswrite(S2,handles.vel_fluc,'Velocity Fluctuation');
xlswrite(S2,handles.turb_intens,'Turbulant Intensity Map');
xlswrite(S2,handles.vel_profilex','Velocity profile x');
xlswrite(S2,handles.vel_profiley','Velocity profile y');
xlswrite(S2,handles.vel_fluc_profilex','Velocity profile fluc x');
xlswrite(S2,handles.vel_fluc_profiley','Velocity profile fluc y');
xlswrite(S2,handles.turb_intens_profilex','Turb Intens profile x');
xlswrite(S2,handles.turb_intens_profiley','Turb Intens profile y');


% ------------------------------------------------------------------------
function savespec_Callback(hObject, eventdata, handles)

S2 = strcat(handles.File,'analysed_result.xls');
xlswrite(S2,handles.pp1,'Spectrum periodogram p1','A1');
xlswrite(S2,handles.pv1,'Spectrum periodogram p1','B1');
xlswrite(S2,handles.wp1,'Spectrum pwelch p1','A1');
xlswrite(S2,handles.wv1,'Spectrum pwelch p1','B1');
xlswrite(S2,handles.spacial_average1','Spacial average p1');
xlswrite(S2,handles.Filtered_Cflucavg1,'Filtered Spacial average p1');
xlswrite(S2,handles.pp2,'Spectrum periodogram p2','A1');
xlswrite(S2,handles.pv2,'Spectrum periodogram p2','B1');
xlswrite(S2,handles.wp2,'Spectrum pwelch p2','A1');
xlswrite(S2,handles.wv2,'Spectrum pwelch p2','B1');
xlswrite(S2,handles.spacial_average2','Spacial average p2');
xlswrite(S2,handles.Filtered_Cflucavg2,'Filtered Spacial average p2');
xlswrite(S2,handles.vpp,'VelSpectrum periodogram','A1');
xlswrite(S2,handles.vpf,'VelSpectrum periodogram','B1');
xlswrite(S2,handles.vwp,'VelSpectrum pwelch','A1');
xlswrite(S2,handles.vwf,'VelSpectrum pwelch','B1');



function nfftcb_Callback(hObject, eventdata, handles)

function nfftcb_CreateFcn(hObject, eventdata, handles)

if ispc && isequal(get(hObject,'BackgroundColor'),
```

```
    get(0,'defaultUicontrolBackgroundColor'))
    set(hObject,'BackgroundColor','white');
end



function nfftvb_Callback(hObject, eventdata, handles)

function nfftvb_CreateFcn(hObject, eventdata, handles)

if ispc && isequal(get(hObject,'BackgroundColor'),
    get(0,'defaultUicontrolBackgroundColor'))
    set(hObject,'BackgroundColor','white');
end
```